DISSERTATION

FROM THE COLORADO FRONT RANGE TO GLOBAL TOPOGRAPHY:

EVALUATING THE ROLES OF TECTONICS AND CLIMATE ON LONG TERM LANDSCAPE EVOLUTION

Submitted by

Eyal Marder

Department of Geosciences

In partial fulfillment of the requirements

For the Degree of Doctor of Philosophy

Colorado State University

Fort Collins, Colorado

Summer 2022

Doctoral Committee:

Advisor: Sean Gallen

Frank Pazzaglia
Ellen Wohl
Derek Schutt
Stephanie Kampf

ABSTRACT

FROM THE COLORADO FRONT RANGE TO GLOBAL TOPOGRAPHY: EVALUATING THE ROLES OF TECTONICS AND CLIMATE ON LONG TERM LANDSCAPE EVOLUTION

Landscapes are primarily shaped by the interactions between tectonics and climate, and their interplay and relative roles in landscape evolution over thousands to millions of years have a significant impact on global erosion and nutrient and sediment productions. Thus, understanding and quantifying the impact of tectonics and climate on short- to long-term landscape evolution has large implications on natural global cycles (e.g., climate change, atmospheric and terrestrial carbon circulations), biodiversity and ecological sustainability, hazard management (e.g., earthquakes, landslides), infrastructure planning, and decision making. In the last decades, significant progress has been made in the field of tectonic geomorphology to try and resolve the relative roles of tectonics and climate in landscape evolution. Yet, many questions remained unresolved, for instance:

- What drives landscape evolution in post-orogenic settings?
- What is the relative role of climate in landscape evolution at the global scale?

In my PhD, I address these questions by investigating the impact of tectonics and climate on fluvial topography and geomorphology at different spatiotemporal scales. In my first chapter, I present a local study in the southern Colorado Front Range to explore the relative roles of tectonics and climate on observed landscape unsteadiness that affected the area during the late Cenozoic. In the second chapter, I extend this study and address this question to the scale of the entire Colorado Front Range. In my third chapter, I explore the impact of climate on fluvial topography at the global scale. For all these studies, I integrate field data, digital topographic analysis, geochronology, and modeling to compare new and existing predictions for the roles of tectonics and climate at the local (chapter I), regional (chapter II), and global (chapter III) scales to empirical observations. Results from these studies shed light on some ongoing controversies (e.g., what drives topographic rejuvenation in the Colorado Front Range) and resolve misunderstood concepts (e.g., how climate is recorded in fluvially-dominated landscapes). The first and third chapters in this dissertation were submitted to peer-reviewed journals and are under review, while the second chapter is in its final stage as a third manuscript for a peer-reviewed journal.

FIRST CHAPTER: LATE CENOZOIC DEFORMATION IN THE SOUTHERN COLORADO FRONT RANGE REVEALED BY RIVER PROFILE ANALYSIS AND FLUVIAL TERRACES

Post-orogenic landscapes are important sources of sediment and nutrients relevant to many natural global cycles and ecological sustainability. Many of these settings exhibit evidence of recent landscape unsteadiness, but their driving mechanisms are poorly understood. The Colorado Front Range (FR), a post-orogenic setting that maintains high relief, elevated topography, and evidence of ongoing unsteadiness, is a good example of this enigma. Two prevailing hypotheses have been proposed to explain the geologically-recent landscape unsteadiness in the FR: (1) mantle dynamics and active tectonics during the late Cenozoic; (2) enhanced erosional efficiency associated with a Quaternary climate change. Here we evaluate these end-member hypotheses through a case study of tectonic geomorphology of the Upper Arkansas River basin in southern Colorado. We perform river profile analysis on bedrock channels in the eastern Rockies and map and analyze fluvial terraces in the western High Plains. We find that knickpoints in the eastern Rockies record a one- to two-stage increase in base level fall rate downstream of the FR mountain front and an eastward increase in the magnitude of incision. Similarly, terraces in the western High Plains record an eastward increase in the magnitude of incision. Collectively, and supported by flexural and supplemental geomorphic analyses, these results suggest a previously undetected regional-scale, west-directed back tilting signal associated with differential rock uplift. Based on existing geodynamic models, we interpret these deformation patterns and related landscape response as a result of a migrating dynamic topography that swept the southern FR from west to east during the late Cenozoic.

SECOND CHAPTER: TECTONIC AND GEODYNAMIC CONTROL ON REJUVENATION IN THE COLORADO ROCKY MOUNTAINS

The Colorado Rocky Mountains (CRM) ancient foreland basin, currently known as the High Plains, shows a steeper long-wavelength tilt away from its hinterland relative to other active mountain range foreland basins worldwide. Further, studies showed that the High Plains experienced a transition from a system of net deposition to one characterized by net erosion at ~5 Ma. However, the mechanisms proposed to explain these observations are the center of ongoing debate. Some argue that the tilting and the transition from deposition to erosion were facilitated by tectonically- or geodynamically-driven changes in rock uplift rate, while others argue that these records are simply the result of an increase in erosional efficiency driving river incision and relaxation with some amount of isostatic rebound. One of the main reasons this controversy continues is that empirical studies trying to address this question were

conducted mostly in the High Plains, where landscape geomorphic signatures used to distinguish between these two hypotheses are ambiguous. Here, we conduct a geomorphic analysis of the Colorado Rockies, which lies upstream of the High Plains province and is characterized by a harder crystalline basement, where bedrock rivers might still achieve a record of the transient landscape of the CRM and help clarify potential drivers. We combine river profile analysis with a compilation of new and existing basin average erosion rates from cosmogenic ^{10}Be and channel incision rates from luminescence dating on fluvial terraces to differentiate two geomorphic zones in the Colorado Rockies: 1. an upper, relict topography upstream of convex upward knickpoints that is consistent with lower long-term background erosion rates of ~0.03 mm/yr and lower channel steepness of ~80-100 $m^{0.9}$; 2. a transient landscape downstream of these knickpoints that is consistent with higher channel incision rates of ~0.3 mm/yr and higher channel steepness that increases systematically from ~150 $m^{0.9}$ in the northern CRM to 300 $m^{0.9}$ in the southern CRM. These results and their spatial patterns across the CRM are inconsistent with existing predictions from a climate-induced increased erosional efficacy during the last Cenozoic. Rather, they imply a long-wavelength deformation and a sustained tectonic uplift rate associated with active tectonics and geodynamics that impacted the CRM in the last 5 Ma.

THIRD CHAPTER: CLIMATE CONTROLS ON FLUVIAL TOPOGRAPHY

Conceptual and theoretical models for landscape evolution suggest that fluvial topography is sensitive to climate. However, it has remained challenging to demonstrate a compelling link between fluvial topography and climate state in natural landscapes. One possible reason is that many studies compare erosion rates to climate data, although theoretical studies note that, at steady-state, climate is encoded in topography rather than in erosion rates. Here, we use an existing global compilation of ^{10}Be basin average erosion rates to isolate the climate signal in topography for fluvially-dominated catchments underlain by crystalline bedrock that appear to be in morphological steady state. Our results show that the nonlinearity between erosion rates and the normalized river channel steepness index, which is a proxy for fluvial relief, systematically increases with increasing mean annual precipitation and decreasing aridity. When interpreted in the context of detachment-limited bedrock incision models that account for incision thresholds and stochastic distribution of floods, this systematic pattern can be explained by a decrease in discharge variability in landscapes that are wetter and less arid, assuming incision thresholds are important. Our results imply a climate control on topography at a global scale and highlight new research directions that can improve understanding of climate's impact on landscape evolution.

ACKNOWLEDGEMENTS

First and foremost, I would like to thank my advisor, Dr. Sean F. Gallen. Without his meticulous guidance and support, the completion of this dissertation would not have been possible. Thank you for making me a better scientist.

I would like to thank my committee members. Each of them supported and contributed to this dissertation in different ways.

I would also like to thank the Geosciences Department at Colorado State University and the Geological Society of America for their financial support during my doctorate studies.

Finally, I would like to thank my parents. While being on the other side of the globe, they were always close, supporting, and caring.

TABLE OF CONTENTS

LIST OF FIGURES

Chapter 1

Chapter 2

Chapter 3

Appendix A

Appendix B

Appendix C

Chapter 1: Late Cenozoic deformation in the Southern Colorado Front Range revealed by river profile analysis and fluvial terraces[1]

1.1 Introduction

Mountain belts are important sources of sediment and nutrients for land and ocean environments and affect global carbon cycles, short and long term climate changes, and biodiversity (Smith, 1979; Raymo et al., 1988; Tucker and van der Beek, 2013; Larsen et al., 2014; Pecl et al., 2017; Antonelli et al., 2018). Most research on landscape evolution of mountain belts is focused on tectonically active settings, whereas post-orogenic settings are relatively less well explored despite covering ~20% of Earth's terrestrial surface and being a fundamentally important component of the life cycle of mountains (Gallen, 2018; Fülöp et al., 2020). Recent studies in such settings (e.g., Pazzaglia and Brandon, 1996; Galloway et al., 2011; Gallen et al., 2013; Tucker and van der Beek, 2013; Gallen, 2018; Fülöp et al., 2020; Fillon et al., 2021) showed that decaying mountain belts evolution is not consistent with the traditional view of a slow and steady reduction of mean elevation and topographic relief toward a subdued, flat surface (e.g., Davis, 1889). These and other studies showed that most post-orogenic settings record evidence of landscape unsteadiness long after tectonic activity ends (Tucker and van der Beek, 2013; Gallen, 2018; Moodie et al., 2018). A wide range of explanations have been invoked to explain the ongoing landscape unsteadiness in post-orogenic settings, namely dynamic topography, phase changes in the mantle lithosphere and buoyancy, global and regional climate change, isostasy and lithospheric flexure, drainage reorganization, and lithological variability (Pazzaglia and Gardner, 1994; Fischer, 2002; Prince et al., 2011; Gallen et al., 2013; Miller et al., 2013; Tucker and van der Beek, 2013; Willett et al., 2014; Jones et al., 2015; Giachetta et al., 2015; Molnar et al., 2015; Beeson et al., 2017; Blackburn et al., 2018; Gallen, 2018; Peifer et al., 2020; Tao et al., 2020). Perhaps not surprisingly, and due to the multitude of factors that can affect post-orogenic landscape dynamics, there is no consensus on what drives landscape unsteadiness in these settings.

The US Colorado Front Range (herein the FR; Figure 1.1), which we define here as the region extending from the Continental Divide to the western-most High Plains, is perhaps one of the most

---

[1] Chapter is in review for Geological Society of America Bulletin as Marder, E., Gallen, S.F., and Pazzaglia, F.J., Late Cenozoic deformation in the Southern Colorado Front Range revealed by river profile analysis and fluvial terraces.

recognizable and well-studied decaying mountain belts in the world (Tucker and van der Beek, 2013). Located in the middle of the North American plate, the FR maintains unique physiography with high elevation mountains underlain mostly by Precambrian crystalline rocks, which are adjacent to low relief topography of Mesozoic-to-Cenozoic sedimentary units that were deformed and tilted during the Laramide Orogeny at ~40 - 80 Ma (Epis et al., 1976; Damon, 1983). Many studies assume that most of the high elevation in the FR was established during the Laramide Orogeny. However, evidence of increased sediment flux, uplift, and incision across different parts of the FR indicates a geologically-recent landscape unsteadiness (Leonard, 2002; McMillan and Heller, 2006; Pelletier, 2009; Wobus et al., 2010; Tucker and van der Beek, 2013). Based on this evidence, speculation surrounds the relative roles of active tectonics, mantle dynamics, and climate changes during the late Cenozoic on rejuvenation of topography, relief, exhumation rate, and sediment flux across the FR (Epis et al., 1976; Mitrovica et al., 1989; Molnar and England, 1990; Leonard, 2002; McMillan and Heller, 2006; Riihimaki et al., 2007; Moucha et al., 2008; Wobus et al., 2010; Langston et al., 2015; Abbey et al., 2018; Willett et al., 2018). This and subsequent studies have led to two hypotheses to explain the evidence of recent landscape unsteadiness in the FR.

The first hypothesis invokes tectonic and geodynamic processes as the dominant drivers and is supported by mantle convection models, paleo-hydraulic and sedimentological studies on Neogene formations, depositional profiles and reconstructed topographies in the FR High Plains, and thermochronological dating across the southern Rocky Mountains (Leonard, 2002; McMillan et al., 2002; McMillan and Heller, 2006; Karlstrom et al., 2012; Duller et al., 2012; Rosenberg et al., 2014; Abbey and Niemi, 2018). Within this view, dynamic topography and active tectonics associated with the Rio Grande Rift are suggested to tilt the FR eastward, rejuvenate its topography, and increase exhumation and incision rates downstream the FR (Mitrovica et al., 1989; Leonard, 2002; McMillan and Heller, 2006).

The second hypothesis invokes landscape changes across the FR as a response to climate change and associated erosional efficacy during the Quaternary. This hypothesis is based on temporal coincidence of geomorphic and stratigraphic markers with independent records of climate change, both of which align well with predictions of landscape evolution models (Riihimaki et al., 2006, 2007; Pelletier, 2009; Wobus et al., 2010; Dühnforth et al., 2012; Tucker and van der Beek, 2013; Langston et al., 2015). These studies suggest that integrated climate changes and associated variations in discharge, modulated by water storage and release during glacial-interglacial cycles in the Quaternary, increased erosional efficiency in the High Plains without attendant tectonic or dynamic forcing (Riihimaki et al., 2007; Pelletier, 2009; Wobus et al., 2010; Dühnforth et al., 2012). Within this view, roughly regionally uniform climate change would result in regional shoaling of river gradients, mostly in rivers across the High Plains (Wobus et al., 2010; Langston et al., 2015).

Here we investigate these two prevailing hypotheses by exploring different geomorphic markers across the FR main physiographic provinces (e.g., Pazzaglia and Gardner, 1994; Lavé and Avouac, 2000; Wobus et al., 2010; Gallen and Wegmann, 2017). We focus on the upper Arkansas Basin in southern Colorado (herein the southern FR; Figure 1.1) that has been influenced by both active tectonics of the northern tip of the Rio Grande Rift (Leonard, 2002; Abbey and Niemi, 2018) and glacial-interglacial climatic changes during the Quaternary (Young et al., 2011; Schweinsberg et al., 2016, 2020) to reconstruct the relative history of incision and rock uplift along the Arkansas River main stem. In the eastern Rockies, which is dominated by a crystalline basement with incised bedrock channels, we conduct river profile analysis on tributary trunks of the Arkansas River to document the relative incision history of the mainstem (Figure 1.1). In the western High Plains, which is dominated by highly erodible late Mesozoic to Cenozoic sedimentary units, we map and correlate Pleistocene fluvial terraces along a ~50 km transect of the Arkansas River valley from Canon City, CO, downstream to Pueblo, CO, to constrain the history of incision and rock uplift of the Arkansas River further downstream (Figure 1.1). We combine results from the two provinces to derive a complete picture of the relative incision history of the Arkansas River across the southern FR, and interpret results within the context of existing tectonic and climate hypotheses to evaluate the dominant driver(s) responsible for recent landscape unsteadiness in the FR.

1.2 Background

1.2.1 Geological and Geomorphological Setting of the Front Range

The FR is a partitioned crustal-scale block that was uplifted during the Laramide Orogeny (~40 - 80 Ma), an event that warped and folded Paleozoic strata of the western North American passive margin and Mesozoic strata of the Laramide-Sevier foreland along a high angle reverse fault beneath the present-day Front Range (Dickinson and Snyder, 1978; Bird, 1998; Heller et al., 2003; DeCelles, 2004; Liu et al., 2010; Dickinson et al.). At the close of the Laramide Orogeny in the Paleocene to the late Eocene, the modern-day FR mountain front was buried by coarse, locally sourced alluvial fan deposits (Brown, 1943; Epis et al., 1976). During the Oligocene, the entire Laramide foreland (including the FR) was subsequently blanketed by west-sourced volcaniclastics, and summits were pedimented to form the Rocky Mountain surface (Scott and Taylor, 1975; Steven, 1975; Epis et al., 1976; Kluth and Nelson, 1988; Abbey et al., 2018). During the onset of the Miocene crustal extension associated with the Rio Grande Rift, parts of the

FR were dismembered and structurally inverted to form the Sangre de Cristo and Wet mountains and their associated normal-fault bound valleys (Figure 1.1; Epis et al., 1976; Abbey et al., 2017; Abbey and Niemi, 2018). Since the waning activity of the Rio Grande Rift around the late Miocene to Pliocene (Morgan et al., 1986; Kelley et al., 1992; Abbey and Niemi, 2018), the FR was concurrently exhumed from its Laramide molasse (Leonard, 2002; McMillan et al., 2002; McMillan and Heller, 2006; Duller et al., 2012; Willett et al., 2018) and modified by alternating Quaternary glacial-interglacial climate processes (Wobus et al., 2010; Dühnforth et al., 2012; Tucker and van der Beek, 2013; Langston et al., 2015).

The geological and geomorphic history of the FR resulted in the development of two major physiographic provinces with a sharp lithologic and topographic contrast west and east of the FR mountain front: the rugged, high-relief eastern Rockies; and the subdued, low-relief western High Plains (Figure 1.1; Tuyl and Lovering, 1935; Chapin and Kelley, 1997; Keller and Morgan, 2016). The eastern Rockies is underlain by a Proterozoic crystalline basement, which is partially covered by Oligocene to Miocene volcanic and volcanoclastic units (Epis and Chapin, 1974, 1975; Grambling and Tewksbury, 1989; Keller and Morgan, 2016) and Quaternary alluvial deposits from the Sangre de Cristo and Wet mountains (Epis et al., 1976; Lindsey et al., 2005). The western High Plains is underlain by gently deformed, east tilted late Mesozoic to Cenozoic marine sedimentary units (limestone, marl, and siltstone), gravels of the Miocene Ogallala Formation, and Pleistocene and Holocene alluvial deposits along major river valleys (Madole, 1991; Lindsey et al., 2005).

The sharp lithological contrast between the eastern Rockies and the western High Plains results in a differential landscape response and contrasting spatiotemporal incision patterns across the FR drainage network (Zaprowski et al., 2001; McMillan and Heller, 2006; Dethier et al., 2014; Willett et al., 2018). In the eastern Rockies, bedrock channels are incised into the Proterozoic crystalline basement (Heede, 1970) to form deep gullies and canyons, such as the Royal Gorge (Powers, 1935; Clarey et al., 2004). In contrast, some areas in the Upper Arkansas Valley (Figure 1.1, red dashed line) and basins that tap the Sangre de Cristo and Wet mountain ranges (Figure 1.1, purple and brown dashed lines, respectively) are locally affected by recent glaciation and/or alluviation (avoided in this study, see Methods; Schweinsberg et al., 2016, 2020). In the western High Plains, the fluvial network predominantly consists of mixed bedrock-alluvial channels that are incised into the late Mesozoic to Cenozoic sedimentary units and are largely covered by Quaternary gravel deposits that were transported from the Wet Mountains and the eastern Rockies drainage networks (Figure 1.1; Scott, 1960; Scott and Lindvall, 1970).

1.2.2 Predicted geomorphic patterns for tectonic and climate scenarios in the Front Range

In this study, we aim to derive the geologically-recent relative incision history of the Arkansas River to determine the main driver(s) (i.e., tectonics and/or climate) for recent landscape unsteadiness in the southern FR. We target the Arkansas River and its tributary trunks to compare observed geomorphic patterns with predicted patterns from the previously suggested tectonic and climate hypotheses. Each of these hypotheses makes different and unique predictions for the relative base level fall and landscape response patterns in the FR.

In the case of the tectonic hypothesis, where many studies suggest that the FR was tilted eastward during the late Cenozoic (Figure 1.2A – H1; e.g., Leonard, 2002; McMillan and Heller, 2006; Abbey and Niemi, 2018), the predicted geomorphic patterns include a series of concave down slope-break knickpoints in the eastern Rockies (herein “normal knickpoints”; e.g., Kirby and Whipple, 2012). These knickpoints will show a gradual increase in elevation and channel steepness in reaches below them as a function of distance upstream (westwards) towards the tectonic loci (e.g., Kirby and Whipple, 2012; Mitchell and Yanites, 2019). Similarly, fluvial terraces in the western High Plains will deform in an upstream fanning pattern with an increased gradient in slope and elevation towards the tectonic loci (e.g., Wobus et al., 2010).

In the case of the climate hypothesis (Figure 1.2A – H2; e.g., Riihimaki et al., 2006, 2007; Pelletier, 2009; Wobus et al., 2010; Dühnforth et al., 2012; Tucker and van der Beek, 2013; Langston et al., 2015), the climate-induced increased erosional efficiency during the Quaternary will result in a series of concave up slope-break knickpoints (herein “inverted knickpoints”; e.g., Zaprowski et al., 2005). In contrast to knickpoint spatial patterns for the tectonic hypothesis, the inverted knickpoints will lie at similar elevations, and fluvial reaches below them will have gentler slopes. In the western High Plains, the regional increased erosional efficiency will relax main channels, and the fluvial terraces will show a fanning pattern that record the gradual reduction of past river gradients (e.g., Wobus et al., 2010).

1.2.3 River Profile Analysis

The detachment-limited stream power incision model provides a convenient framework to analyze and interpret longitudinal river profiles in terms of tectonic and climate changes over intermediate (10^4 yr) to long (10^6 yr) time scales (Howard, 1994; Whipple and Tucker, 1999; Whipple, 2004; Lague, 2014). The model approximates bedrock channel erosion rates, E, based on upstream drainage area, A, which is a proxy for water discharge, and local channel slope, S, scaled by a coefficient of erodibility, K, that incorporates the effects of climate, hydrology, substrate erodibility, and drainage geometry, and empirical constants m and n that depend on basin hydrology, hydraulic geometry, and the dominant incision process (Howard, 1994; Whipple and Tucker, 1999):

$$E = KA^m S^n \tag*{(1).}$$

Equation 1 can be solved for local channel slope (Figure 1.2B):

$$S = \left(\frac{E}{K}\right)^{1/n} A^{-m/n} \tag*{(2),}$$

which has the same form as Flint's law for steady-state, graded river profiles (Flint, 1974):

$$S = k_s A^{-\theta} \tag*{(3),}$$

where k_s is defined as the channel steepness index and θ as the channel concavity index. Comparison of equations 2 and 3 suggests that:

$$k_s = (E/K)^{1/n} \tag*{(4)}$$

$$\theta = m/n \tag*{(5).}$$

Therefore, at steady state, where E equals the rock uplift rate, U (Snyder et al., 2000; Kirby and Whipple, 2012), equations 4 and 5 show that k_s is sensitive to tectonics and climate, while θ is largely insensitive to these factors (Snyder et al., 2000; Tucker and Whipple, 2002; Kirby and Whipple, 2012). To handle the covariation of k_s with θ, the normalized steepness index, k_{sn}, is calculated using a reference concavity index, θ_{ref}. For basins spanning a range of conditions in similar lithology and climate settings, such as the eastern Rockies, studies show that typical θ_{ref} span a small range of ~0.3 – 0.7 (e.g. Ouimet et al., 2009; DiBiase et al., 2010; Kirby and Whipple, 2012). In this study, we calibrate θ_{ref} empirically from a digital elevation model (DEM) (Appendix A; Schwanghart and Scherler, 2014).

k_{sn} can be quantified for a river profile through analysis of log-transformed S and A data (Equation 3; Wobus et al., 2006; Kirby and Whipple, 2012). However, taking the derivative of elevation with respect to distance to calculate S introduces unwanted noise into the analysis, thus requiring a large amount of smoothing (Snyder et al., 2000; Wobus et al., 2006). To avoid this shortcoming, a transformed length parameter, χ, that is a path-dependent integral of the inverse of A raised to an exponent (Royden and Perron, 2013) is used instead:

$$\chi = \int_{x_b}^{x} \left(\frac{A_0}{A(x')}\right)^{\frac{m}{n}} dx' \tag*{(6),}$$

where x_b is the referenced distance at the drainage network outlet, x is the upstream distance along the channel, and A_0 is the referenced upstream drainage area, usually chosen as unity ($A_0 = 1$). Equation 3 (or 2) can be integrated to generate a χ-elevation plot (typically referred to as a χ-plot):

$$z(x) = z(x_b) + k_{sn}\chi \qquad (7).$$

Linear regressions through χ-plot segments are often used to determine average k_{sn} for different segments along a river profile, which is interpreted as a reach-scale proxy for relative bedrock channel erosion rate (Figure 1.2C). Importantly, equation 7, along with an estimate of the segment k_{sn}, are commonly used to reconstruct paleo-river profiles above transient knickpoints by linear extrapolation of the segment above the knickpoint location to its outlet in χ-plots (Figure 1.2C). These paleo-river profile reconstructions are thus useful for quantifying incision depths below migrating knickpoints and determining spatiotemporal deformation patterns across a drainage network (e.g., Schoenbohm et al., 2004; Gallen et al., 2013; Mitchell and Yanites, 2019).

The upstream migration of knickpoints generated by changes in base level fall rates can be modeled as a kinematic wave based on equation 1. In the case of a step-change in base level fall/uplift rate with uniform K, m, and n, the vertical velocity of a knickpoint is uniform such that related knickpoints will lie at the same elevation contour (Niemann et al., 2001). The horizontal knickpoint velocity (celerity), C $(= \frac{dx}{dt})$, is defined, on the other hand, as (Whipple and Tucker, 1999; Crosby and Whipple, 2006):

$$C(x) = K(x)A(x)^m S(x)^{n-1} \qquad (8),$$

where equation 8 can be rearranged and integrated to derive the fluvial response time, τ:

$$\tau(x) = \int_0^x \frac{dx'}{C(x)} \qquad (9).$$

In the special case where $n = 1$ (i.e., bedrock incision is dominated by plucking; Whipple et al., 2000) and assuming a uniform K for a drainage network wholly in crystalline rocks or Phanerozoic sedimentary cover (a reasonable assumption for the eastern Rockies, based on field observations and geological data), $\tau(x) \propto \chi(x)$. Under such conditions, the slope term in equation 8 drops out and genetically related knickpoints are expected to migrate throughout a river network at the same rate in χ-space. In this case, knickpoints generated by the same base level fall event will be located at similar elevations in case of a uniform uplift or at different elevations in case of a spatially varied uplift (Berlin and Anderson, 2007; Kirby and Whipple, 2012; Mitchell and Yanites, 2019), while χ-distance for these knickpoints will be the same regardless of the uplift pattern.

Thus, based on knickpoint elevation and χ-distance patterns, one can test if a series of knickpoints within a drainage basin is genetically related to a base level fall event from a common reference base level position and if uplift has been uniform or varied over time (e.g., Gallen and Wegmann, 2017; Mitchell and Yanites, 2019). Since slope-break knickpoints (predicted by the prevailing hypotheses described above) are identified as changes in k_{sn} for different segments along a river profile (in contrast to vertical-step knickpoints that show an abrupt local change in k_{sn}; e.g., Haviv et al., 2010; Kirby and Whipple, 2012), calculating the average k_{sn} in even χ-bins for a catchment-scale drainage network can be used to identify and validate locations of these knickpoints. Here we use a matrix inversion of river network elevations and discretized χ (e.g., Goren et al., 2014; Gallen, 2018; Pavano and Gallen, 2021) to calculate these basin-wide k_{sn}-χ patterns and test if prominent knickpoints mapped along tributary trunks can be interpreted as genetically related (for further information on this method, see Appendix A).

1.2.4 Fluvial Terraces in the Western High Plains

Fluvial terraces in the western High Plains were previously investigated in our study area and in several places along the northern and central FR (Table 1.1). Excluding a pre-Pleistocene surface (commonly termed “the Nussbaum terrace”) and a Holocene terrace (commonly termed “the Broadway terrace”), all documented fluvial terraces in the western High Plains region are Pleistocene in age (Scott, 1960; Madole, 1991). In previous studies, these Pleistocene terraces were mapped as allostratigraphic units in the northern and central FR and classified based on their ages, sedimentology, and/or strath elevations above major rivers in the area. These terraces are termed (from older to younger) as the Rocky Flats, the Verdos, the Slocum, and the Louviers terraces (Table 1.1; Scott, 1960; Madole, 1991; Lindsey et al., 2005; Riihimaki et al., 2006; Dühnforth et al., 2012).

In the Denver area, the youngest Louviers terraces show a wide range of ages between ~15 - 130 ka (Szabo, 1980; Schildgen et al., 2002). In the upper Arkansas Basin (our study area), Slocum terraces were dated to ~190 ka based on a U-series dating on a bison horn (Scott and Lindvall, 1970; Szabo, 1980). In the northern and central FR, surfaces classified as Verdos terraces were dated to ~620 ka based on the observed presence of the Lava Creek B volcanic ash in their terrace stratigraphy (Madole, 1991), but later studies on correlative terraces in the Boulder area showed younger ages ~200 - 400 ka (Riihimaki et al., 2006; Dühnforth et al., 2012). The oldest Pleistocene surfaces in the FR, the Rocky Flats terraces, are considered to be ~1.3 to 2 Ma in age (Scott, 1960; Madole, 1991; Birkeland et al., 1999; Schildgen et al., 2002), but later studies showed that this age might vary between ~400 - 800 ka (Riihimaki et al., 2006; Dühnforth et al., 2012). This poor stratigraphic correlation among sites separated by tens to hundreds of kilometers increases the likelihood of misclassification of a dated terrace (Table 1.1; Scott, 1960; Madole, 1991; Lindsey et al., 2005).

In our study area, surficial mapping was conducted in the Fremont and Pueblo counties by Scott et al. (1972, 1977). This mapping effort classified and correlated the Rocky Flats, Verdos, Slocum, and Louviers terraces based on their stratigraphy from both sides of the Arkansas River valley and strath elevations of gravel deposits above the Arkansas River referenced to previously reported elevations in the Denver area (Scott, 1960). This mapping also included two mappable allostratigraphic sub-units in the Slocum and Verdos terraces that were not mapped previously in studies north of our study area (Scott et al. 1972, 1977; see below). To our knowledge, since then, no other detailed surficial mapping of fluvial terraces was conducted in our study area.

1.3 Methods

1.3.1 Digital Topographic Analysis and River Analysis

We performed digital topographic analysis to visualize spatial variation in proxies related to relative incision rate in the southern FR. We restricted this analysis to fluvially-dominated bedrock channels that conform to the general assumptions of the detachment-limited incision model. We quantitatively analyzed the topography in the eastern Rockies using a Shuttle Radar Topography Mission (SRTM) 1 arc-second (~30 m horizontal resolution) DEM and conducted a drainage network analysis using TopoToolbox v2 (Schwanghart and Scherler, 2014) and ChiProfiler (Gallen and Wegmann, 2017). We delineated the drainage network of the eastern Rockies as areas draining ≥ 10^6 m^2, which based on log-transformed S and A, is above the hillslope-fluvial transition where hillslope processes (e.g., debris flows) affect topography (Figure A1; Snyder, 2000; Wobus et al., 2006; Kirby and Whipple, 2012). We calculated a regional-scale channel θ_{ref} by taking the average of two different methods available in TopoToolbox - a Bayesian optimization function 'mnoptim' and a variance minimization function 'mnoptimvar' (equations 6,7) - to recover an average θ_{ref} of 0.39 (Figure A2). We used this value and ChiProfiler to calculate k_{sn} from χ across the eastern Rockies drainage network using a smoothing window average of 300 m (e.g., Gallen and Wegmann, 2017). To aid in visualization of k_{sn} spatial patterns, we interpolated k_{sn} across the drainage network to produce a regional k_{sn} map using kriging in ESRI Arc Pro 2.8.3 at resolution of 500 meters.

For each basin in the eastern Rockies drainage network (Figure 1.1), we conducted a detailed river profile analysis of fluvially-dominated bedrock tributary trunks. We excluded basins that show significant alluviation and glacial scouring, based on 1:62,500 geological maps (Taylor et al., 1975a; Epis et al., 1979; Wobus et al., 1979), inspection of Google Earth imagery, and field observations. We found that these basins were mostly located west and south of the Arkansas River in channels that drain the Sangre de Cristo and Wet Mountains (Figure 1.1). In the field, we also noted minor alluvial backfill in lower reaches of some tributaries north of the Arkansas River. This fill is thin (<5 m), and the transition from bedrock to thin alluvial cover channel does not correspond with changes in slope in our χ-plots. We, therefore, assume that this backfill is transient and short-lived and has little influence on the long-term evolution of the analyzed bedrock river profiles.

We used ChiProfiler and TopoToolbox to perform river profile analysis on fluvially-dominated bedrock channels. We identified main stem knickpoints following the criteria that the difference in k_{sn} between upstream and downstream reaches is greater than 25% (Figure 1.2C; Table 1.2; e.g., Gallen and Wegmann, 2017). We manually inspected knickpoint locations on tributary trunks in the context of geological maps, Google Earth imagery, and in the field to ensure they are not related to local variations in lithology or valley aggradation (e.g., Crosby and Whipple, 2006; Haviv et al., 2010; Forte et al., 2016). For instance, we analyzed the potential role of lithological variability on knickpoint formation by classifying main lithological units from digitized geological maps (Green, 1992) using Arc Pro Spatial Analyst. We used Matlab to map and project these digitized geological units onto river profiles to allow easy examination and refute correlations between changes in lithology and knickpoint locations. Similarly, we refuted the role of pre-existing faults on knickpoint formations by comparing knickpoint locations with existing pre-Quaternary and Quaternary faults in our study area (USGS archive).

To verify that the selected tributary trunk channel knickpoints are associated with other knickpoints throughout the tributary network, we compared knickpoint locations with k_{sn} spikes in the basin-wide χ-binned inversions. This analysis is similar to studies that rely on the generic knickpoint celerity model to test if a series of knickpoints within a drainage basin are related (e.g., Crosby and Whipple, 2006; Berlin and Anderson, 2007; Gallen et al., 2013; Miller et al., 2013), but has the advantage of using all data in the river network instead of only using data from specific knickpoint locations (Appendix A; e.g., Gallen, 2018; Pavano and Gallen, 2021). We also used these basin-wide χ-binned inversions to confirm that recent capture events in upper reaches of some of our analyzed tributaries (as seen by Google Earth imagery and in our river profiles in χ space) did not impact knickpoint retreat rates since their migration from the basin outlets that confluence with the main stem of the Arkansas River (e.g., Whipple et al., 2017; Giachetta and Willett, 2018).

We calculated paleo-channel profiles and total incision magnitudes for the analyzed tributaries using k_{sn} regressions above knickpoint locations (Figure 1.2C; e.g., Gallen et al., 2013; Gallen and Thigpen, 2018; Mitchell and Yanites, 2019). We analyzed all mapped knickpoints and tributary trunks to quantify χ and elevation at knickpoint locations, k_{sn} in reaches above and below knickpoints, and total incision magnitudes at tributary outlets, where the knickpoint χ was calculated from a common base level of the modern Arkansas River near Canon City (i.e., the FR mountain front) to assess if the knickpoints are genetically related.

1.3.2 Terrace Mapping and Analysis

We mapped a flight of six terraces along the Arkansas River valley in the western High Plains using a Colorado GeoData Cache post-2013 flooding digitized LiDAR survey, with a positional horizontal accuracy of ± 73.4cm at 95% confidence level and non-vegetated vertical accuracy of ± 7.84cm at 95% confidence level (Merrick & Co, 2019). The preliminary identification and correlation of the mapped terraces included: (1) digitizing the surficial mapping by Scott et al. (1972, 1977); (2) generating 28 cross-sections of 4-6 km across the Arkansas River Valley at 1 km intervals from Canon City downstream to Pueblo using Google Earth imagery; (3) mapping terrace treads from our LiDAR data; (4) conducting in-situ descriptions of sedimentological characteristics of each terrace level in the field (Table 1.1); (5) verifying terrace locations and measuring strath elevations and alluvial fills above strath levels in the field using GPS and Laser Rangefinder (Table A1); (6) comparing our mapping and field observations to previous mapping and descriptions north of our study area (Table 1.1; Scott, 1960; Madole, 1991; Lindsey et al., 2005; Riihimaki et al., 2006; Dühnforth et al., 2012).

Since previous studies north of our study area showed a wide range of ages for the same terrace classification (see above; Table 1.1; e.g., Riihimaki et al., 2006; Dühnforth et al., 2012), we based terrace names and classifications on the surficial mapping by Scott et al. (1972, 1977) and published terrace elevations from previous studies that showed consistency with elevations of mapped terraces across the Arkansas River in our study area (Table 1.1). We termed the terraces Ql, Qs, Qv, and Qrf after Louviers, Slocum, Verdos, and Rocky Flats, respectively, where the Qs and Qv terraces were sub-divided to Qs1, Qs2, Qv1, Qv2, respectively, based on the classification and mapping by Scott et al. (1972, 1977).

To best represent strath elevations of the mapped terraces and minimize issues associated with using terrace treads for calculating total incision (e.g., Wegmann and Pazzaglia, 2009), we projected only river-facing edge points of each mapped polygon (i.e., lowest elevation points) to a line that cross the Arkansas River valley from Canon City downstream to Pueblo. Since maximum alluvial fills of the terraces observed in the field did not exceed 5 m on average (i.e., a thin alluvial fill with little local relief; Table A1), we considered the river-facing edge points of the mapped terraces as strath locations under a reasonable uncertainty. We used these approximate strath locations to estimate a pre-erosion continuous strath profile for each terrace level by calculating linear and power-law regressions for each terrace level data set. We verified the elevation predictions of the regressions with field-measured straths elevations and alluvial fill thicknesses (Table A1). We calculated the total incision from each of the continuous modeled strath profiles to a paleo-river profile regression of Holocene terraces along the Arkansas River valley (using the same technique as for the Pleistocene terraces) to avoid potential biases introduced by the dynamic reference of the modern-day Arkansas River (e.g., Finnegan et al., 2014; Gallen et al., 2015).

To independently verify our terrace classification and downstream strath profiles (cf. Zhu et al., 2021), we calculated two-dimensional hypsometry of the LiDAR data to assess downstream mapping correlations with the projected strath locations. We first removed "non-flat" areas using slope and curvature thresholds of 5° and ± 0.005, respectively. The remaining elevation data was binned in 25 m increments in the downstream direction, tallied in 1 m elevation increments to get pixel frequencies (i.e., hypsometry), and projected onto a line that crosses the Arkansas River valley. When discrepancies were noted between the LiDAR analyses and our projected strath locations, we iteratively revised and updated the mapping and terrace correlations accordingly.

1.3.3 Flexural and Geomorphic Analyses

We calculated the correspondent flexural isostatic response to the removal of a Rocky-Flats paleo surface across the Arkansas River valley in the western High Plains. We reconstructed this surface by extrapolating mapped Rocky Flats treads in our study area with remnants of Rocky Flats deposits from previous mappings downstream of our study area (Figure 1.1; Sharps, 1976). We differenced the extrapolated paleo-surface from the modern topography along the Arkansas River valley to approximate differential erosion across the western High Plains. Because the correlation and preservation of Rocky Flats remnants downstream our study area are rough (i.e., not based on the LiDAR data), we selected and digitized only Arkansas River facing polygon edges within 7 km of the Arkansas River active channel (see above; Figure 1.1). By doing so, we considered the inferred eroded volume from the calculated paleo-surface as a maximum estimation of differential erosion and a conservative test for the isostatic component magnitude on the overall deformation in the High Plains. To calculate the isostatic rebound to this unloading, we used a 2D flexural-isostatic model (Appendix A) under a range of elastic thicknesses, T_e, from 5 to 15 km; mantle density, $\rho_m = 3300\ kg/m^3$, crust/infill density,$\rho_c = 2500\ kg/m^3$, Young's modulus, $E = 10^{11} Pa$, and Poisson's ratio, $v = 0.25$, based on previous geophysical studies in the region (e.g., Hansen et al., 2013; Lazear et al., 2013).

To complement our terrace and flexural analyses, we conducted geomorphic analyses along the active channel of the Arkansas River to explore the potential variable incision rates in the western High Plains (e.g., Schumm et al., 2002; Burbank and Anderson, 2011). We digitized the Arkansas River active channel from Canon City downstream to Pueblo (Figure 1.1) using Google Earth and Arc Pro. We calculated the Arkansas River sinuosity and k_{sn} using TopoToolbox, and binned and calculated the channel distance, slope, width, and stream power at 500 m streamwise distance bins along the channel center line using TopoToolbox and ChanGeom (Fisher et al., 2012, 2013).

1.4 Results

1.4.1 River profile and knickpoint patterns in the Eastern Rockies

Excluding drainage basins in the eastern Rockies that contained evidence of recent glaciation or heavy alluviation (Figure 1.1, Figure 1.3), tributary trunk knickpoints in the fluvially-dominated bedrock channels north of the Arkansas River are all normal knickpoints that correlate with k_{sn} spikes in the basin-wide χ-binned inversions (Figure 1.4). Generally, these knickpoints do not correlate with lithological changes or pre-existing faults across the eastern Rockies drainage network (Figure 1.4, Figure A4; USGS archive).

Regionally, the tributary trunks north of the Arkansas River, where the knickpoints are located, change their flow orientations from NE-SW between Salida downstream to Cotopaxi to NW-SE between Cotopaxi downstream to Canon City (Figure 1.1, Figure 1.3, Figure 1.4). The regional k_{sn} patterns for these tributaries (Figure 1.3C) show little change in k_{sn} among primary rock types but do show increased k_{sn} moving downstream along the tributary trunks towards their basin outlets (Figure 1.3A, Figure 1.4). k_{sn} along the main stem of the Arkansas River shows a gradual decrease from Salida downstream to Cotopaxi and an increase from Cotopaxi downstream to Canon City (Figure 1.3C). Interestingly, the regional changes in tributary trunks flow orientations and the overall increase in k_{sn} downstream of Cotopaxi spatially correlate with a sharp kink in the main stem of the Arkansas River from NW-SE to SW-NE at the same area (Figure 1.3).

All the normal knickpoints fall roughly within two bands of χ values when calculated from a common base level near Canon City (i.e., the FR mountain front; Figure 1.5A): (1) χ of ~15 that is found in channels containing a single knickpoint or for higher knickpoints in channels that contain two knickpoints; (2) χ of ~8 for lower knickpoints in channels containing more than a single knickpoint. Knickpoints with χ ≈ 15 rise in elevation from ~200 m directly west of Cotopaxi to ~800 m near the Royal Gorge (Figure 1.5B). Similarly, knickpoints with χ ≈ 8 rise in elevation from ~200 m to ~400 m across the same distance (Figure 1.5B). Based on this clustering of knickpoint χ and elevation patterns, we define an older, higher set of normal knickpoints (red in Figure 1.4, Figure 1.5A,B) and a younger, lower set of normal knickpoints (cyan in Figure 1.4, Figure 1.5A,B) that propagated from a common base level fall downstream the eastern Rockies. The single knickpoint at Salida (Figure 1.5) stands out from the rest of the knickpoints, and there is not enough data to determine if this knickpoint is spurious or relates to a real trend further upstream the Arkansas River. Given this uncertainty, we treat this knickpoint as spurious and ignore it from our interpretations herein forward.

The distribution of k_{sn} in the tributaries between Salida downstream to Canon City is consistent with the distribution and elevation of the identified knickpoints. k_{sn} along the upper-most reaches (i.e., above highest knickpoints in all the channels) is ~20 - 30 $m^{0.78}$ (Figure 1.4, Figure 1.5C - purple points; Table 1.3). For the section between Salida downstream to Cotopaxi, k_{sn} for reaches below the higher knickpoints is 33 - 100 $m^{0.78}$ (Figure 1.4, Figure 1.5C – red points; Table 1.3). In tributaries between Cotopaxi downstream to Canon City, where two sets of normal knickpoints are observed, k_{sn} for reaches below the higher knickpoints is decreasing from 50 $m^{0.78}$ near Cotopaxi to 30 $m^{0.78}$ near the Royal Gorge (Figure 1.4, Figure 1.5C – red points; Table 1.3). For reaches below the lower knickpoints at the same section, k_{sn} is ~65 – 75 $m^{0.78}$ (Figure 1.4, Figure 1.5C – cyan points; Table 1.3). Overall, in all the tributaries, k_{sn} is gradually increasing moving downstream the tributary trunks, with general k_{sn} ratios of lower to upper reaches of ~1 - 3, with higher ratios of ~6 near Salida and ~3 - 4 west of Cotopaxi (Figure 1.4, Figure 1.5C; Table 1.3).

The total magnitude of incision depth from the reconstructed relict reaches above the highest knickpoints (Figure 1.4; red dashed lines) is 518 m in Salida, 52 m west of Cotopaxi, a gradual increase from ~52 m near Cotopaxi to ~560 m west of the Royal Gorge area, and ~320 m near the Royal Gorge (Figure 1.5D). The total magnitude of incision depth with respect to the lower knickpoint set (Figure 1.4,; cyan dashed lines) is 85 m at ~10 km downstream from Cotopaxi, gradually increasing to ~220-250 m near the Royal Gorge area (Figure 1.5D).

Overall, the analysis of tributary trunks north of the Arkansas River shows an increase in knickpoint elevations and total incision depths (Figure 1.5B,D) as a function of downstream distance along the Arkansas River from west of Cotopaxi to the Royal Gorge. For the section between Cotopaxi to the Royal Gorge, k_{sn} is similar for different reaches of tributary trunks, with a gradual downstream increase in k_{sn} toward their confluences with the main stem of the Arkansas River (Figure 1.5C).

1.4.2 Terraces patterns in the Western High Plains

Six Pleistocene terrace levels in the western High Plains from Canon City downstream to Pueblo were mapped and identified (Figure 1.6). The topographically highest (~100 m above the Arkansas River) and stratigraphically oldest allostratigraphic unit in the study area is the Rocky Flats terrace (Qrf in Figure 1.6A; Table 1.1). This unit is ~3-5 m thick and composed of sandy gravel with 2-30 cm diameter rounded cobbles of diverse provenance, including granite, pegmatite, granodiorite, and schist. These cobbles are chemically decomposed and have weathering rinds of several mm to cm thick, with a well-developed, m-thick, stage III+ calcic soil tread (Figure 1.6B; Table 1.1, Table A1).

The next set of allostratigraphic units mapped at ~75 - 85 m and ~55 - 65 m above the Arkansas River are the upper and lower Verdos terraces (Qv1 and Qv2, respectively; Figure 1.6A). These terraces are composed of ~1-5 m of upward-fining, mostly subangular, imbricated sandy gravel with clasts ranging from ~2-40 cm, consisting of granodiorite, K-spar rich pegmatite, and a small amount of schist, embedded in well-developed, red-colored, oxidized soil profiles (Figure 1.6C; Table 1.1, Table A1).

Stepping down to terraces at ~35 - 45 m and ~25 - 35 m above the Arkansas River are the upper and lower Slocum terraces (Qs1 and Qs2, respectively; Scott et al. 1972, 1977; Figure 1.6A). These units are characterized by rounded cobbles and pebbles of granodiorite, mostly in Qs2, transitioning to angular cobbles and boulders in a partly oxidized matrix in the upper Qs1 surface, with mean alluvial fills of ~2 - 6 m for Qs2 and ~3 - 10 m for Qs1 (Figure 1.6; Table 1.1, Table A1).

The lowest and youngest allostratigraphic unit in our study area is the Lovuiers alluvium (Ql). This terrace lies ~15 - 25 m above the Arkansas River (Figure 1.6A) and is characterized by ~0.6 - 1 m fine silt/loess material lying on top of a ~3-4 m thick channel facies with south-oriented imbricated cobbles of 10-50 cm (Figure 1.6E; Table 1.1, Table A1). In some of these terrace treads, the alluvium is topped with disseminated detrital charcoal, which might or might not be an in-situ deposit.

Younger allostratigraphic units at an elevation of 3 m or less from the modern-day Arkansas River (i.e., not the Broadway terrace) and the Arkansas River flood plain are all Holocene in age and are lumped in this study as one unit that is used as a reference frame for incision calculations (e.g., Finnegan et al., 2014; Gallen et al., 2015; see Methods).

Our terrace mapping and classification from the LiDAR data and Google Earth imagery (Figure 1.7A) agree with our GPS, strath elevations, and alluvial fill measurements from the field (Figure 1.6, Figure 1.7B; Table 1.1, Figure A1). High-density regions in our LiDAR hypsometry show a good correlation with our mapped terraces, field measurements and inferred downstream correlations (Figure 1.8). Power law and linear regressions over the projected strath river-facing edge points are $R^2 = 0.86$ for the Qrf terrace and $R^2 \approx 0.96$-0.99 for the Qv1, Qv2, Qs1, Qs2, Ql, and Holocene terraces (Figure 1.8, Figure A5). Since the terraces show significant deformation, here we prefer to use the power-law fit regressions (Figure 1.8) over the simpler linear fit regressions (Figure A5) for further interpretation of the western High Plains deformation history.

The total incision calculated from the continuous strath profiles to the Holocene terraces paleo-river profile (Figure 1.8) show that for: (1) Ql, total incision is ~17 m near Canon City, grows to ~23 m at ~25 km downstream from Canon City, and diminishes to ~18 m near Pueblo; (2) Qs2, total incision is ~30 m near Canon City, grows to ~32 m at ~25 km downstream from Canon City, and diminishes to ~27 m near Pueblo; (3) Qs1, total incision is ~35 m near Canon City, growing gradually to ~42 m near Pueblo; (4) Qv2, total incision is ~43 m near Canon City, growing gradually to ~61 m near Pueblo; (5) Qv1, total incision is ~77 m near Canon City, growing gradually to ~85 m at ~35 km downstream from Canon City, and diminishes to ~82 m near Pueblo; (6) Qrf, total incision is ~93 m near Canon City, growing rapidly to ~118 m at ~35-40 km from Canon City and diminishes to ~112m near Pueblo.

Strath terrace separation from the Holocene datum display collectively a down-to-the-west fanning pattern with increased total incision moving downstream along the main stem of the Arkansas River from Canon City downstream to Pueblo (Figure 1.8). This fanning pattern is opposite to previously reported fanning patterns north of our study area (Figure 1.2A; Wobus et al., 2010; Dühnforth et al., 2012; Langston et al., 2015), and it is mostly noticed at ~5 - 15 km upstream of Pueblo, where the upper Slocum and lower Verdos terraces (Qs1 and Qv2, respectively) are locally deformed (Figure 1.8, Figure A5).

1.4.3 Flexural and geomorphic patterns in the Western High Plains

The subtraction of the paleo Rocky-Flats surface (~90-100 meters above the Arkansas River) from the modern-day Arkansas River (Figure 1.9A) shows a downstream increase in differential erosion from ~10-20 m near Canon City to ~90-100 m near Pueblo (Figure 1.9B). This differential erosion increases farther downstream to the southeast for another 100 km along the Arkansas River valley from Pueblo and is consistent with valley widening up to ~50 km at this area (compared to ~2-5 km of valley width in our study area; Figure 1.9B). The flexural isostatic rebound from differential erosion under varied elastic thicknesses shows a maximum value of ~4 – 10 m at the same location of the maximum valley widening at ~50 km downstream from Pueblo (Figure 1.9C, Figure A6).

The regional and local geomorphic analyses along the main stem of the Arkansas River in the western High Plains show a reduction in sinuosity from 1.4 to 1.26 at ~30 km downstream from Canon City (Figure 1.10C, inset). Farther downstream at ~37-43 km from Canon City, the main stem of the Arkansas River shows the steepest (up to 0.1, Figure 1.10A), almost narrowest (down to ~30-40 m, Figure 1.10B), and highest stream power (up to ~6e^{8} kg m^{2} s^{-3}, Figure 1.10C) reach, which spatially correlates with the recorded local deformation of the Qv2 and Qs1 terraces at ~5-15 km upstream of Pueblo (Figure 1.8).

1.5 Discussion

1.5.1 Recent incision history in the Eastern Rockies

We interpret the two sets of normal knickpoints in the eastern Rockies (Figure 1.4, Figure 1.5, Figure A3) as recording at least two geologically-recent base level fall events downstream of the FR mountain front (Figure 1.1). We base this interpretation on several observations from our river profile analysis. First, on the tributary-scale, most knickpoints do not correlate with changes in rock type (Figure 1.4, Figure A4) or faults (USGS Archive), but correlate in χ-space with spikes in k_{sn} within each individual basin (Figure 1.4). This indicates that the knickpoints are transient (i.e., not static, e.g., Wobus et al., 2006; Crosby and Whipple, 2006) and have been propagated in a kinematic wave-style from a given tributary confluence with the Arkansas River to current locations. Second, on the eastern Rockies drainage scale, the knickpoints fall into two main χ bands when calculated from a common base level of the Arkansas River near Canon City (Figure 1.5A). This result indicates that two knickpoint sets are genetically related, are the result of a base level fall downstream of Canon City, and that they have been propagated upstream in an overall uniform substrate, climate, and incision processes (Whipple and Tucker, 1999; Kirby and Whipple, 2012; Figure 1.3).

The tributary and knickpoint morphologies are inconsistent with predicted geomorphic patterns of the climate hypothesis (Figure 1.2A-H2). River profiles do not show gradient relaxation, and knickpoints are normal and not inverted (Figure 1.2A-H2; e.g., Wobus et al., 2010). The tributary and knickpoint spatial patterns across the eastern Rockies are also not consistent with predicted geomorphic patterns of an eastward forward tilting that is associated with active tectonics of the Rio Grande Rift (Figure 1.2A - H1, 5; Leonard, 2002; McMillan and Heller, 2006; Abbey and Niemi, 2018). Knickpoint elevations and total incision depths at tributary outlets increase from Cotopaxi downstream to the Royal Gorge, opposite to what is predicted from such a hypothesis.

The spatial patterns in knickpoints and tributary trunks indicate an eastward increase in uplift rates towards the FR mountain front (Figure 1.5B; e.g., Snyder, 2000; Wobus et al., 2006). This finding is more consistent with a tectonic- or geodynamic-triggered base level fall and back tilting. Further, the k_{sn} increase in the downstream direction along tributary trunks indicates that the uplift field is also temporally increasing (Figure 1.5C). The estimated differential uplift of ~400 – 500 m from Cotopaxi downstream to the Royal Gorge (Figure 1.5D) agrees with the location and depth of the Royal Gorge (~320 m), which its narrow valley and local barbed tributaries imply a relatively recent geomorphic feature (Figure 1.1, 5D; Powers, 1935; Clarey et al., 2004; Abbey et al., 2017). Thus, the gorge formation is also better explained by the interpretation of differential uplift and back tilting, in contrast to previous studies that struggled to explain it in the context of forward (downstream) tilting (Figure 1.2-H1; Powers, 1935; Leonard, 2002; Abbey et al., 2017).

1.5.2 Incision processes in the Western High Plains during the Quaternary

Based on published age estimates and our mapping, a rough estimate of the average incision rate along the Arkansas River in the western High Plains since the early Pleistocene is ~0.1 – 0.2 mm/kyr (Figure 1.8, Figure A5). Yet, this incision is not steady nor uniform (Figure 1.8). The downstream fanning pattern (i.e., terraces tilted to the west) mimics the back tilting signal recovered from our river profile analysis in the eastern Rockies (Figure 1.5B,D). Consistent with the river profile results, this west-directed tilting is inconsistent with climate-induced relaxation of the Arkansas River or deformation patterns predicted from the hypothesis of a tectonic induced eastward tilting (Figure 1.2).

The local deformation of the Qv2 and Qs1 terraces at ~5 - 15 km upstream of Pueblo (Figure 1.8) spatially correlates a zone of narrowing, steepening, and increased stream power of the main stem of the Arkansas River (Figure 1.10). This result is consistent with deformation patterns in other modern bedrock channels above active tectonic uplifts (e.g., Ouchi, 1985; Holbrook and Schumm, 1999; Lavé and Avouac, 2000; Schumm et al., 2002; Turowski et al., 2006; Burbank and Anderson, 2011; Marder et al., 2018). A parsimonious explanation for this local deformation is motion on an unrecognized fault or faults beneath the Arkansas River (Figure 1.8, 11). This is a reasonable interpretation given that there are several other faults identified in the western High Plains with documented Quaternary rupture on them (e.g., Widmann, 1997a,b; Crone and Haller, 2015). However, this does not explain why a fault might be active in this location, a point which we return to later in the discussion.

The estimated flexural isostatic rebound triggered by differential erosion in the western High Plains cannot explain the observed broad back tilting pattern of the Pleistocene fluvial terraces (Figure 1.9, Figure A6). While this differential uplift is similar to the amount of the tilt of the terraces (~several meters to tens of meters), the locus of flexural rebound is too far downstream to explain the terrace fanning pattern and the local deformation at ~5 – 15 km upstream of Pueblo (Figure 1.8).

Combining, the evidence of (i) recent local scale uplift and active tectonics at ~5 - 15 km upstream the Arkansas River from Pueblo (Figure 1.8, 10), (ii) an intermediate scale signal of down-to-the-west back-tilting fanning pattern from Canon City downstream to Pueblo (Figure 1.8), and (iii) the longer wavelength crustal-scale back-tilting signal across the eastern Rockies and the western High Plains, are all inconsistent with previously suggested hypotheses (Figure 1.2A). As such, our results require an alternative mechanism to explain the recent landscape unsteadiness in the southern FR.

1.5.3 A geodynamic model to explain recent landscape unsteadiness in the southern FR

Studies by Moucha et al. (2008, 2009) suggested a migrating wave of dynamic topography that swept northeastward through the southwestern US to the central US during the last 30 Ma. According to this geodynamic model, the wavelength of dynamic topography is ~100 - 200 km with potential surface uplift of 100 - 300 m once reaching the FR at ~5 Ma (Moucha et al., 2009). Based on this model, from ~5 Ma to the present day, the wave of dynamic topography migrated eastward through the eastern Rockies and later through the western High Plains with respect to a fixed North America reference frame, with a current locus of maximum dynamic topography somewhere in eastern Colorado. The migrating dynamic topography model by Moucha et al. can explain the long-wavelength west-directed back tilting patterns recorded in tributary networks in the eastern Rockies and in river terraces in the western High Plains (Figure 1.11). Importantly, the model predicted wavelengths and surface uplift magnitudes (Moucha et al., 2009) are roughly consistent with the deformation across the southern FR (~100 km) and the magnitude of incision in the eastern Rockies and western High Plains (up to ~400 m and ~100 m, respectively; Figure 1.5, Figure 1.8, Figure 1.11).

Nevertheless, while the general patterns of deformation gleaned from our study are broadly consistent with the dynamic topography model of Moucha et al. (2008, 2009), several features identified in our results, namely the two-phase base level fall history in the eastern Rockies and the local deformation in the western High Plains, require a more nuanced interpretation. The simplest explanation for the recorded two-phase base level fall history in the eastern Rockies is incision through sub-horizontal sedimentary units with variable erodibility in the western High Plains (cf. Forte et al., 2016; Gallen, 2018).

This mechanism can alter and/or augment the steady base level fall associated with the long-wavelength dynamic topography, resulting in punctuated steps of base level drop during the late Cenozoic. The local deformation in the western High Plains can be explained by reactivation of pre-existing faults or fractures by perturbation of the upper crust stress state due to crustal warping associated with the propagating wave of dynamic topography (Figure 1.11A). If correct, this stress perturbation can reactivate pre-existing structures optimally oriented in the regional stress field (cf. Gallen and Thigpen, 2018), thereby generating shorter wavelength deformation due to slip on reactivated structures. Thus, the two-phase base level fall history in the eastern Rockies and the local deformation in the western High Plains are expected landscape responses (given the local geology) and are consistent with our interpretation of an eastward migrating wave of dynamic topography that swept the southern FR during the late Cenozoic.

This geodynamic interpretation does not necessarily refute other tectonic and climatic mechanisms for transient landscape evolution elsewhere in the FR. For instance, the geodynamic driver in the southern FR might decay moving north or south of our study area, allowing other drivers, such as climate, to play a more prominent role in driving transient landscape evolution. Future research focused on detailed reconstructions of the landscape evolution history of different portions of the FR will elucidate the myriad of mechanisms and processes driving landscape dynamics in this setting.

1.6 Summary and Conclusions

We performed different tectonic geomorphology analyses in the eastern Rockies and western High Plains provinces to resolve incision patterns along the main stem of the Arkansas River and main driver(s) for recent landscape unsteadiness in the southern FR. In the eastern Rockies, we conducted river profile analysis on tributary trunks of the Arkansas River to recover the relative base level fall history between Salida, CO downstream to Canon City, CO. We find that topographic metrics along these tributary trunks (e.g., knickpoint elevations, incision depths at basin outlets, k_{sn} downstream tributaries) all increase from Cotopaxi downstream to Canon City. In the western High Plains, we mapped and correlated six Pleistocene fluvial terraces across a 50 km transect along the Arkansas River valley from Canon City, CO downstream to Pueblo, CO. We find that these terraces record increased incision magnitudes as a function of downstream distance along the Arkansas River. We also find that these terraces record an uplifted local deformation younger than ~300 ka at ~5-15 km upstream from Pueblo, which spatially correlates a zone of narrowing, steepening, and increased stream power along the Arkansas River.

These recorded geomorphic patterns across the southern FR, supported by a flexural analysis, are inconsistent with previously suggested prevailing hypotheses of a climate-induced enhanced erosional efficiency during the Quaternary (Wobus et al., 2010; Langston et al., 2015) or eastward tilting associated with the Rio Grande Rift (Leonard, 2002; McMillan and Heller, 2006; Abbey et al., 2018). Rather, these geomorphic patterns are more consistent with a regional long-wavelength deformation with a down-to-the-west back tilting signal and recent, localized deformation in the western High Plains. This agrees with a previously suggested geodynamic model by Moucha et al. (2008, 2009) that predicts a wavelength dynamic topography of ~100 km, surface uplift of up to ~400 m, and active tectonics in the western High Plains during the late Cenozoic.

Our study results and interpretation shed light on the ongoing controversy surrounding the main drivers for recent landscape unsteadiness in the FR and bolster the role of geodynamics as the main driver for its southern section. The study also highlights the importance of using geomorphic markers to resolve recent landscape unsteadiness deformations in post-orogenic settings and the imprint of tectonics and climate processes over short to intermediate time scales in other similar settings.

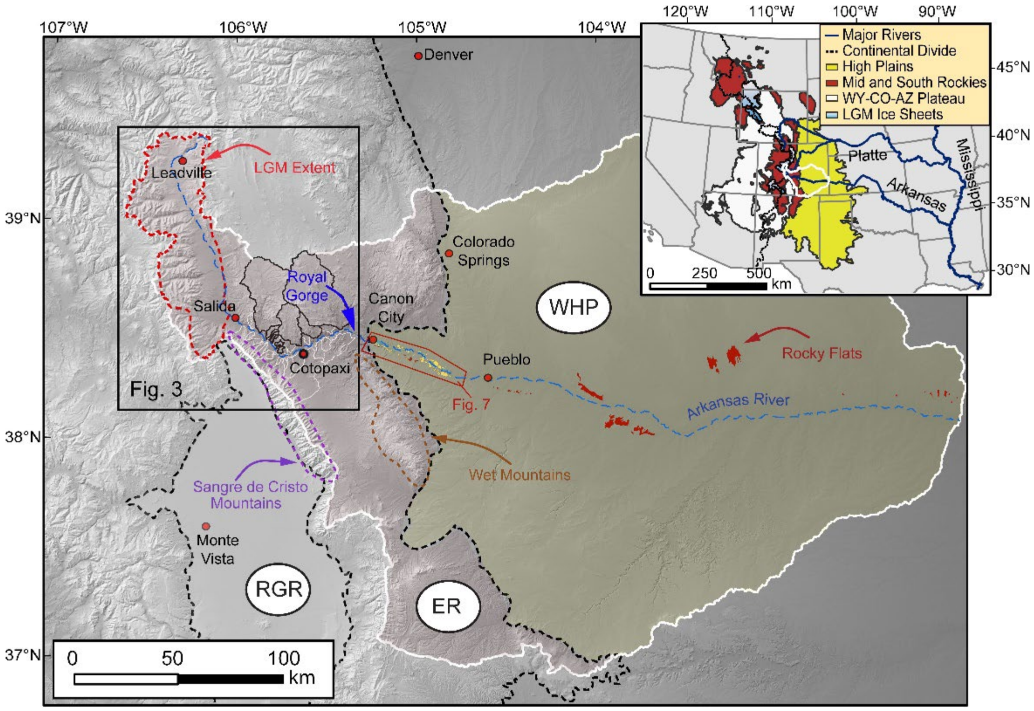

Figure 1.1 ***(A) (Inset)*** *Regional map of main physiographic provenances, glacial extents, and rivers surrounding the Arkansas basin (white polygon).* ***(Main)*** *Main physiographic provenances across the Arkansas basin and the southern Colorado Front Range: the eastern Rockies (ER, red), western High Plains (WHP, yellow), and the Rio Grande Rift (RGR, white). In the eastern Rockies, the excluded alluvial/glaciated basins (white polygons) and the analyzed basins (black polygons) are marked. In the western High Plains, the analyzed fluvial terraces (colored polygons) and their extent from Canon City, CO to Pueblo, CO (red polygon) are marked as well. Also marked are the areas affected by alpine glaciers during the Last Glacial Maximum (LGM, red dashed polygon), the Sangre de Cristo mountains (purple dashed polygon), the Wet Mountains (brown dashed polygon), and mapped treads of the Rocky Flats terraces downstream of our study area (Sharps, 1976) that were used for the flexural analysis.*

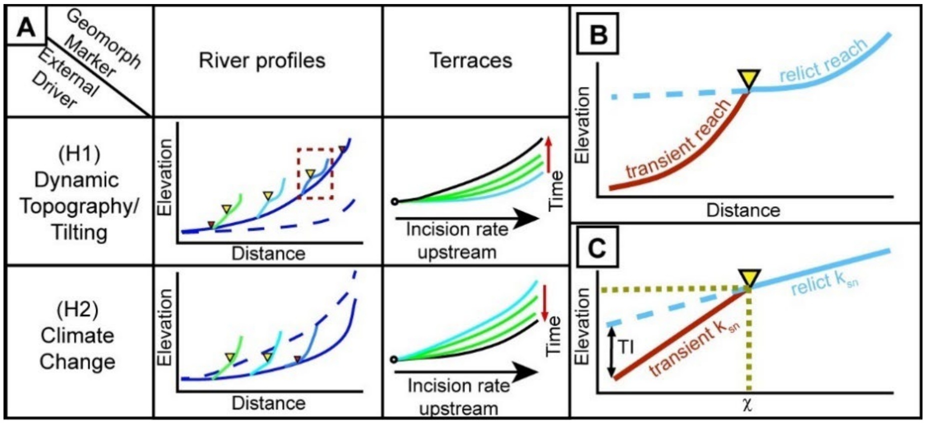

Figure 1.2 ***(A)*** *Predicted geomorphic representations for bedrock river profiles and fluvial terraces for the prevailing tectonic and climate hypotheses that are suggested for recent landscape unsteadiness in the Front Range. In the case of tectonic-induced forward tilting and differential uplift rate (H1), normal knickpoints are generated and migrate up through the main stem tributaries at different vertical rates to show an increased elevation pattern toward the tectonic loci. Below these knickpoints, river profiles will have higher steepness than reaches above them. Fluvial terraces will tilt and have steeper profiles over time, with higher and older terraces showing maximum integrated deformation. A detailed representation of the predicted response for knickpoint migration in a tributary of the main river for H1 (red dashed rectangle) is shown in (B) and (C). In the case of increased erodibility triggered by climate modulations (H2), inverted knickpoints will be generated and migrate up the tributaries. Since under this scenario, the uplift is uniform, knickpoints will migrate vertically at the same rate and will be located in the same elevation band. Below these knickpoints, river profiles will have lower steepness than for reaches above them (i.e., reversed river profiles and patterns than the ones shown in (B) and (C)). Fluvial terraces will show a relaxation pattern that mimic the shoaling of the paleo-river profiles over time.* ***(B)*** *Detailed representation of the relict (blue line) and adjusted (red line) reaches during a slope break normal knickpoint migration from a tributary outlet as a response to increased tectonic uplift rate in elevation-distance space.* ***(C)*** *Same as (B), but in elevation-χ space, where the slope of the linear line is k_{sn} (equation 7). In both B and C, the dashed blue lines show the estimated paleo-river profile prior to the knickpoint formation that is used to calculate total incision (TI) since the local base level fall at the tributary outlet.*

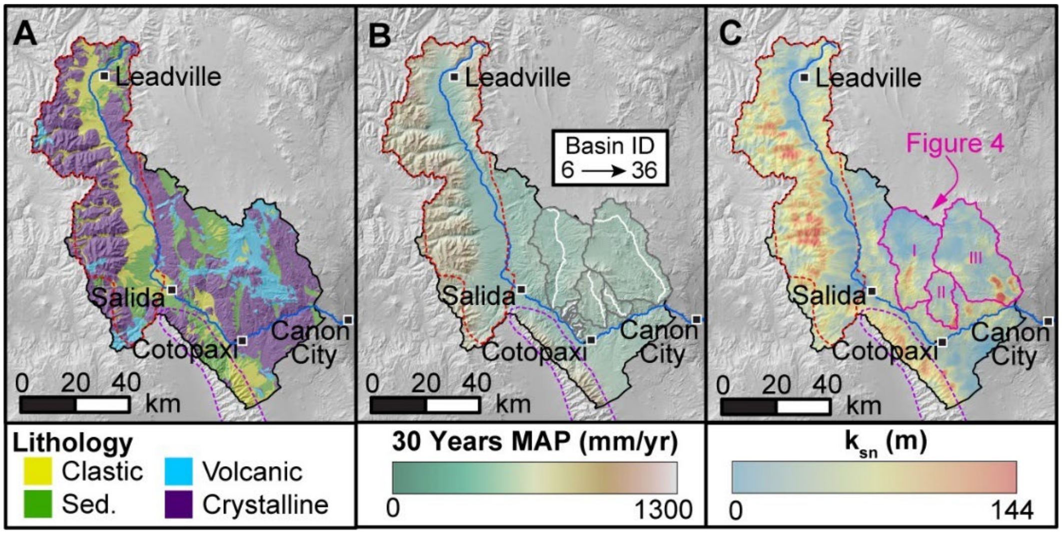

Figure 1.3 ***(A)*** *Simplified lithologic map of the Arkansas River basin upstream of Canon City (after Green, 1992).* ***(B)*** *30-year average mean annual precipitation map (after Fick and Hijmans, 2017) with the analyzed basins drawn on top of it. The basin identification numbers that are mentioned in Table 1.2, Table 1.3, and Figure A4 are increasing as a function of downstream distance along the Arkansas River (blue line).* ***(C)*** *Regional-scale normalized steepness index (k_{sn}) map of the eastern Rockies province within the Arkansas River basin. Magenta colored basins are shown in detail in Figure 4. The LGM alpine ice extent (red dashed line) and the Sangre de Cristo mountain range (purple dashed line) are shown for reference.*

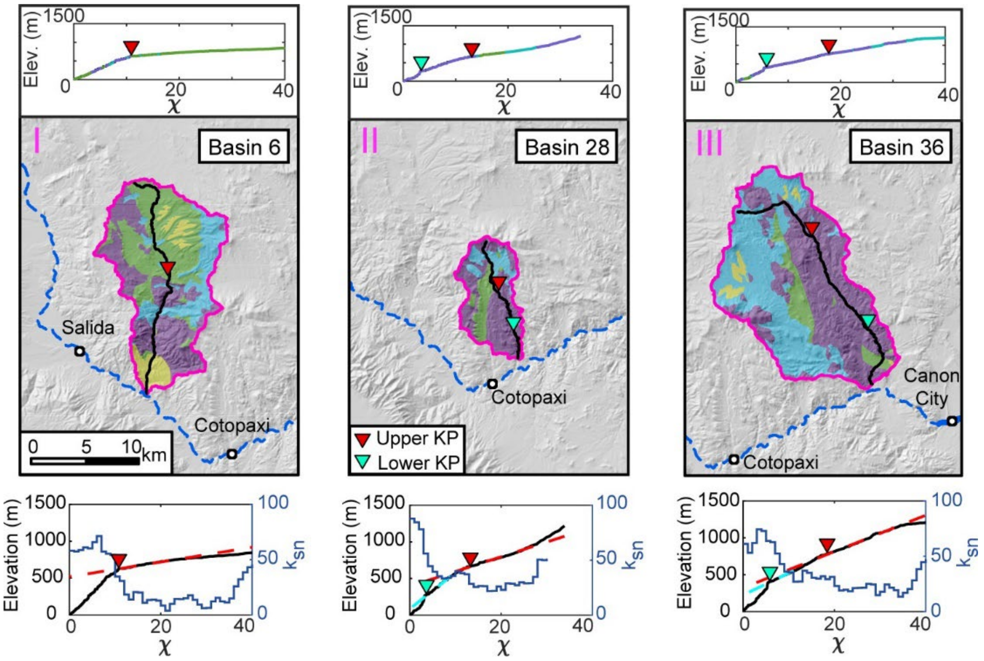

Figure 1.4 River profile analysis results for tributary trunks along basins that are marked in Figure 1.3C. ***(Top)*** *Tributary profiles lithology and knickpoint locations.* ***(Main)*** *Map view of the tributary basins (magenta lines), their trunk channels (black lines), and knickpoint locations (red and cyan triangles) over main lithological units.* ***(Lower)*** *River profiles (black lines) and locations of upper (red triangles) and lower (cyan triangles) normal knickpoints, compared with basin-wide* χ*-binned* k_{sn} *linear inverse model results (blue lines). The lower basins closer to the Front Range mountain front (II, III) show a second set of slope break normal knickpoints (cyan triangles) that do not appear in the upper basins (I). Dashed lines in the lower panels are the calculated paleo-river profiles based on* k_{sn} *in upper reaches above knickpoints. These projected paleo-river profiles are used to calculate the total incision and base level fall at the basin outlet (e.g., Figure 1.2C). For a full analysis of all basins and main channels, see Table A1.*

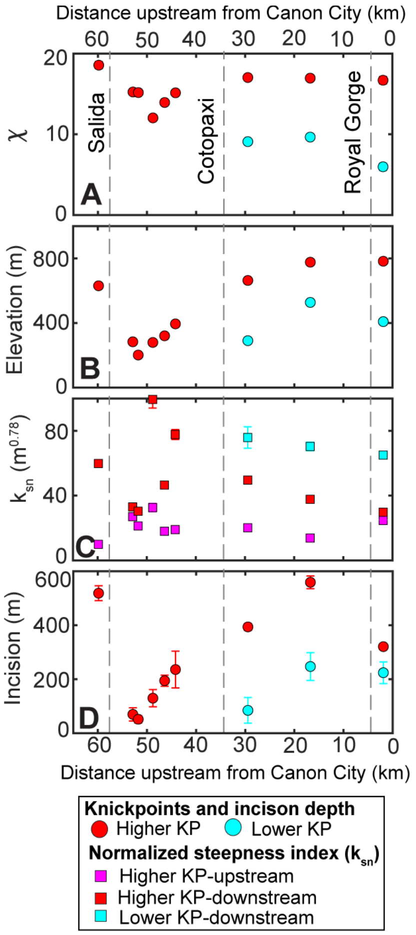

Figure 1.5 Summary (see also Table 1.2 and Table 1.3) of the eastern Rockies river profile analysis results. ***(A)*** *knickpoint χ-distance from a common base level of the Arkansas River near Canon City.* ***(B)*** *knickpoint elevations from basin outlets.* ***(C)*** *k_{sn} for different river segments separated by knickpoints.* ***(D)*** *total incision depth at the tributary basin outlet. All data is plotted as a function of downstream distance of tributary outlets along the main stem of the Arkansas River. Main towns and the Royal Gorge are noted for spatial reference (dashed gray lines). The upper and lower knickpoint sets in (A) show χ values that are roughly the same, indicating that the knickpoints are genetically related and sourced from a common base level fall of the Arkansas River near the Front Range mountain front (or further downstream). For the section between west of Cotopaxi to the Royal Gorge, knickpoint elevations in (B) and incision depths at basin outlets in (D) increase to the east. For the section between Cotopaxi to the Royal Gorge, a second set of lower elevation normal knickpoints is generated, and k_{sn} values in (C) are increasing along tributary trunks from the upper reaches to the lower reaches. For all the panels, data symbols without visual error bars are larger in size than their measured error.*

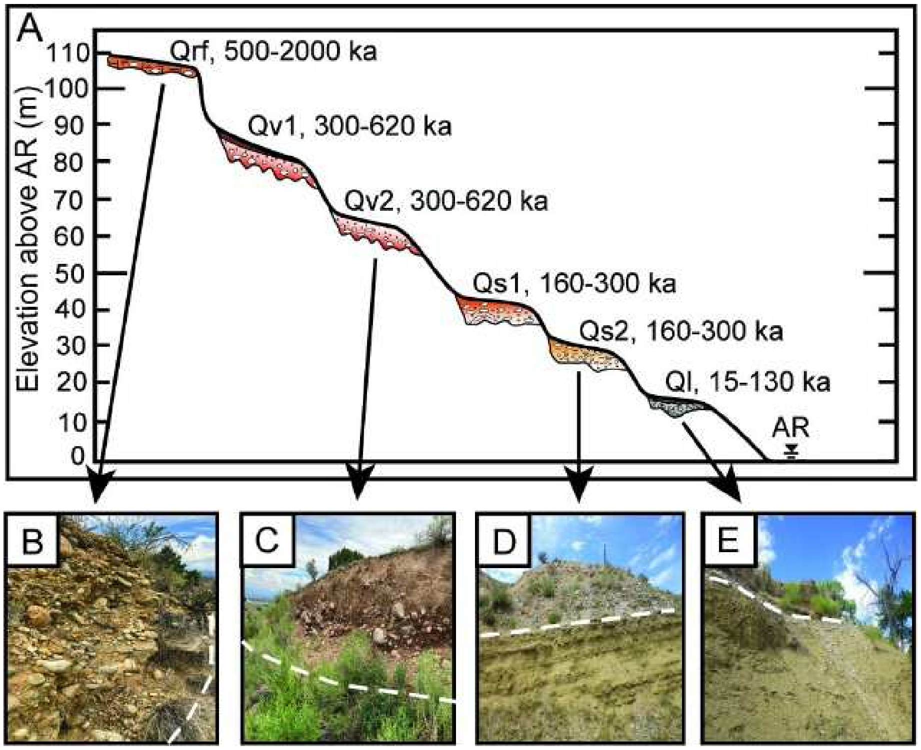

Figure 1.6 ***(A)*** *Stratigraphic-age model for the six allostratigraphic units/terraces identified in the western High Plains. The elevation, color, clast size, and alluvial fill thickness are representative of the surfaces' soils and stratigraphy as seen in the field (Table 1.1, Table A1).* ***(B-E)*** *photos of the Rocky Flats, Verdos, Slocum, and Louviers terraces that were taken in the field. For all the photos, the white dashed lines show the strath locations.*

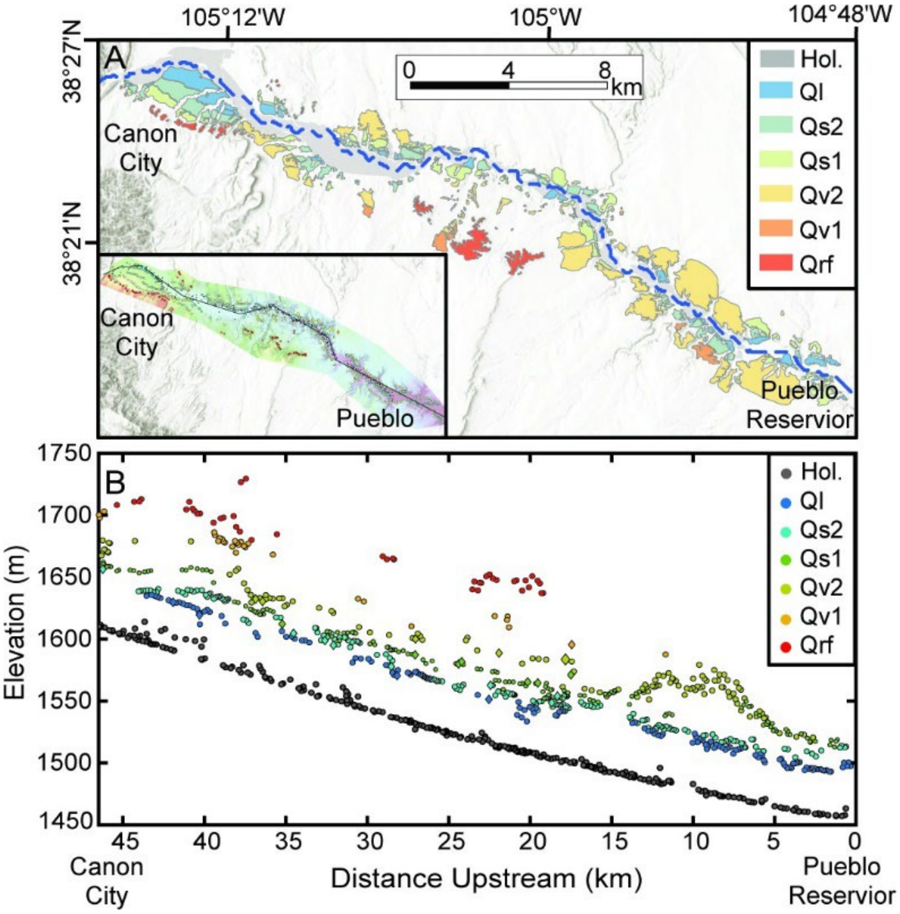

Figure 1.7 ***(A)*** *Surficial mapping of the Pleistocene terraces between Canon City and Pueblo. Nomenclature of these terraces is after Scott et al. (1972, 1977): Qrf - Rocky Flats; Qv1 – Verdos (upper); Qv2 – Verdos (lower); Qs1 – Slocum (upper); Qs2 – Slocum (lower); Ql – Louviers. The Arkansas River (blue dashed line) is marked for reference.* ***(Inset)*** *Tread river-facing edge points that were projected onto the trace of the Arkansas River valley (black line) to generate the profiles in B.* ***(B)*** *Terrace river-facing edge points (circles), and strath field locations (diamonds) projected to the Arkansas Valley line that is shown in (A, inset).*

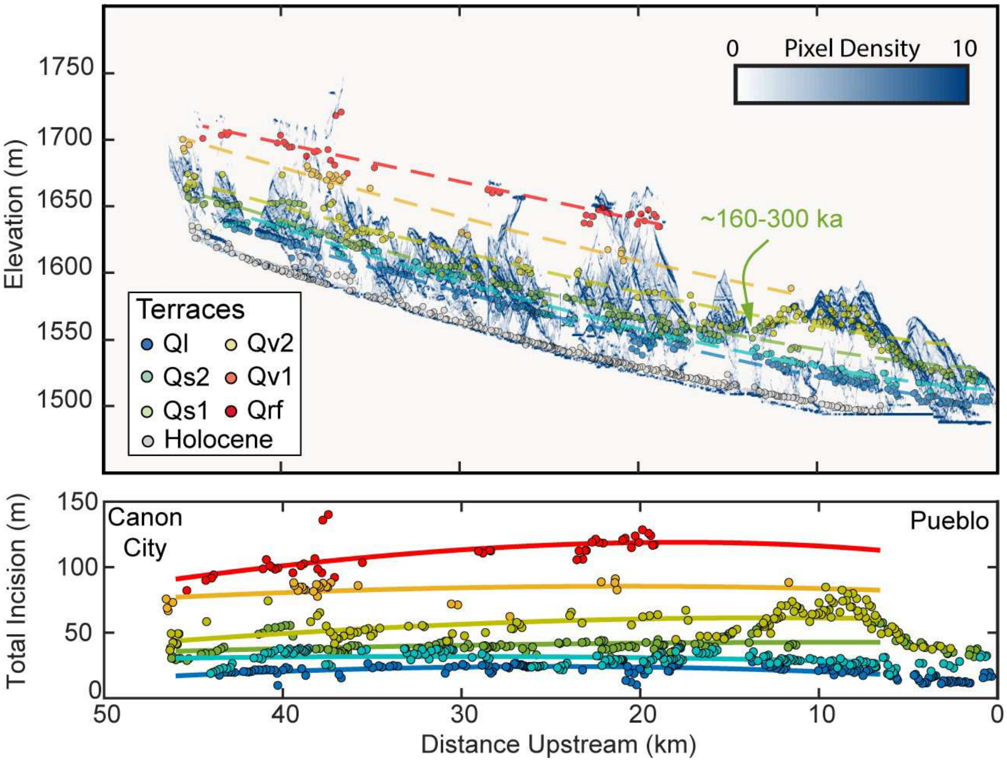

Figure 1.8 ***(A)*** *Two-dimensional hypsometry of the filtered LiDAR elevation data. Elevation pixels were projected to the trace of the Arkansas River valley (Figure 1.7A, inset), binned at 25 m increments of streamwise distance, and tailed at 1 m elevation increments. High pixel density values, which represent flat surfaces in the mapping area, correlate well with tread river-facing edge points (Figure 1.7A, inset). Also plotted are regressions of the pre-surfaces for each mapped terrace level based on the tread river-facing points. Note an antiformal deformation at ~5-15 km upstream Pueblo, CO, as seen from both the LiDAR hypsometry and the projected terrace points.* ***(B)*** *The estimated total incision for the mapped terraces as a function of upstream streamwise distance along the Arkansas River from Pueblo to Canon City. The total incision is calculated from the power-law pre-surface regressions in (A) and their elevation above the Arkansas River. The terraces show an increase in total incision magnitude as a function of downstream streamwise distance along the Arkansas River from Canon City to Pueblo.*

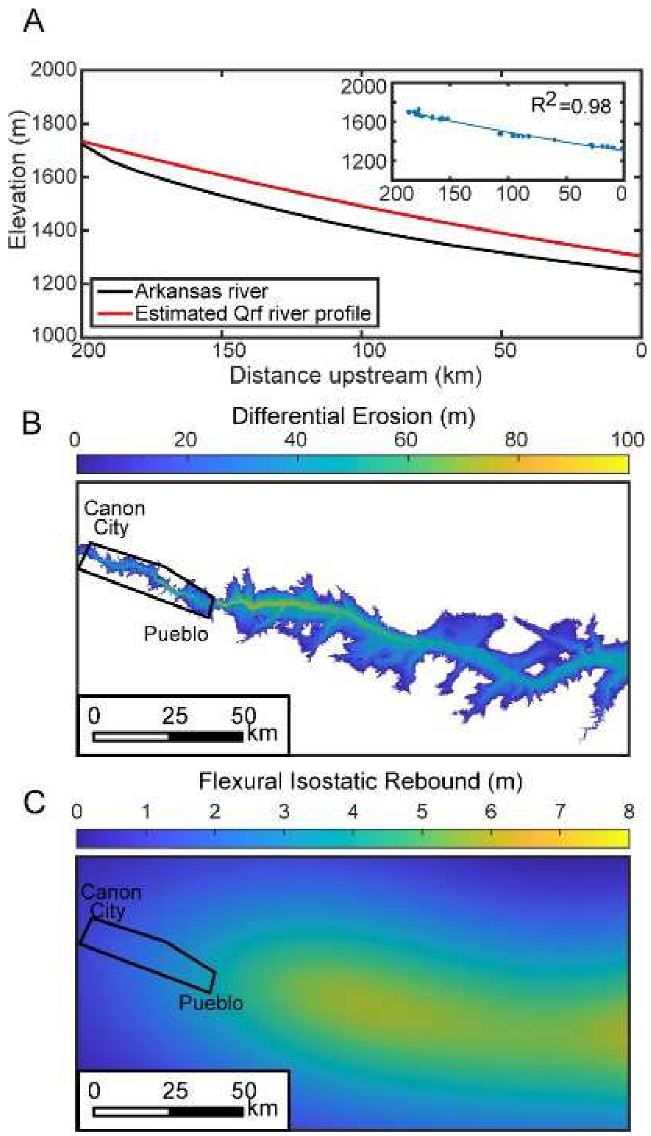

Figure 1.9 ***(A)*** *Estimated paleo Arkansas River profile at the time of the Rocky Flats (red line; ~1.3-2 Ma) and today (black line).* ***(Inset)*** *The power-law fit of the estimated paleo Arkansas River profile through river-face edge points of the mapped Rocky Flats in our study area and previously mapped treads downstream of the study area (Figure 1.1; Scott, 1972, 1977; Sharps, 1976).* ***(B)*** *Differential erosion between the extrapolated Rocky Flats surface and the modern topography across the Arkansas River valley in the High Plains.* ***(C)*** *Estimated flexural isostatic rebound under* $T_e = 10\ km$; $\rho_m = 3300\ kg/m^3$;$\rho_c = 2500\ kg/m^3$; $E = 10^{11}\ Pa$; $v = 0.25$ *(for results under lower and higher* T_e*, see Appendix A; Hansen et al., 2013; Lazear et al., 2013). The maximum flexural response, at ~50 km southeast of our study area, is ~4-10 m. Black polygons in (B) and (C) mark the extent of the terrace mapping area in Figure 7A.*

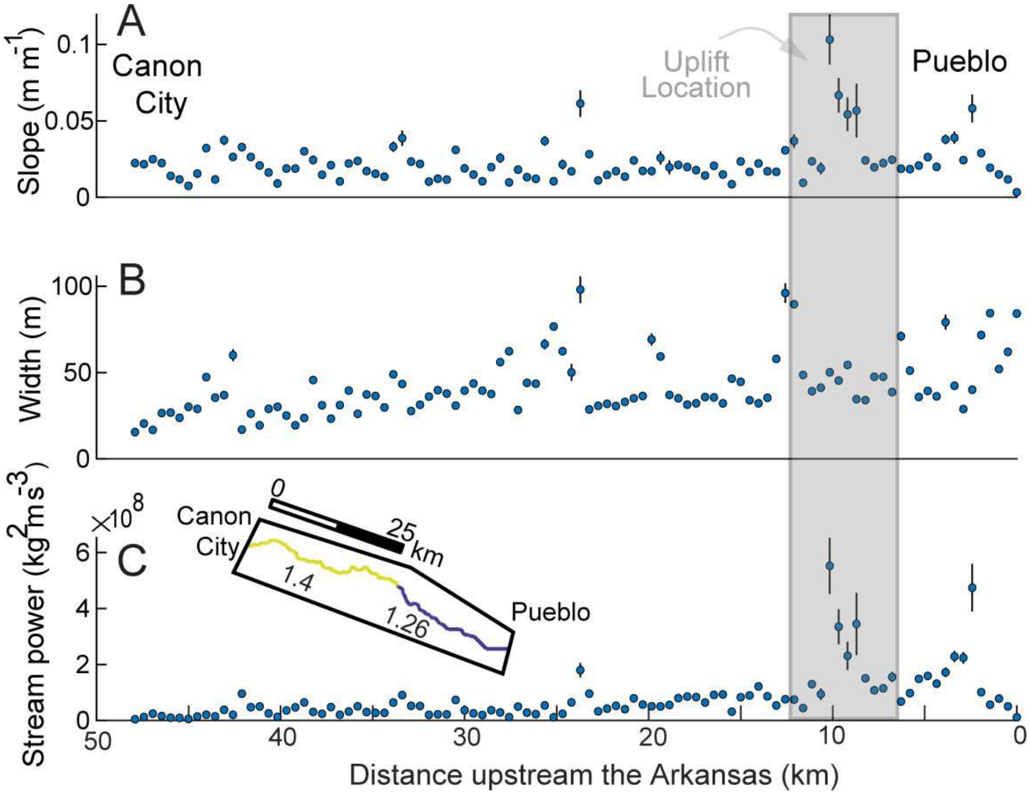

*Figure 1.10 The Arkansas River active channel slope **(A)**, width **(B)**, and sinuosity and unit stream power **(C)** from Canon City downstream to Pueblo. At ~5-15 km upstream from Pueblo, where the terraces record a local uplifted and deformed structure (Figure 1.8; gray transparent polygon), the active channel shows a local increase in slope up to 0.1, high unit stream power up to 6 kg m^2 s^{-3}, and low sinuosity of 1.26.*

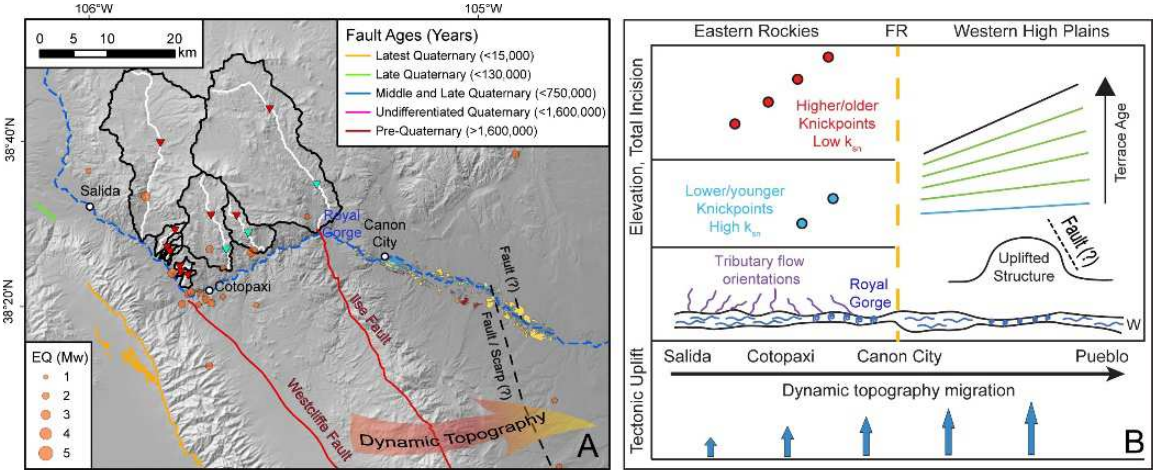

Figure 1.11 ***(A)*** *Knickpoint and terrace locations in the context of mapped faults and recorded microseismicity (USGS Fault and Earthquake digital archives). Newly proposed blind faults in the western High Plains (dashed black lines) are marked according to topographic and field observations and recorded deformation patterns in Pleistocene terraces (Figure 1.8). The direction of migrating dynamic topography following the geodynamic model by Moucha et al. (2008, 2009) is marked as well (orange arrow). Knickpoint and terrace colors and legends are as in Figures 4 and 7.* ***(B)*** *Geodynamic interpretation for the recent landscape unsteadiness in the southern Colorado Front Range. In the eastern Rockies, the knickpoint elevation trend (red and cyan points) and tributary trunk flow orientations (purple lines) show a sharp transition at the Cotopaxi region, where recent concentrated seismic activity is observed. Between Cotopaxi downstream to Canon City, knickpoint elevations and incision magnitudes at basin outlets increase eastwards towards the Front Range mountain front. For the same section,* k_{sn} *increases along tributary trunks from upper reaches to lower reaches. In the western High Plains, the fluvial terraces show increased incision moving downstream (eastwards) along the Arkansas River from Canon City to Pueblo. The terraces also record an uplifted deformed structure with potential recent faulting on it. This zone spatially correlates an area of increased narrowing, steepening, and high stream power of the Arkansas River. Collectively, the deformation patterns in the eastern Rockies and western High Plains are consistent with a geodynamic model of an eastward migrating dynamic topography that swept the area during the late Cenozoic (Moucha et al., 2008, 2009), as shown in (A).*

Table 1.1 Summary and comparison of fluvial terraces mapped in our study area with ages and descriptions of studies that mapped these terraces in northern sections of the Front Range.

Terrace Name	Area	Elevation (m)	Age	Dating Technique	Thickness (m)	Description
Louviers						
Scott et al. 1960	Louviers,CO	18.2m above stream and 12.19m below Slocum	Early Wisconsin (15-35 ka)	fossil mammals and mollusks	N/A	Reddish brown pebbly facies along the major streams and a yellowish-brown silty facies along the minor streams
Madole, 1991	Plum Creek	12-18m above plum creek, <10m in tributaries that confluence with South Platte River	86 ± 6 ka to 129 ± 10 ka (<Bull Lake Till -MIS 6 ~130-200 ka)	U-series on bones near Denver	1-3m	1. large streams: coarse facies, cobble and pebble gravel overlain by sand and minor silt; 2. small streams: fine grained facies - thin basal pebbel gravel overlain by thick sand and silt.
Lindsey et al. 2005	Entire South Platte Basin	21-24m above the South Platte; 15m above ralston & clear creek	130-200 ka (Bull Lake)	previous studies	10m, Boulder; 30m, Greely	Gravels with lenses of pebbly sand
Dahnforth et al., 2012	Boulder creek	N/A	130 ka	previous studies	N/A	N/A
This Study	Canon City to Pueblo,CO	15-25m above the Arkansas River	N/A	N/A	3-4m	Fine silt/loess size materials of ~0.6-1m over 0.6-1.5m of cobbles (10-50cm) imbricated to the south. Top loess is covered by organic material (charcoal/patina?)
Slocum						
Scott et al. 1960	Slocum Ranch, CO	30.5m above stream and 45.7m below Verdos	Illinoian or Sangamon	mollusks	N/A	Moderate reddish-brown, well-stratified, clayey coarse sand with lenticular beds of pebbles and silt
Madole, 1991	South Platte and Arkansas	30m above South Platte and Arkansas; 6m above tributaries of the South Platte; 6-12m above Louviers, 40-65 below Verdos.	160 ± 60 ka to 190 ± 50 ka (<Bull Lake Till - MIS 6 ~130-200 ka)	U-series,bison horn near Arkansas River	3-27m	Pediment or terrace deposit of clast-supported gravel, deeply oxidized, strongly developed paleosol (Bt/Btk/K)
Lindsey et al. 2005	Entire South Platte Basin	15m above the Poudre near Fort Collins; 30m above ralston creek	240 ka	previous studies	0.3m, ralston	Abundant vein quartz+quartzite, poorly to modertae rounded gravels
Riihimaki et al. 2006	Ralston Creek	25m above ralston creek	258 ± 27 ka to 296 ± 32 ka (no burial)/600-700 ka (0.5m burial)	TCN exposure (10Be/26Al)	1-5m	Gravel capped
Dahnforth et al., 2012	Boulder region	30m	190 ± 50 ka ;258 ± 27 ka to 296 ± 32 ka	previous studies	N/A	N/A
This Study	Canon City to Pueblo, CO	30-45m above the Arkansas River	N/A	N/A	2-6m (Qs2) 3-10m (Qs1)	Mostly rounded cobbles and pebbles of granodiorite (Qs2) transitioning to angular cobbles and boulders in partly oxidized matrix in upper part (Qs1)
Verdos						
Scott et al. 1960	Verdos Ranch, CO	45.7m above slocum and 30.5m below Rocky Flats	Kansan or Yarmouth	mollusks	4.9-10.6m	Brown, well stratified coarse sand with some boulders and a volcanic ash bed overlying Mesosoic bedrock
Madole, 1991	Denver area	70 ± 5m above present streams	620 ka	Lava Creek B volcanic ash	3-12m	Deeply eroded, well developed paleosol, beds and lenses of Lava Creek B, similar to Rocky Flats lithology and thickness (coarse, clast supported gravel)
Lindsey et al. 2005	Ralston Creek	75m above past piney creek alluvium	640 ka	previous studies	3-6m	52-69% quartzite
Riihimaki et al. 2006	Ralston Creek	45m above ralston creek	273 ± 29, 347 ± 38, 391 ± 43 ka	TCN exposure (10Be/26Al)	1-5m	Gravel capped
Dahnforth et al., 2012	Pioneer, Ralston Creek	65m above ralston creek	175 ± 27 ka	clast burial (10Be)	5-10m	Sand lens of 1-3m depth separating coarser units that are poorly sorted no imbrication. Coarse fraction are igneous and metamorphic with grain sizes ranging from a few to ~30 cm.
This Study	Canon City to Pueblo, CO	55-85m above the Arkansas River	N/A	N/A	1-5m	Sub-angular deposit, 20mm-400mm, decreasing upwards, boulders are granodiorite and pegmatite, rounded schist cobbles ~20-30mm, imbrication, reddish, oxidized paleosol.
Rocky Flats						
Scott et al. 1960	Great Western Inorganics, CO	30.5m above Verdos	Nebraskan or Aftonian	stratigraphic relation to Verdos	3-12.2m	Reddish-brown, poorly sorted, stony coarse sand uncomformatbly overlying on Mesosoic bedrock
Madole, 1991	Denver area	100 ± 10m above present streams and 30m above Verdos	early Pleistocene	stratigraphic relation to Verdos	3-12m	Well developed paleosol (Bt/Btk/K), coarse, clast supported gravel, oxidized and hues as red 5YR in upper few meters.
Lindsey et al. 2005	Rocky Flats (Boulder)	108.8m above Ralston Creek	750 ka	previous studies	1-30m	Coarse, poorly sorted, and weakly stratified gravel, 50-90% quartzite, some volcanics.
Riihimaki et al. 2006	Coal Creek, Denver Basin	100m above the South Platte	380 ± 41, 469 ± 52, 546 ± 62, 780 ± 94 ka	TCN exposure (10Be/26Al)	1-5m	Clast-supported, poorly sorted, clasts within alluvium 1-20cm and boulders on surface ~75cm, weathered and oxidized, strongly developed soils
Dahnforth et al., 2012	Table Mountain, Boulder	85m above Lefthand creek	95 ± 3.8 ka	Meteoric and clast burial (10Be)	5-10m	Unsorted, uniform gravels with a sediment matrix of clay, silt and sands. Coarse fraction is sandstones, igneous and metamorphic ranging from 1-30 cm, no obvious soil horizons.
This Study	Canon City to Pueblo, CO	95-110m above the Arkansas River	N/A	N/A	3-5m	Strongly weathered, calcified, highly cemented, oxidized "orange" matrix, cobbles 20-300mm, varied rounded igenous/metamorphic cobbles, strong alteration, developed rinds.

Table 1.2 Knickpoint locations, χ, and elevations, as shown in Figures 1.5A,B.

Basin ID*	KP Set	Location		χ	Absolute Elevation (m)	Basin Elevation (m)	Channel Distance (km)	
		Lat (°N)	Long (°W)				From Outlet	From Headwaters
6	I	38.66	105.81	11.48	2696	631	25.94	25.52
12	I	38.46	105.79	7.92	2315	284	3.26	5.43
14	I	38.45	105.79	7.02	2275	202	2.08	2.91
17	I	38.42	105.76	5.05	2299	280	2.17	4.02
19	I	38.41	105.76	7.27	2322	321	1.99	2.60
21	I	38.40	105.74	9.55	2401	395	3.36	2.35
28	II	38.45	105.64	4.12	2271	291	5.55	22.33
28	I	38.52	105.68	13.17	2644	664	15.94	11.94
32	II	38.48	105.59	7.58	2430	528	7.40	13.16
32	I	38.52	105.62	15.83	2679	777	13.20	7.35
36	II	38.58	105.41	6.09	2188	409	13.78	42.44
36	I	38.73	105.53	18.42	2562	783	36.60	19.62

Table 1.3 k_{sn} for different reaches/segments along tributary trunks, as shown in Figure 1.5C.

Basin ID*	Segment†	k_{sn}		R^2	χ		Elevation (m)		Basin Outlet Location		k_{sn} ratio
		Mean	STD§		min	max	min	max	Lat (°N)	Long (°W)	
6	KP I lower	59.79	0.47	0.997	0.17	10.60	2076	2677	38.47	105.86	6.00
	KP I upper	9.97	0.18	0.969	11.74	42.10	2696	2923	38.47	105.86	
12	KP I lower	33.01	2.02	0.977	0.21	7.60	2036	2293	38.43	105.81	1.22
	KP I upper	27.00	0.52	0.997	8.58	17.81	2331	2568	38.43	105.81	
14	KP I lower	30.42	1.79	0.998	4.39	6.70	2175	2255	38.43	105.80	1.43
	KP I upper	21.28	0.77	0.999	7.49	11.01	2282	2360	38.43	105.80	
17	KP I lower	99.36	5.27	0.996	3.19	4.83	2149	2291	38.41	105.78	3.04
	KP I upper	32.68	2.55	0.973	5.28	12.94	2312	2549	38.41	105.78	
19	KP I lower	46.58	1.47	0.999	2.84	7.27	2060	2312	38.39	105.77	2.59
	KP I upper	17.99	1.93	0.995	7.66	9.99	2328	2374	38.39	105.77	
21	KP I lower	77.69	3.07	0.999	8.23	9.55	2312	2400	38.38	105.76	4.08
	KP I upper	19.06	2.25	0.988	10.05	13.52	2419	2502	38.38	105.76	
28	KP II lower	75.89	6.67	0.924	0.26	3.49	1993	2253	38.41	105.64	1.53
	KP I lower	49.57	0.75	0.994	4.12	12.37	2272	2629	38.41	105.64	
	KP I upper	20.12	0.40	0.993	13.43	21.95	2649	2805	38.41	105.64	2.46
32	KP II lower	70.33	2.66	0.977	0.19	7.01	1912	2405	38.45	105.54	1.86
	KP I lower	37.79	0.86	0.991	8.03	14.93	2450	2663	38.45	105.54	
	KP I upper	13.83	0.18	0.998	16.43	25.84	2689	2815	38.45	105.54	2.73
36	KP II lower	65.03	1.47	0.984	0.21	5.29	1797	2131	38.50	105.40	2.19
	KP I lower	29.74	0.28	0.996	5.78	17.61	2185	2544	38.50	105.40	
	KP I upper	24.63	0.38	0.994	18.61	28.98	2568	2832	38.50	105.40	1.21

Chapter 2: Tectonic and geodynamic control on rejuvenation in the Colorado Rocky Mountains[2]

2.1 Introduction

Post-orogenic landscapes globally exhibit evidence of transient landscape evolution in the form of spatially and temporally variable erosion, incision, and exhumation rates and sediment flux, as well as ample evidence for disequilibrated river profiles and drainage networks. However, the mechanisms driving transient landscape evolution in post-orogenic settings remain unclear. In the last few decades, different drivers have been invoked to explain this enigma, namely active tectonics, geodynamics, climate change, isostasy, drainage reorganization, and lithological variability (Pazzaglia and Gardner, 1994; Fischer, 2002; Prince et al., 2011; Gallen et al., 2013; Miller et al., 2013; Tucker and van der Beek, 2013; Willett et al., 2014; Jones et al., 2015; Giachetta et al., 2015; Molnar et al., 2015; Beeson et al., 2017; Blackburn et al., 2018; Gallen, 2018; Peifer et al., 2020; Tao et al., 2020). Yet, up to date, there has been no consensus on this matter.

A prime example of this conundrum is the Colorado Rocky Mountains in the middle of the North American plate (herein CRM; Figure 2.1A). The region's high relief, steep topography and fluctuations in sediment production since the end of the Laramide Orogeny at ~40 Ma (Raynolds, 2002; Eaton, 2008; Tucker and van der Beek, 2013) all imply landscape unsteadiness during the late Cenozoic. This is best demonstrated by studies that explored deformation in sedimentary units of the Ogallala Group (largely fluvial sandstones and conglomerates) that blanketed the ancient foreland basin of the CRM in the High Plains physiographic province (herein HP; Figure 2.1B) during the mid to late Miocene. Studies noted that the long-wavelength slope of the Ogallala surface shows a higher tilt away from the CRM hinterland relative to other active foreland basins globally (Eaton, 2008; Duller et al., 2012). Importantly, empirical studies showed that the Ogallala depositional surface and its underlying sedimentary units in the HP have been rapidly incised in the last ~5 Ma (Leonard, 2002; McMillan et al., 2002; McMillan and Heller, 2006; Duller et al., 2012; Heller and Liu, 2016). Collectively, these lines of evidence led geologists and geomorphologists to conclude that the HP, and likely the entire CRM, have been experiencing a large-scale shift in landscape boundary conditions and topographic rejuvenation in the last ~5 Ma.

---

[2] This chapter is under work as a manuscript for GSA Today

Yet, while studies generally agree that topographic rejuvenation occurred in the CRM during the late Cenozoic, an ongoing controversy surrounds the primary driving mechanism. One hypothesis proposes that active tectonics associated with the Rio Grande Rift and/or long-wavelength regional geodynamic processes uplifted and tilted the CRM in the last ~5 Ma (Figure 2.1A; Mitrovica et al., 1989; Leonard, 2002; McMillan et al., 2002; McMillan and Heller, 2006; Moucha et al., 2008; Karlstrom et al., 2012; Duller et al., 2012; Rosenberg et al., 2014; Abbey and Niemi, 2018). An alternative hypothesis claims that climate-induced changes in discharge and sediment flux, caused by rapidly fluctuating climate during the Plio-Pleistocene, increased erosional efficacy across the entire CRM, causing rivers in the HP to incise rapidly and reduce their gradients (Figure 2.1A; Small and Anderson, 1998; Riihimaki et al., 2006, 2007; Pelletier, 2009; Wobus et al., 2010; Dühnforth et al., 2012; Tucker and van der Beek, 2013; Langston et al., 2015). These two contrasting hypotheses were largely drawn from geomorphological and sedimentological studies in the HP.

For instance, studies that favor a tectonic or geodynamic driver based interpretations on reconstructions of the depositional Ogallala surface, which exhibits an antiformal deformation with a peak in the southern HP that decays to the north and east (Leonard, 2002; McMillan and Heller, 2006). These studies showed that the deformation in the HP could not be explained solely by the small magnitude of isostatic rebound due to differential erosion below the Ogallala surface, implying a significant tectonic or geodynamic driver (e.g., Leonard, 2002). This interpretation is supported by a paleo-hydrology study that showed that gravels in channels within the Ogallala Group were transported and deposited along paleo-channel slopes far less than the observed modern gradient of the Ogallala depositional surface (McMillan and Heller, 2006). In contrast, studies that favor a climatic driver, based interpretations on paleo-hydrology and numerical modeling analyses on reconstructed Pliocene paleo-channels of rivers in the HP. These studies showed that the steep slopes and high gradients of reconstructed paleo-rivers existed since the Pliocene. Based on this evidence, it was argued that climate-induced aggradation at the time of global warming during the mid-Pliocene, followed by an incisional period during global cooling in the late Pliocene and Pleistocene, drove most of the rapid incision in the HP during the late Cenozoic. Within this interpretation, the rapidly incised rivers in the HP are predicted to relax their gradients while incising through the Ogallala Group in response to changes in discharge and sediment supply (Wobus et al., 2010).

Here, we contribute to this discussion by expanding the analysis of transient geomorphic and landscape signatures from the HP upstream to the Colorado Rockies province (herein CP; Figure 2.1A). We do that because we hypothesize that the incision of bedrock rivers into the harder crystalline basement of the CR (Figure 2.1B) might still record landscape response to changes in boundary conditions propagating upstream from the HP channel network. We focus our effort on river profile analysis in bedrock channels in the CR and combine it with new and existing basin average erosion rates from cosmogenic ^{10}Be and local channel incision rates from luminescence dating on fluvial terraces. We compare spatiotemporal patterns in these bedrock river profiles, landscape erosion rates, and channel incision rates across the CR with predicted geomorphic patterns from the two end-member hypotheses to determine which best explain recent topographic rejuvenation in the CRM.

2.2 Background

2.2.1 Geological and geomorphological history of the CRM

The CRM was first uplifted in the Pennsylvanian as part of a series of intra-tectonic basement uplifts during the Ancestral Rockies orogenic events (Kluth and Coney, 1981). However, most of the modern-day topography of the CRM is traditionally related to two following orogenic events during the Cenozoic. In the early Cenozoic, the CRM was uplifted, warped and folded during the Laramide Orogeny at ~40 - 80 Ma (Dickinson and Snyder, 1978; Bird, 1998; DeCelles, 2004; Liu et al., 2010). During the Eocene and Oligocene, the CRM experienced a protracted period of declining relief that is recorded by the formation and preservation of the Rocky Mountain erosional surface (Scott and Taylor, 1975; Steven, 1975; Epis et al., 1976; Kluth and Nelson, 1988; Abbey et al., 2018). This period of tectonic quiescence was disrupted by a second orogenic event where tectonic extension and normal faulting associated with the Rio Grande Rift system dismembered, structurally inverted, and uplifted parts of the CRM (particularly in its southern part) (Epis et al., 1976; Heller et al., 2003; Liu et al., 2010). Since the late Miocene and during the Quaternary, the CRM topography was presumably rejuvenated to produce most of its modern-day high topographic relief (Leonard, 2002; McMillan and Heller, 2006).

This geological history of the CRM resulted in the formation of two major physiographic provinces: the rugged, high elevation CR and the subdued, low elevation HP, which are underlain by crystalline and sedimentary basements, respectively (Figure 2.1B; Tuyl and Lovering, 1935; Chapin and Kelley, 1997; Keller and Morgan, 2016). These sharp lithologic and topographic contrasts between the CR and HP results in a differential landscape response during the late Cenozoic. The CR drainage network is characterized by bedrock channels that incise into the Proterozoic crystalline basement to form deep gullies and canyons, while the HP drainage network is characterized by mixed bedrock-alluvial channels that incise into gently deformed, east tilted late Mesozoic to Cenozoic sedimentary units, including the Ogallala Formation (Scott and Lindvall, 1970; Heede, 1970; Madole, 1991; Lindsey et al., 2005).

2.2.2 Geomorphic predictions of hypotheses for topographic rejuvenation in the CRM

Each of the prevailing end-member hypotheses described above makes different predictions regarding the style of transient landscape evolution recorded in the CP drainage network. For instance, hypotheses favoring a tectonic or geodynamic driver predict a sustained increase in rock uplift rate in the last ~5 Ma. This sustained increase in rock uplift rate will result in a sustained increase in base level fall rate and a signal propagating from the HP upstream to the CR drainage network in the form of convex upward (herein “normal”) slope-break knickpoints with higher channel steepness below them (Figure 2.2; e.g., Kirby and Whipple, 2012). A sustained increase in base level fall rate in the CR in the last ~5 Ma also predicts higher incision rates downstream of the propagating normal knickpoints, and based on the work by Leonard (2002), a regional increase in the magnitude of deformation from the north CRM to the south CRM (Figure 2.1A; Figure 2.2).

The hypotheses suggesting a climate driver and a transient adjustment of river gradients due to an increase in erosional efficiency predict that the incision rates along rivers in the HP will slow through time and approach the isostatically-imposed rock uplift rate as topography adjusts its shape to the new climate conditions (Figure 2.2; Wobus et al., 2010). This requires the CR landscape to re-equilibrate via river relaxation, which under fluvial bedrock incision and detachment-limited conditions, will result in convex downward (herein “inverted”) knickpoints with higher channel steepness above knickpoints, and relatively uniform signals in landscape erosion rates and channel incision rates across the entire CR (Figure 2.2). Thus, each of the two end-member hypotheses makes different, testable predictions regarding the pace and style of landscape adjustment that we intend to test here through geomorphic and landscape analyses of the CP drainage network.

2.3 Methods

2.3.1 Measuring erosion and incision rates in the CRM

The main surface mechanisms that dictate landscape erosion rates in 10^3-10^6 yr timescales are hillslope erosion, channel incision, and sediment production (Granger and Schaller, 2014). An effective method to quantify these millennial-to-centennial-scale erosion rates is by measuring the concentration of cosmogenic nuclides in earth materials (e.g., ^{10}Be in quartz) (Bierman and Steig, 1996; Granger and Muzikar, 2001; Portenga and Bierman, 2011; Granger and Schaller, 2014). These cosmogenic nuclide concentrations reflect the amount of time a rock parcel resides within the upper ~1 m of the earth surface that is inversely proportional to the near surface erosion rate (Bierman and Steig, 1996; Granger and Schaller, 2014). In well-mixed fluvial sands at drainage outlets, cosmogenic nuclides concentrations have been shown to reflect erosion rates averaged over the entire drainage basin (Portenga and Bierman, 2011; Granger and Schaller, 2014). Here we build off this method to determine basin average erosion rates at basin outlets that confluence with the Poudre and Arkansas rivers in the northern and southern CRM, respectively, combined with existing measurements of basin average erosion rates west of Boulder, CO, to examine spatiotemporal changes of long-term hillslope erosion rates on a north-to-south transect across the CRM (Figure 2.1).

To complement these measurements with recent incision rates in the active drainage network of the CRM, we also produce new luminescence ages for fluvial terraces in the southern CRM along the Arkansas River from optically stimulated luminescence (OSL) on quartz grains and infrared stimulated luminescence (IRSL) on feldspar grains (Appendix B). This method works by illuminating trapped electrons in radioactive elements in buried fine sand material and quantifying the magnitude of this illumination, which is proportional to the burial time since the terrace abandonment by the river (assuming the sample was not exposed previously to sunlight) (Nelson et al., 2015). We combine the new terrace ages in the southern CRM with existing geochronological estimates of terrace ages from luminescence dating and cosmogenic burial data near Boulder, CO (Table B3; Schildgen et al., 2002; Dühnforth et al., 2012) as well as inferred ages of some terraces based on correlation with stream glacial deposits along the Poudre River. We calculate local channel incision rates based on the new and existing terrace ages and their strath heights above their modern rivers (Dühnforth et al., 2012; Pazzaglia, 2013).

Collectively, we use the new and existing basin average erosion rates and channel incision rates across the CRM to image the spatial patterns of landscape denudation and interpret them in the context of the predictions of the two hypotheses.

2.3.2 River profile analysis

Fluvial knickpoints are a common geomorphic marker used to explore landscape response to changes in geological, climatic, and tectonic boundary conditions (Crosby and Whipple, 2004; Wobus et al., 2006; Berlin and Anderson, 2007; Kirby and Whipple, 2012; Gallen et al., 2013; Gallen and Wegmann, 2017; Marder et al.). They are classified as vertical-step and slope-break knickpoints, based on their morphology, where vertical step knickpoints are identified as sharp (step-like) discrete drops in river profile elevation, and slope-break knickpoints are defined by a sustained change in channel steepness above and below these knickpoints (Crosby and Whipple, 2004; Wobus et al., 2006; Haviv et al., 2010; Kirby and Whipple, 2012). Both of these knickpoint types can be static and related to changes in bedrock erodibility or discrete spatial changes in rock uplift (e.g., faults), or mobile and related to changes in base level lowering rate caused by a temporal change in rock uplift rate or a sudden basin level drop (Crosby and Whipple, 2004; Wobus et al., 2006; Kirby and Whipple, 2012). In the case of the prevailing hypotheses for topographic rejuvenation in the CRM, both predict mobile slope-break knickpoints. The tectonic hypothesis predicts normal knickpoints with lower and higher channel steepness above and below them, respectively, while the climate hypothesis predicts inverted slope-break knickpoints with a reversed channel steepness pattern (Figure 2.2).

Here we use river profile analysis to identify these knickpoint morphologies and channel steepness. We calculate their normalized channel steepness index, k_{sn}, which is a common metric to analyze river profiles based on a stream power model framework (Kirby and Whipple, 2012). To do so, we extract the local channel slope, S, and upstream contributing drainage area, A, from a digital elevation model (DEM), which are empirically related to k_{sn} (Flint, 1974):

$$k_{sn} = SA^{-\theta_{ref}} \tag{1,}$$

where θ^{ref} is the reference concavity index, ~0.3-0.7 globally (Kirby and Whipple, 2012; Harel et al., 2016). k_{sn} can be calculated from the y-intercept in $\log(S)$ versus $\log(A)$ in equation 1. Yet, this calculation introduces unwanted noise into the analysis. Thus, it is often preferred to calculate k_{sn} using a new transformed length parameter, χ, to the distance along the river profile, x (Figure 2.2; Appendix B; Perron et al., 2013):

$$\chi = \int_{x_b}^{x} A(x')^{-\theta^{ref}} dx' \tag{2}$$

$$z(x) = z(x_b) + k_{sn}\chi \tag{3,}$$

where z is elevation along the profile and x_b is the distance at the drainage outlet. Equation 3 shows that k_{sn} can be calculated for different segments along a river profile by linear regressions through $\chi - z$ plots (known as χ-plots; Figure 2.2). In the case of an increase in tectonic uplift or base level fall rate (i.e., the tectonic hypothesis), a series of normal knickpoints will propagate upstream from the basin outlet to separate a lower reach with higher k_{sn} from a higher reach with lower k_{sn} (Figure 2.2). On a regional scale, rivers that will experience higher tectonic uplift rates will have higher k_{sn} in reaches below normal knickpoints than rivers that experience lower uplift rates (Snyder et al., 2000; Kirby and Whipple, 2012). In the case of an increase in discharge or stream power through a drainage network (i.e., the climate hypothesis), inverted knickpoints will separate higher reaches with higher k_{sn} from lower reaches with lower k_{sn} (Figure 2.2). On a regional scale, these rivers will show similar k_{sn} patterns and magnitudes above and below these inverted knickpoints. Thus, by exploring the geometry and spatiotemporal patterns of river knickpoints across the CRM, we can test and differentiate between the tectonic and climate hypothesis predictions for rejuvenation in the CRM during the late Cenozoic.

2.3.3 Sampling and analysis in the CR and HP drainage networks

We collected twelve basin average erosion rate samples from fluvial sands at basin outlets that confluence with the Cache la Poudre and Arkansas rivers (Figure 2.1; Table B1). We processed these samples using standard techniques of extracting ^{10}Be from purified quartz grains (Appendix B; Table B2; Bierman and Steig, 1996; Granger and Schaller, 2014). We combined these new results in the Poudre and Arkansas rivers with existing ^{10}Be concentrations measured at basins west of Boulder, CO (Figure 2.1; Table B1; Dethier et al., 2014). We calculated erosion rates for all these samples using the CRONUS algorithm (Appendix B; Balco et al., 2008) and filtered out data from small basins < 10 km^2 to avoid potential concentration biases introduced by poorly mixed landslide material (Yanites et al., 2009).

We processed seven samples of fine sand from different Quaternary fluvial terraces along the Arkansas River for OSL and IRSL to determine terrace ages (Figure 2.1; Appendix B; Table B3, Table B4). We compiled this data with the existing terrace ages near and west of Boulder, CO (Schildgen et al., 2002; Dühnforth et al., 2012) and calculated local incision rates based on these terrace elevations above their modern rivers (Figure 2.1; Table B3). In the north part of the CRM, where we did not have geochronology data, we use existing approximations of terrace ages for mapped alluvial deposits in the Cache la Poudre River (Abbott, 1976; Braddock, 1988). Based on the geochronology data in the Arkansas River and age approximation for terraces in the Poudre, we digitized Quaternary fluvial terraces (~100-200 ka) along the Poudre and Arkansas main stems to reconstruct their paleo-river profiles and assess spatial patterns of incision along their main stems during the Quaternary.

We delineated 24 basins that drain to the CR-HP boundary (Figure 2.1A) using a Shuttle Radar Topography Mission (SRTM) 1 arc-second (~30 m horizontal resolution) DEM. We conducted river profile analysis on each basin using TopoToolbox v2 (Schwanghart and Scherler, 2014) and ChiProfiler (Gallen and Wegmann, 2017) (Figure B1). We used a θ_{ref} of 0.45 based on a best-fit variance minimization method for the entire CR drainage network ('mnoptimvar' in TopoToolbox; e.g., Goren et al., 2014; Hergarten et al., 2016). We detected slope-break knickpoints in river profiles based on the criteria of at least 25% difference in k_{sn} in reaches above and below knickpoints in $\chi - z$ space (Figure 2.1, Figure 2.2,

Figure B1). We mapped knickpoints only in drainage networks that are up to ~40 km upstream from the CR-HP boundary to avoid areas that experience alluviation and glacial scouring closer to the Continental Divide (Figure 2.1A). For each knickpoint, we measured k_{sn} for reaches above and below the knickpoint location in χ plots (Equation 3; Figure B1).

2.4 Results

The ^{10}Be-derived basin average erosion rates across the CRM are roughly consistent at ~0.01-0.02 mm/yr for the northern and central CRM and slightly higher ~0.03-0.05 mm/yr in the southern CRM (Figure 2.1A, Figure 2.3A). The channel incision rates across the entire CRM are an order of magnitude higher than these erosion rates and range between ~0.1 to 0.8 mm/yr (Figure 2.1A, Figure 2.3A). These incision rates are consistent between crystalline and sedimentary units in the CR and HP (Figure 2.1B) and show a systematic increase with decreasing terrace age (Figure 2.3B). Reconstructed paleo-river profiles from the Pleistocene terraces along the Arkansas and Poudre rivers show low incision rates of ~0.05 mm/yr above normal knickpoints and high incision rates of ~0.2-0.3 mm/yr below them (Figure 2.4). River profile analysis of the 24 basins across the CRM reveals a series of normal knickpoints as in the Arkansas and Poudre rivers at ~40 km upstream from the CR-HP boundary with a narrow range of χ values of ~2-4 (Figure 2.5, Figure B1). When these knickpoints are projected on a north to south line across the CRM (A-A' in Figure 2.1A), k_{sn} in reaches below these knickpoints increases systematically from ~150 m$^{0.9}$ in the north to 300 m$^{0.9}$ in the south, while k_{sn} in reaches above these knickpoints is relatively constant at ~80-90 m$^{0.9}$ (Figure 2.6).

2.5 Discussion

The channel incision rates from Quaternary fluvial terraces (~12-300 ka) across the CR-HP transition zone and downstream of the normal knickpoints are an order of magnitude higher than basin average erosion rates in this region (Figure 2.1, Figure 2.3A). These high channel incision rates systematically increase with younger terraces to reflect a potential temporal increase in base level fall rate during the Quaternary (Figure 2.3B). However, caution should be made in interpreting the meaning of this signal due to the potential for a Sadler effect (Finnegan et al., 2014; Gallen et al., 2015). Recognizing this potential bias, we consider samples older than 50 ka as more reliable (Figure 2.3B). The reconstructed paleo-river profiles along the Arkansas and Poudre rivers exhibit variable incision rates below the knickpoints with an average rate of ~0.25 mm/yr (Figure 2.4). This average value is consistent with incision rates measured from river terraces > 50 ka across the CR-HP boundary zone (Figure 2.1A, Figure 2.3B;

Table B3; Dühnforth et al., 2012; Marder et al.) and ^{10}Be erosion rates in the High plains (Dethier et al., 2014). Above the normal knickpoints, however, channel incision rates are only a fraction of the incision rates below the knickpoints (Figure 2.4) and slightly higher than the basin average erosion rates across the CR (Figure 2.1A, Figure 2.3A). Based on this consistency, we interpret the incision rates above normal knickpoints and the basin average erosion rates across the CR as reflecting erosion of the upland, relict topography, and the incision rates below these knickpoints as reflecting the transient rejuvenated landscape (Figure 2.6).

All the mapped knickpoints in the eastern CR drainage network are normal knickpoints that consistently lie at a relative elevation of ~450 m and relative χ value of ~3 when calculated from the CR-HP boundary (Figure 2.5). Provided similar rates of rock uplift and uniform erodibility, these knickpoints reflect upstream migration at the same vertical rate in χ-transformed distance (Niemann et al., 2001; Perron et al., 2013). We, therefore, interpret the consistency in relative knickpoint elevation and χ to a common base level fall event that originated downstream of the CR-HP boundary. Further, combined with the erosion and incision spatiotemporal patterns across the CRM (Figure 2.3, Figure 2.4), our results indicate recent relief production propagating from the CR-HP boundary upstream, where the gentle fluvial topography above knickpoints is interpreted as reflecting slow (~0.03 mm/yr) pre-topographic rejuvenation base level fall rate, and the steeper fluvial topography below these knickpoints as reflecting recent and faster (ca. 0.25 mm/yr) incision rates (Figure 2.6).

The climate hypothesis predicts increased erodibility across the entire CRM during the Quaternary. If true, river profiles across the CRM are expected to reduce their gradient (i.e., k_{sn}) to generate a series of inverted knickpoints and transient enhanced incision rates that will decline back to the isostatically-imposed rock uplift rate over time (Figure 2.2; Wobus et al., 2010). Yet, our results contradict these predictions and instead show a sustained transient and steeper drainage network downstream of the normal knickpoints (Figure 2.6). These high channel incision rates of ~0.1-0.8 mm/yr across the CRM indicate a sustained increase in base level fall rate that is consistent with epeirogeny and dynamic topography (Leonard, 2002; McMillan and Heller, 2006; Eaton, 2008) rather than climate-related ephemeral relaxation (e.g., Wobus et al., 2010). Another climate-induced mechanism that is often suggested to explain the increase in base level fall rate is isostatic rebound. However, previous studies showed that the expected isostatic response to erosion since ~5 Ma would not exceed ~200 m (Leonard, 2002; McMillan and Heller, 2006; Willett et al., 2018). Thus, collectively, the observations and geomorphic patterns for topographic rejuvenation across the CRM in this study cannot be explained by predictions of the climate hypothesis.

Our results appear consistent with the tectonic/geodynamic hypothesis (Figure 2.2). The most consistent evidence for tectonic impact on landscape morphology in the CRM during the late Cenozoic are the repeated normal knickpoints and the systematic increase in k_{sn} in reaches below them as a function of distance from north to south along the CR-HP boundary (Figure 2.1A, Figure 2.5, Figure 2.6, Figure B1). This is consistent with the results and predicted patterns by Leonard (2002) and McMillan and Heller (2006) in their studies in the HP, and by predictions and observations from other empirical and numerical studies that invoked active tectonics and geodynamics in the CRM during the late Cenozoic (Moucha et al., 2009; Heller and Liu, 2016; Abbey and Niemi, 2018). Recognizing the long-wavelength of deformation of these knickpoints across the CRM from north to south (~350 km; Figure 2.1A, Figure 2.5, Figure 2.6) and the high magnitude of total incision near the CR-HP boundary (up to ~400 m; Figure 2.5), the CRM appear to record a significant geodynamic signal and tectonic-related rejuvenation during the late Cenozoic (Figure 2.2, Figure 2.5, Figure 2.6; McMillan and Heller, 2006; Moucha et al., 2009; Marder et al.), which is consistent with a geodynamic model of a migrating dynamic topography that swept the CRM in the last 10 Ma (Moucha et al., 2009).

2.6 Conclusions

New and existing data of long-term basin average erosion rates, short-term channel incision rates, and river profile analysis across the CRM indicate recent regional base level fall along the CR-HP boundary. The predominance of slope-break normal knickpoints, the lack of climate-related deformation patterns, and increase of k_{sn} from north to south, all support the tectonic-induced rejuvenation hypothesis for the CRM. The long wavelength of deformation and the high magnitude of incision rates suggest a significant role of dynamic topography that has impacted the CRM during the late Cenozoic. Previously suggested mechanisms for rejuvenation in the CRM, namely active tectonics by the Rio Grande Rift or increased erosional efficacy by global cooling, seem to be secondary to this geodynamic signal that has been superimposed on them. Future cross correlation of surficial mapping and terrace dating with regional numerical modeling and long-term erosion rates along a predicted geodynamic migration direction could bolster or refute this suggested geodynamic interpretation versus other tectonic and climatic mechanisms.

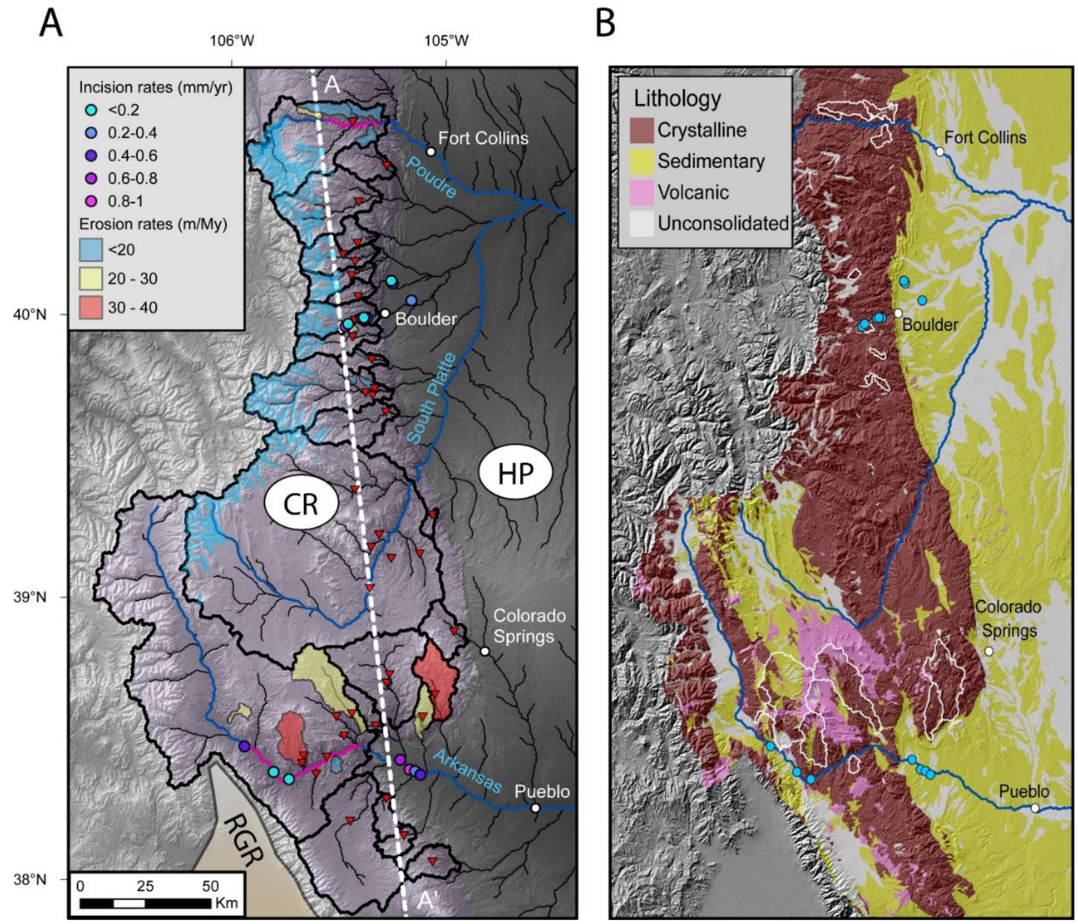

*Figure 2.1 **(A)** The Colorado Rocky Mountains (CRM) study area. Shown are new and existing (Schildgen et al., 2002; Dethier et al., 2014) erosion and incision rates data. Basins (black lines) and normal knickpoints (red inverted triangles), and terrace lines of the reconstructed paleo-river profiles in Figure 2.3 (pink lines) are noted. The north to south line (A-A') to where knickpoints are projected in Figure 2.4 and Figure 2.5 is marked. Extents of the Rio Grande Rift northern tip (RGR, orange polygon) and ice sheet cover during the Pleistocene (Madole et al., 1998; blue polygons) are marked for reference. **(B)** Main lithology across the CRM (Fick and Hijmans, 2017). Basins where erosion rates were calculated (white polygons) and terrace locations where incision rates were calculated (blue points) are marked for reference.*

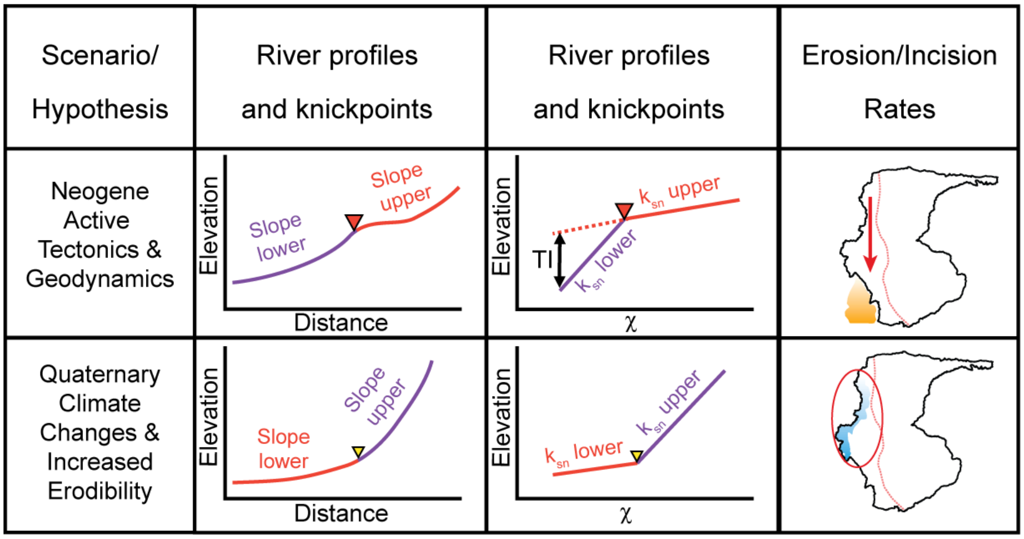

Figure 2.2 Predicted geomorphic patterns for the prevailing tectonic and climate hypotheses for recent rejuvenation in the CRM. In the case of active tectonics and geodynamics during the late Cenozoic, the expected geomorphic patterns include generation of slope break normal knickpoints (red inverted triangle) where the slope/k_{sn} in reaches below are higher than the slope/k_{sn} in reaches above the knickpoints. In χ-plots, extrapolation of the upper reach to the basin outlet can be used to estimate total incision (TI) since the knickpoint migration. Erosion and incision rates are expected to increase towards the tectonic loci during the late Cenozoic near the southwest CRM. In contrast, in the case of a climate-induced uniform increased erodibility across the CRM during the Quaternary, river profiles will show inverted knickpoints (yellow inverted triangle) with opposite slopes/k_{sn} patterns than in the case of normal knickpoints. Erosion and incision rates are expected to be uniform across the entire CRM.

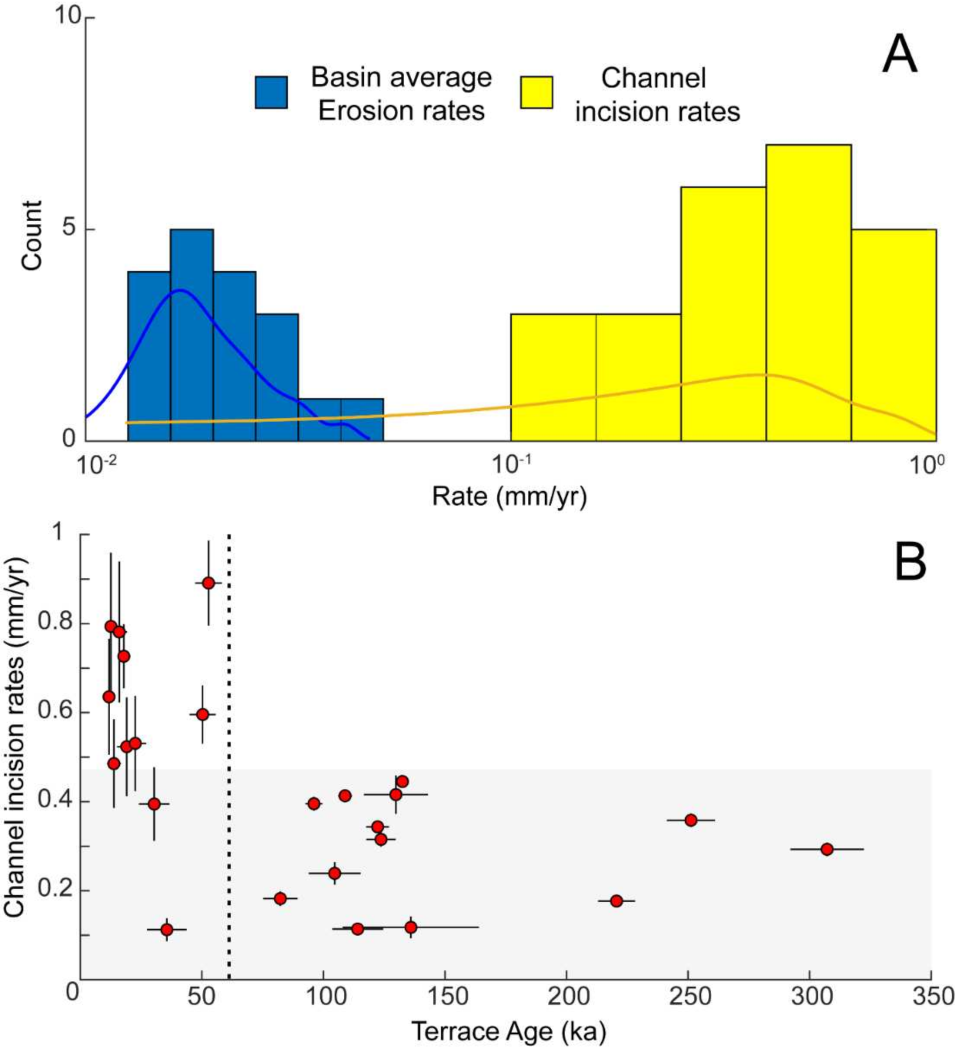

Figure 2.3 ***(A)*** *Histograms of the compiled data of basin average erosion rates and channel incision rates across the CRM.* ***(B)*** *Channel incision rates versus the terrace ages where rates were calculated. Note a systematic increase in incision rate with younger terraces < 50 ka that might reflect a real signal or a bias due to a Sadler effect (Finnegan et al., 2014; Gallen et al., 2015).*

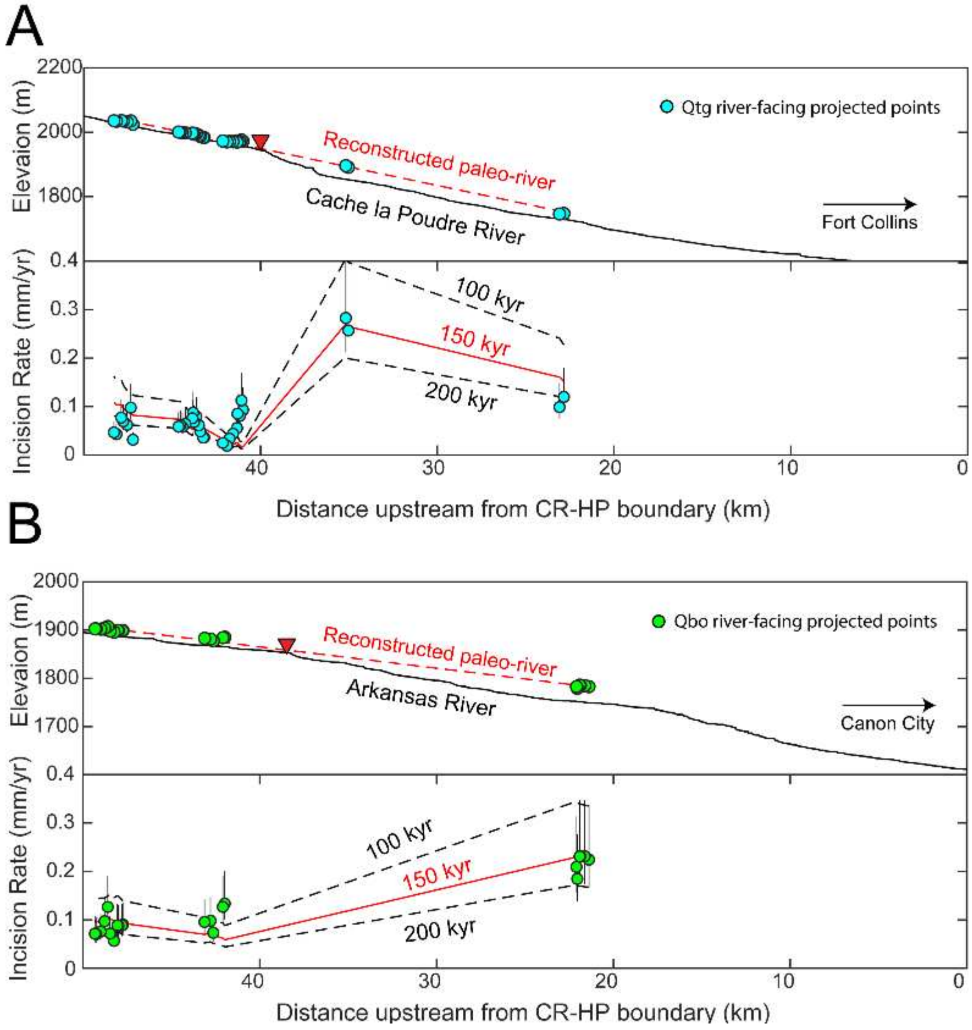

Figure 2.4 ***(A)*** *Reconstructed paleo-river profile and incision rates (red line) of the Cache la Poudre main stem (black line) based on digitized Quaternary fluvial terraces and estimated age of 150 ka (Qtg; blue points; Abbott, 1976; Braddock, 1988).* ***(B)*** *Same as (C) for the Arkansas river main stem (Qbo; green points; (Taylor, 1975; Taylor et al., 1975b). Black dashed lines show calculated incision rates in the case of younger or older ages for these terraces for 100 and 200 ka, respectively.*

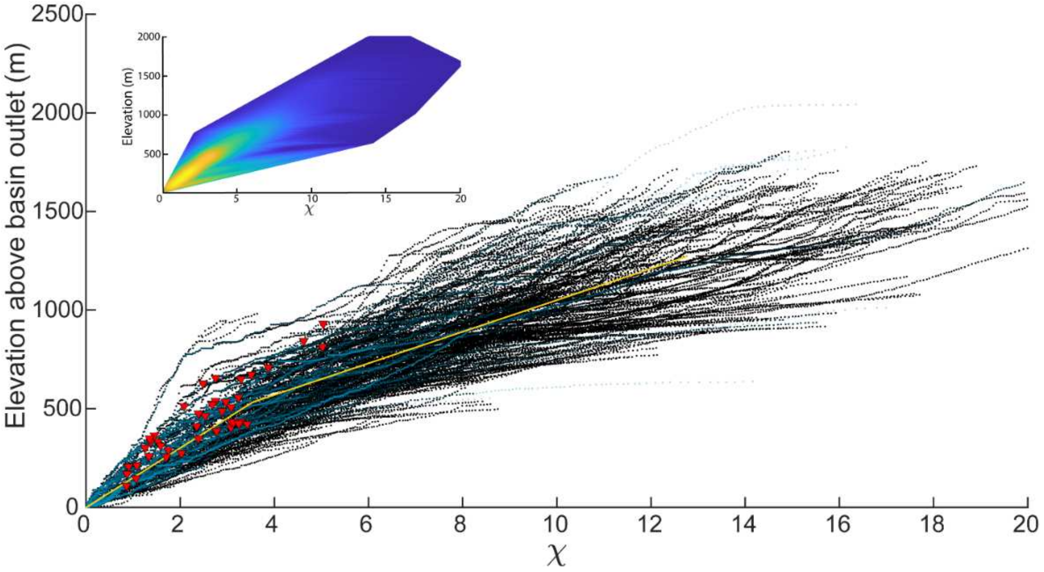

Figure 2.5 ***(Main)*** *River profiles (black) for all basins shown in Figure 1A in* χ*-plot. Blue lines are river profiles where slope-break normal knickpoints (red inverted triangles) were identified. Thick yellow line shows an estimated average slope above and below the normal knickpoints.* ***(Inset)*** *relative density of the data plotted in the main figure. Note high density at* χ*~2-4. For a full river profile analysis, see Figure B1.*

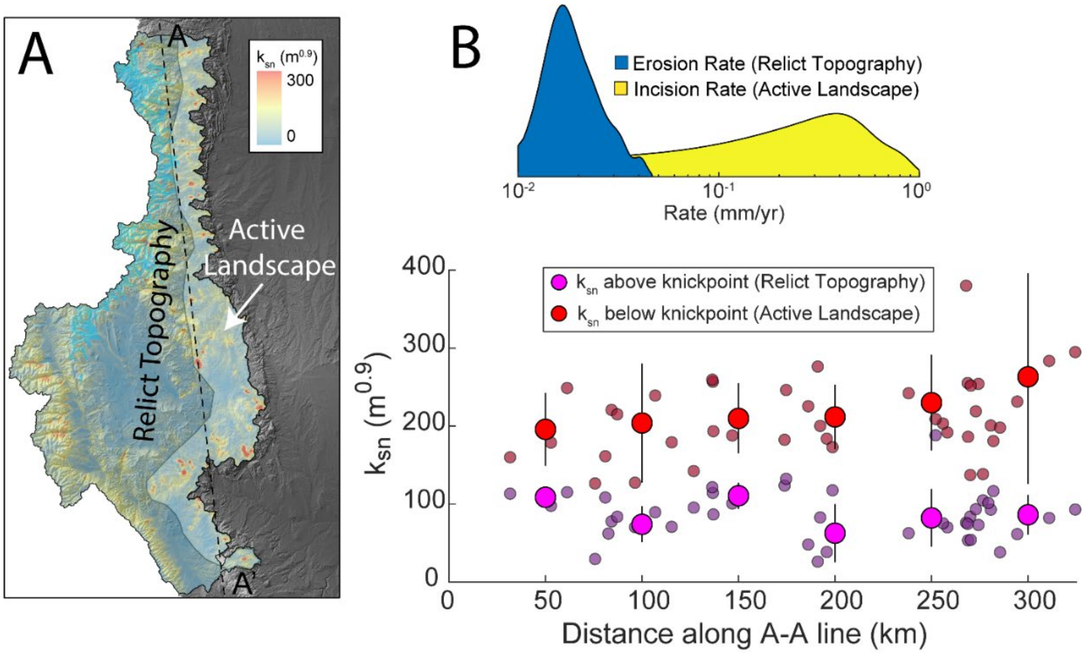

Figure 2.6 ***(A)*** *k_{sn} map for the Colorado Rockies as extrapolated from k_{sn} across the drainage network. Highlighted are the rejuvenated transient landscape below normal knickpoints at ~40 km upstream from the CR-HP boundary (transparent white polygon) and the relict topography above these knickpoints and east of the LGM glacier extent (cyan polygons). Also marked is the A-A' line used to project the knickpoint metrics in (B).* ***(B) (Inset)*** *Magnitude and distribution of basin average erosion rates and channel incision rates.* ***(Main)*** *k_{sn} in reaches above and below normal knickpoints as shown in Figure 5 once projected on a north to south line across the CR in (B). Transparent and non-transparent points are non-binned and binned data, respectively. The relict topography is consistent with low long-term basin average erosion rates of ~0.01-0.05 mm/yr and lower and consistent k_{sn} above normal knickpoints ~80-90 $m^{0.9}$. The rejuvenated landscape is consistent with higher channel incision rates of ~0.1-0.8 mm/yr and a systematic increase of k_{sn} below normal knickpoints from ~150 $m^{0.9}$ in the north CR to ~300 $m^{0.9}$ in the south CR.*

Chapter 3: Climate controls on fluvial topography[3]

3.1 Introduction

Geologists and geomorphologists have long been motivated to understand the relationships between tectonics, climate, and landscape evolution (Molnar and England, 1990; Whipple et al., 1999; Willett, 1999). In the last decades, there has been a concerted effort by geomorphologists to characterize and quantify the impact of climate on landscape evolution in natural settings (e.g., Riebe et al., 2001; von Blanckenburg, 2005; Harel et al., 2016; Chen et al., 2019). Much of this work has focused on fluvially-dominated landscapes, where studies often compare long-term erosion rates from isotopic proxies (e.g., 10Be) with measurable climate proxies (e.g., mean annual precipitation). Such comparisons typically show little-to-no correlation between climate and erosion rate, which is used to argue that climate is not a first-order driver of landscape dynamics (e.g., Riebe et al., 2001; von Blanckenburg, 2005). In contrast, studies that carefully selected transient river systems with strong precipitation gradients show clear correlations between erosion rate or bulk erodibility and mean annual precipitation or precipitation variability (e.g., Moon et al., 2011; Ferrier et al., 2013; Gayer et al., 2019). Similarly, studies of morphologically steady-state bedrock rivers show that the functional relationship between fluvial topography and erosion rates systematically changes with precipitation, where all else being equal, basins that receive higher precipitation rates are less steep than basins that receive less rainfall (Adams et al., 2020).

These studies highlight two critical points. First, climate appears to have a measurable impact on landscape response time and bulk erodibility, such that for transient landscapes, basins that receive more precipitation will attain equilibrium faster and will have higher time-averaged erosion rates during landscape adjustment relative to basins that receive less precipitation (e.g., Ferrier et al., 2013). Second, at steady state, the climate signal is recorded in topography rather than in the long-term erosion rate because topography dynamically adjusts its geometry to erode and transport sediment at a rate equal to the tectonically or isostatically imposed rock uplift rate (Hack, 1960; Whipple et al., 1999; Adams et al., 2020). While such studies demonstrate that climate can impact landscapes at local-to-regional scales, no systematic global analysis has been conducted to determine if there is a climate signature encoded in landscape morphology globally.

---

[3] Chapter is in review for Geology as Marder, E. and Gallen, S.F., Climate controls on fluvial topography. Preprint DOI: https://eartharxiv.org/repository/dashboard/3139/10.31223/X5DS6B

Here, we fill this knowledge gap by conducting a global analysis of fluvially-dominated bedrock basins that appear to be morphologically in steady-state and that incise into similar crystalline rock types (56, Figure C1, Figure C2). Leveraging an existing global compilation of cosmogenic 10Be-derived erosion rates, a digital elevation model (DEM), global rock type, and global climate proxy data sets, we test for relationships between climate and landscape morphology (Figure C1, Figure C2; Table C1). Through this analysis, we demonstrate a clear, systematic relationship between climate and topography that points to specific controlling mechanisms. We conclude by discussing the implications of these mechanisms in the context of climate, hydrology, and landscape evolution.

3.2 Materials and Methods

Tectonic geomorphology studies consistently demonstrate that in bedrock river systems, long-term erosion rate, E, and the normalized channel steepness, k_{sn}, defined as the local channel steepness normalized to its upstream drainage area, are empirically related via a power function (DiBiase et al., 2010; Kirby and Whipple, 2012; Lague, 2014; Harel et al., 2016):

$$E = Ck_{sn}{}^{p} \qquad (1),$$

where C and p are empirical constants. Numerous empirical studies and theoretical models for bedrock river incision that include incision thresholds and stochastic flood distributions, show that the relationship between E and k_{sn} is well described by equation 1 and largely controlled by hydroclimate (Appendix C; Lague et al., 2005; DiBiase and Whipple, 2011; Lague, 2014; Deal et al., 2018).

Here we explore p in the context of changes in mean annual precipitation (MAP), aridity index (AI), mean annual temperature (MAT), and mean basin elevation (ME) (Figure C1). We use an existing standardized global compilation of basin average erosion rates derived from 10Be concentrations in quartz-rich fluvial sands in fluvially-dominated basins (56, Figure C1; Table C1; Codilean et al., 2018). We derive the average k_{sn}, and a MAP-weighted version of this metric, $k_{sn}Q$ (Adams et al., 2020), for each of these basins, using a 3-arc second Shuttle Radar Topographic Mission (SRTM) DEM and a global MAP dataset (Figure C1; Table C1; ‘WorldClim 2’; Fick and Hijmans, 2017). We calculate k_{sn} from the slope of a linear regression through the river network elevation, z, and the transformed distance coordinate χ (known as χ-plots) for areas draining ≥ 1 km2 (Appendix C; 56, inset; Perron et al., 2013) using a reference concavity index of 0.5, which is a common value for many river systems globally (Appendix C; Kirby and Whipple, 2012; Harel et al., 2016).

To best isolate the climate signal on fluvial topography, we attempt to control for rock type and uplift rate related changes in erodibility by restricting our analysis to bedrock rivers that drain ≥ 90% crystalline rocks ('GLiM'; Hartmann and Moosdorf, 2012; note distribution of plutonic and metamorphic units exhibit no systematic relationship with climate proxies; Appendix C; Figure C2; Table C1) and basins that appear to be morphologically in steady-state with an R^2 ≥ 0.9 in χ-plots (56, inset; although note we do not find results presented herein to be sensitive to changes in R^2; Appendix C; Table C2). We also restrict our analysis to basins draining ≥ 10 km2 to reduce potential biases in 10Be concentrations imposed by land sliding (Yanites et al., 2009) and basins with MAP > 200 mm/yr to ensure that fluvial erosion is the dominant landscape denudation process.

For the remaining basins, we calculate the average values for MAP, MAT ('WorldClim 2'; Fick and Hijmans, 2017), AI ('CGIAR-CSI'; Trabucco and Zomer, 2009), and ME (SRTM DEM) (Table C1). We bin the $E - k_{sn}$ and $E - k_{sn}Q$ data by increments of each respective climate variable, ensuring an equal number of data points in each bin, with minimum of 15 data points per bin (Figure C3). We calculate p and C for each climate bin using total least-square linear regressions through the log-transformed $E - k_{sn}$ and $E - k_{sn}Q$ data (Figure C4). In a separate analysis, we attempt to account for the general nonlinearity in the global dataset by conducting normalized regressions using a fixed p of 2.2 based on a regression through the entire dataset, to calculate the normalized y-intercept, C_{ne}, for each climate bin (Appendix C; Figure C5; Harel et al., 2016; Adams et al., 2020). For each regression in these analyses, we estimate goodness-of-fit by calculating the R^2, χ^2, and Kolmogorov-Smirnov two-sided p-value test at the 90% significance level for each regression (Figure C3, Figure C5; Table C2). We conduct several sensitivity analyses to evaluate the robustness of signals in p with changes in climate proxies by changing the number of bins for each climate variable and changing the R^2 threshold used to define morphological steady-state (Appendix C; Figure C6). For each of these tests, we estimate the same goodness-of-fit metrics described above (Table C2).

3.3 Climate control on E-k_{sn} nonlinearity

Our results show systematic changes in the functional relationship between E and k_{sn} or $k_{sn}Q$ with changes in MAP and AI (Figure 3.2, Figure C3). Because C and p in equation 1 covary, we focus on the exponent, p, which determines the degree of nonlinearity in the $E - k_{sn}$ and $E - k_{sn}Q$ relationships. We find that p systematically increases with increasing MAP (i.e., wetter) and AI (i.e., more humid) values (Figure 3.3, Figure C4; Table C2). For an increase in MAP from 500 to 4000 mm/yr and an increase of AI from 0.25 to 2, p increases from ~1.5-2 to ~3.5-4, with a slightly higher goodness-of-fit for AI (Figure 3.3,

Figure C4; Table C2). We note that regressions for the highest MAP (>1717 mm/yr) and AI (>2) bins fit the data poorly (Figure 3.2, Figure C3, Figure C6; Table C2). These poor fits are likely due to the high chemical weathering in extremely wet and humid settings, which bias the typical relationship between denudation rates and 10Be concentrations, making standard calculations of basin average erosion rate from 10Be concentrations unreliable (e.g., Riebe and Granger, 2013). Excluding these high MAP and AI values, all other fits, which span most of the range of global climate conditions, show statistically significant relationships between E and k_{sn} with systematic changes in MAP and AI (Figure 3.2, Figure C3, Figure C6; Table C2). We do not find significant fits and systematic changes in p with ME and MAT (Figure C3, Figure C4, Figure C6; Table C2). Under a fixed p of 2.2, C_{ne} generally decreases from ~10-8m-7yr-1 to ~10-9m-8yr-1 with increasing MAP and AI, but have poor fits, suggesting that variations in the degree of nonlinearity is critical to explain the data (Figure C5; Table C2). Importantly, p values derived from E - $k_{sn}Q$ data show similar climate sensitivity as E - k_{sn}, implying that the incorporation of precipitation patterns do not explain systematic variations in fluvial topography with climate at the global scale (Figure 3.3, Figure C3, Figure C5; cf. Adams et al., 2020). For both $E - k_{sn}$ and $E - k_{sn}Q$, sensitivity analyses show that systematic changes in p as a function of changes in MAP and AI are statistically robust to the number of climate bins used to segregate data and the R^2 threshold used to define morphologically steady-state basins (Figure 3.3, Figure C6; Table C2).

3.4 Interpretation of climate control on fluvial topography

Our results demonstrate a clear climate signal in topographic form based on systematic variations in the degree of nonlinearity of $E - k_{sn}$ (i.e., changing p) as a function of MAP and AI (Figure 3.2, Figure 3.3, Figure C3, Figure C6). We interpret these findings in the context of simple models for detachment-limited bedrock channel incision that account for stochastic flood distributions and incision thresholds (herein STIMs; Appendix C). STIMs predict systematic changes in p as a function of flood distributions when incision thresholds are significant (Appendix C; Lague et al., 2005; Lague, 2014; Deal et al., 2018). For instance, in threshold-dominated bedrock channels, p will systematically decline with increasing discharge variability (Lague et al., 2005; DiBiase and Whipple, 2011). Further, empirical studies and simple soil-layer hydrology models show that discharge variability decreases with higher mean annual precipitation and lower aridity (Appendix C; Molnar et al., 2006; Lague, 2014; Deal et al., 2018). Thus, in bedrock channels where incision thresholds are relevant, the nonlinearity between E and k_{sn} is expected to increase with higher mean annual precipitation and decreasing aridity, which is precisely what our result show (Figure 3.2, Figure C3).

The dependency of the degree of nonlinearity between E and k_{sn} (i.e., p) on discharge variability can be visualized using STIMs as a function of the normalized incision threshold (defined as the ratio of incision threshold to erosion rate, ψ/E) and discharge variability (Appendix C; 59A; Lague et al., 2005). In this model, discharge variability is approximated with an inverse gamma distribution via a shape parameter, k, where low to high k represents high to low variability (Appendix C; Lague et al., 2005). By comparing predicted k and p values from STIMs under locally-calibrated parameters (DiBiase and Whipple, 2011; Lague, 2014) with empirically determined k and p values from discharge daily records near some of our analyzed basins, we find that in both cases, k increases from ~0.1 to 3, and p increases from ~1 to 5 with increasing MAP and AI, consistent with both our global analysis and previous studies (Appendix C; Figure 3.3, 59, Figure C7; Molnar et al., 2006; Lague, 2014; Deal et al., 2018). Thus, assuming STIMs are representative for the analyzed basins in this study, our results imply that incision thresholds are important, and that discharge variability decreases with increasing MAP and AI globally.

While, generally, STIMs provide a simple framework to explain our results, some nuances in our analysis are still not fully resolved. For example, p calculated for $E - k_{sn}Q$ and, C_{ne}, which attempt to control for some of the climate influence, show systematic variations with climate proxies (Figure C3, Figure C5). This finding suggests that climate-related variables studied and invoked here cannot fully account for observed variations in topography, and that other factors, such as the magnitude of incision threshold, grain size distribution, channel width scaling, rock type, and dominant incision process, likely covary with the climate regime. Future efforts to understand the relationships between climate and landscape evolution in fluvially-dominated systems will ultimately reveal other dominant channel incision mechanisms that are most sensitive to climate. Despite some lingering questions, our results demonstrate a clear and systematic change in the degree of nonlinearity between E and k_{sn} or $k_{sn}Q$ as a function of MAP and AI, providing compelling evidence for a correlation between landscape morphology and climate on a global scale (Figure 3.2, Figure 3.3, Figure C3, Figure C6).

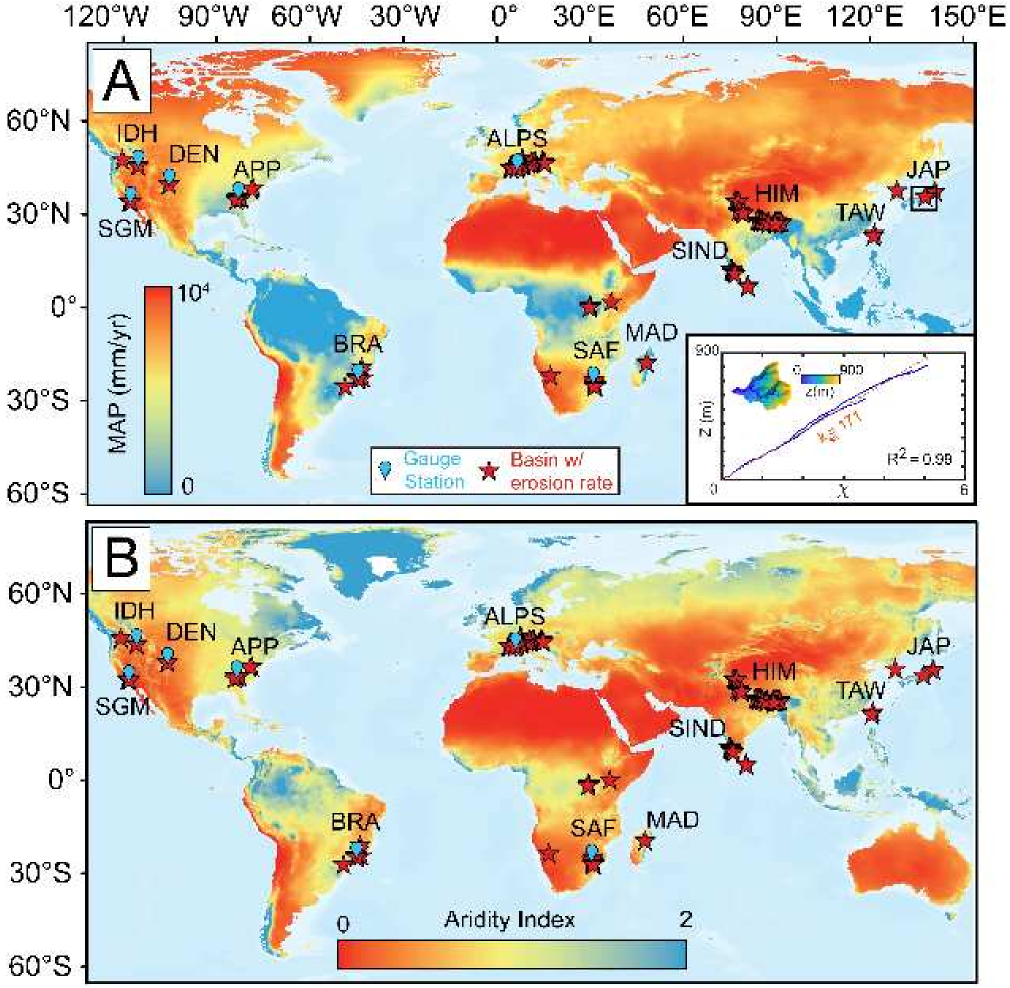

Figure 3.1 ***(A) (Inset)*** *k_{sn} calculation from river profiles in χ-z space in a steady-state basin in Japan (black square in A); we use a similar method to calculate $k_{sn}Q$ (see Appendix C; Figure C3).* ***(Main)*** *Global mean annual precipitation map (Fick and Hijmans, 2017) with locations of the analyzed steady-state basins with existing basin average erosion rates from the Octopus archive (Codilean et al., 2018). Also marked are the locations of stream gauge stations in Figures 4 and C7. IDH = Idaho, USA; DEN = Denver, USA; App = Appalachians, USA; SGM = San Gabriel Mountains, USA; BRA = Florianopolis, Brazil; ALPS = European Alps; SAF = South Africa; MAD = Madagascar; SIND = Southwest India; TAW = Taiwan; JAP = Japan.* ***(B)*** *Global aridity index map (Trabucco and Zomer, 2009) with similar annotations as in (A).*

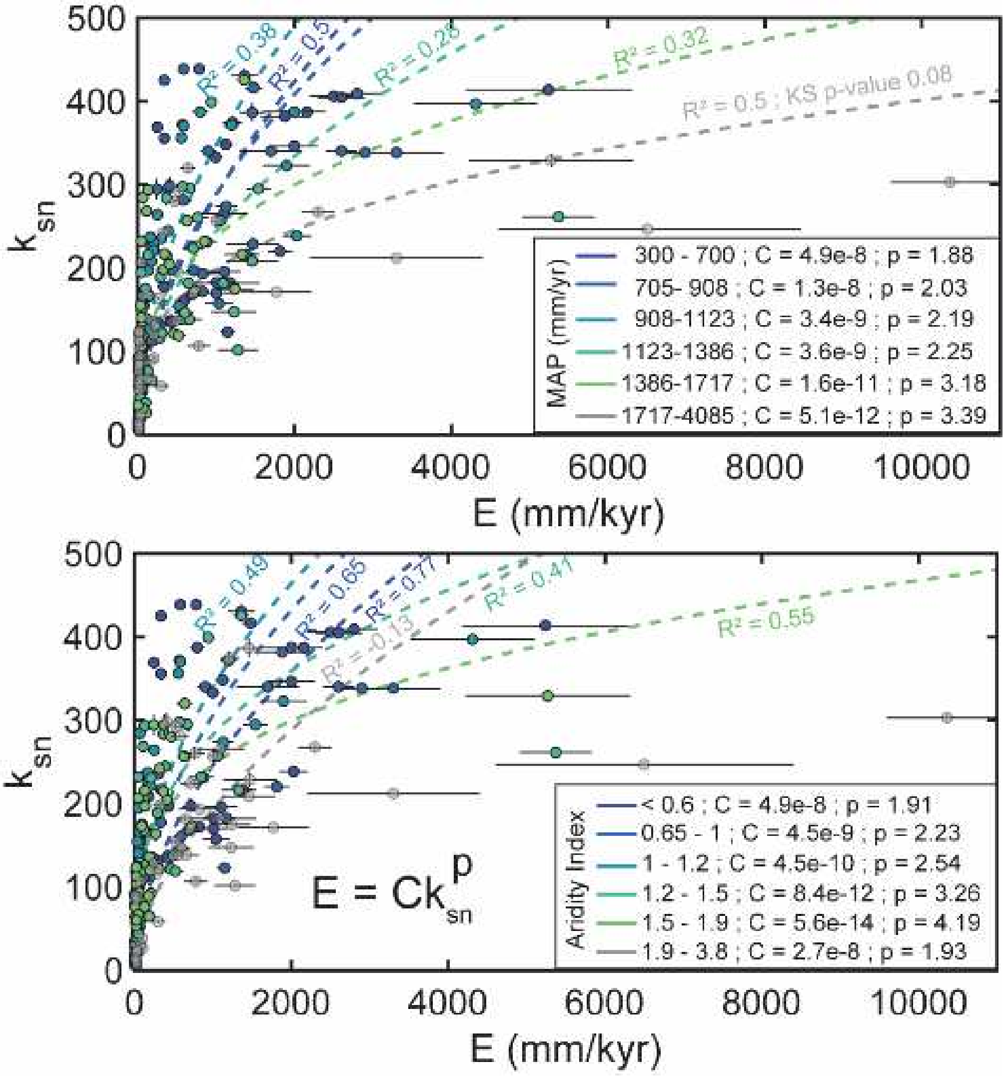

*Figure 3.2 Modeled regressions for k_{sn} versus E (equation 1) for 265 basins under a steady-state threshold of R^2 > 0.9 (Figure 1, inset; Figure C6; Table C1), where each data point represents one basin and is classified by its mean annual precipitation **(A)** and aridity index **(B)**. Noted are power law modeled regressions and their R^2 goodness-of-fit. For each climate bin, p and C are noted. For the highest MAP and AI climate bins, where goodness-of-fit is poor, regressions and data points are transparent and colored in grey. For full analysis, see Figure C3 and Table C2.*

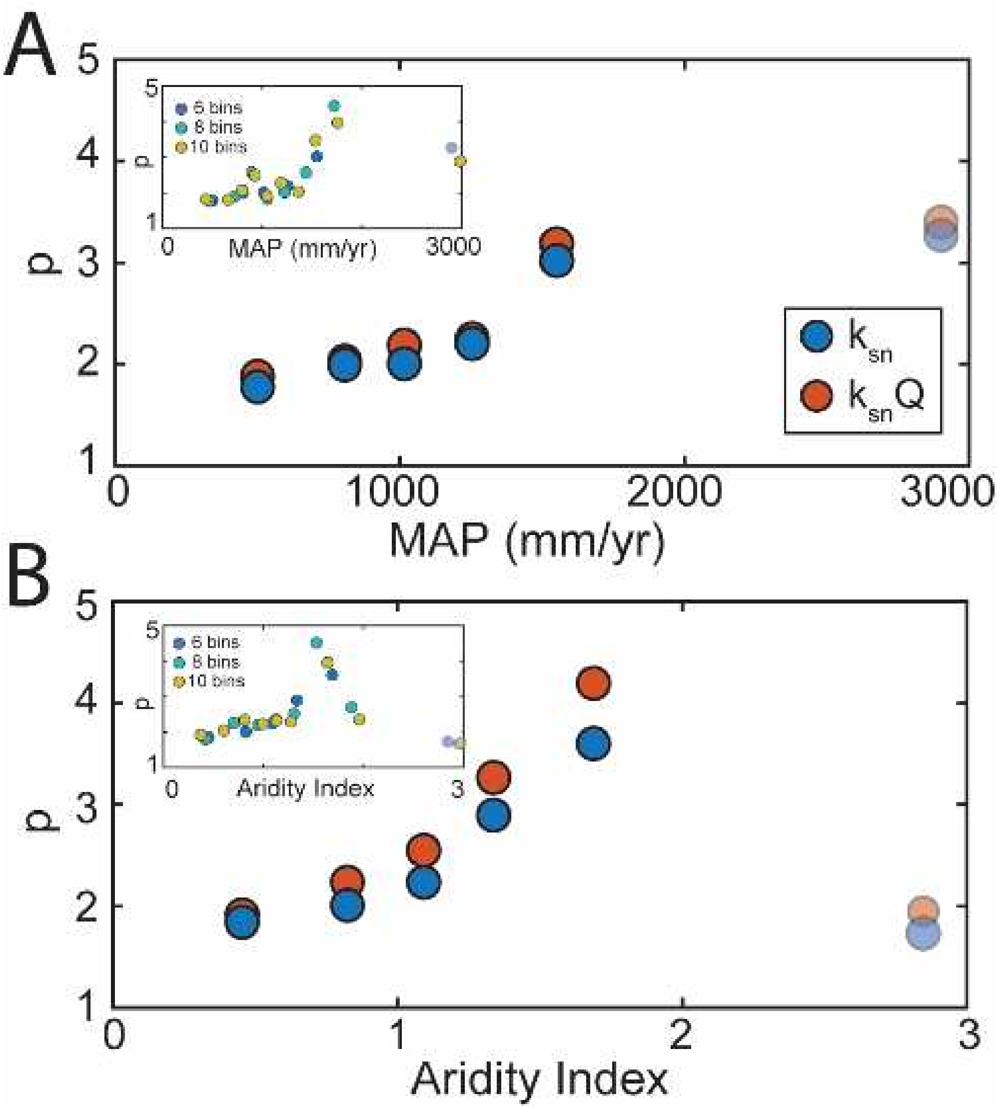

*Figure 3.3 p values for modeled regressions in Figure 2 with changes in **(A)** MAP and **(B)** AI. Inset figures show p values under different number of climate bins (for full analysis of p with changes in climate proxies, number of bins, and different R^2 thresholds, see Figure C4, Figure C6; Table C2). Note a systematic increase in p with increased MAP (i.e., wetter) and AI (i.e., higher humidity). $k_{sn}Q$ does not significantly change values or systematic patterns in p. p values from poor fits are transparent (Table C2).*

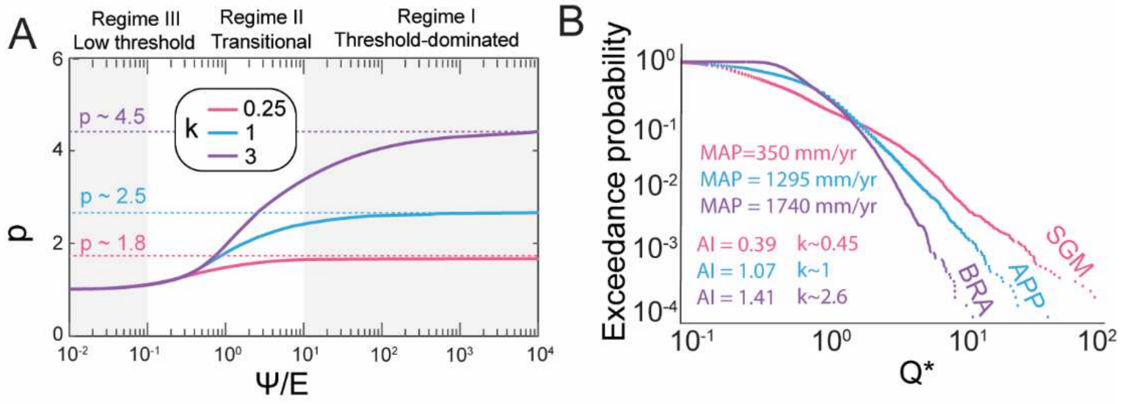

Figure 3.4 ***(A)*** *Modeled changes in* p *in equation 1 as a function of changes in the normalized threshold for channel incision,* ψ/E. ***(B)*** *Exceedance probability plots of mean daily discharge (m*^{3}*/s) recorded data in gauge stations near SGM, APP, and BRA (see locations in 56). Mentioned are MAP, AI, and calculated* k *for basins near the gauge stations (Appendix C; Figure C7). The range and systematic increase in* p *from ~1.8 to 4 with increasing MAP and AI correspond with theoretical predictions of increase of* p *from ~1.8 to 4.5 under a threshold dominated regime (Lague, 2014), where in both cases,* k *increases from ~0.25 to 3.*

Summary and future work

In this dissertation, I introduced and discussed the roles of tectonics and climate on fluvial topography from the local scale (chapter 1) to the regional scale (chapter 2) to the global scale (chapter 3). In chapter 1, I explored geomorphic markers of river knickpoints and fluvial terraces based on dominant bedrock lithology in the different physiographic provinces of the southern Colorado Front Range. In the eastern Rockies, I conducted river profile analysis and identified a series of concave down normal knickpoints that show an increase in elevation, channel steepness in river reaches below them, and total magnitude of incision at their basin outlets as a function of downstream distance along the upper Arkansas River from Cotopaxi, CO to Canon City, CO. In the western High Plains, I mapped and analyzed six Pleistocene terrace units parallel to the Arkansas River from Canon City, CO to Pueblo, CO that also record an increase in total magnitude of incision as a function of downstream distance along the Arkansas River, as well as local active tectonics/uplift/faulting near Pueblo, CO, which is consistent with the high slope and stream power in the same area along the modern Arkansas River. I showed that isostatic response to the removal of material along the Arkansas River valley during the Quaternary cannot explain the total magnitude of deformation recorded in the western High Plains, and that additional tectonic-induced incision is necessary to explain these empirical observations. Collectively, I showed that the knickpoints in the eastern Rockies and the terraces in the western High Plains, all indicate on an increasing tectonic uplift rate from west to east as a function of downstream distance along the Arkansas River in southern Colorado. This long-wavelength of deformation of ~150 km and the sustained increase in tectonic uplift rate from west to east, cannot be explained by climate-induced increased erodibility or tectonic-induced down-to-the-east tilting, as previous studies suggested. Rather, this deformation extent, magnitude, and increased gradient from west to east are all consistent with a model of dynamic topography that swept the Colorado Front Range in the same direction in the last 5-10 Ma (Moucha et al. 2008, 2009).

In chapter 2, I extended the study in chapter 1 to the entire Colorado Front Range. I conducted a regional river profile analysis in the Colorado Rockies and combined it with new and existing basin average erosion rates and channel incision rates in the Colorado Rockies and High Plains. I showed that the dominant knickpoints in the Colorado Rockies are concave down normal knickpoints, similar to the knickpoints in the southern Colorado Front Range (chapter 1) and that these knickpoints all separate a relict topography with a consistent lower channel steepness in reaches above them from a transient topography with higher channel steepness that increases systematically from north to south in reaches below them. By reconstructing paleo-rivers of the Cache la Poudre and Arkansas rivers in northern and southern Colorado, respectively, I showed that channel incision rates below normal knickpoints are one order of magnitude higher than channel incision rates above them. These high and low incision rates below and above normal knickpoints, respectively, are consistent with higher local channel incision rates and lower basin average erosion rates all across the Colorado Front Range. These knickpoint and erosion/incision rate spatiotemporal patterns across the Colorado Front Range are inconsistent with predictions of climate-induced increased erodibility during the Quaternary. Rather, the results are more consistent with a long wavelength geodynamic signal with a gradient of increased tectonic uplift rate from north to south. This, together with the geodynamic signal from west to east in the southern Colorado Front Range (chapter 1), all imply on a migrating dynamic topography that impacted the region in the last 5-10 Ma (Moucha et al. 2008, 2009).

In chapter 3, I explored the role of climate on fluvial topography at the global scale by analyzing changes in the empirical non-linear relationship between long-term erosion rates and channel steepness. I used existing data of basin average erosion rates in basins that appear to be morphologically in steady state and calculated their average channel steepness. I then classified the data by commonly used climate proxies of mean annual precipitation and aridity index to explore their impact on the nonlinearity between erosion rate and channel steepness. The results from this analysis showed that at the global scale, erosion rate and channel steepness are becoming more nonlinearly related as the climate is wetter and more humid. I demonstrated how this increased nonlinearity with wetter and more humid climate is consistent with a stochastic threshold stream power incision model that takes into account thresholds for channel incision and discharge variability. By conducting this global analysis, I showed that climate is recorded in the topography via the empirical parameters that define nonlinearity between erosion rate and channel steepness, and that hydroclimate, rather than climate alone, is the main mechanism for how climate impacts fluvial topography at the global scale.

In the beginning of this dissertation, I introduced two unresolved questions in the field of tectonic geomorphology and landscape evolution:

- What drives landscape evolution in post-orogenic settings?
- What is the relative role of climate in landscape evolution at the global scale?

In these three chapters, I shed some light on these questions. In chapters 1 and 2, I demonstrated the significant impact of tectonics and geodynamics in driving topographic rejuvenation in post-orogenic settings. I showed that the magnitude of local to regional scale deformation in the Colorado Front Range is primarily dictated by the magnitude of tectonic uplift rate across the region. In chapter 3, I showed that climate controls the magnitude of relief produced for a given landscape via hydroclimate mechanisms and bedrock channel characteristics for both steady state and transient landscapes. Collectively, I showed that tectonics is the main driver for transient landscape evolution in Colorado and that climate is a first order control on the functional relationship between erosion rate and fluvial topography at the global scale.

Despite the promising outcomes introduced in this dissertation, some lingering questions require future work. For instance, what are the roles of lithological variability, lithological strength, divide migration, and drainage reorganization in the Colorado Front Range and other post-orogenic settings worldwide? What are the roles of channel geometry, grain size distribution, rock type, and incision thresholds in hydroclimate interactions with steady-state and transient fluvial topographies? These and other similar questions in the field of tectonic geomorphology should be further addressed to better understand long-term landscape evolution at different spatiotemporal scales.

References

Abbey, A.L., and Niemi, N.A., 2018, Low-temperature thermochronometric constraints on fault initiation and growth in the northern Rio Grande rift, upper Arkansas River valley, Colorado, USA: Geology, v. 46, p. 627–630, doi:10.1130/G40232.1.

Abbey, A.L., Niemi, N.A., Geissman, J.W., Winkelstern, I.Z., and Heizler, M., 2018, Early Cenozoic exhumation and paleotopography in the Arkansas River valley, southern Rocky Mountains, Colorado: Lithosphere, v. 10, p. 239–266, doi:10.1130/L673.1.

Abbott, J.T., 1976, Geologic map of the Big Narrows quadrangle, Larimer County, Colorado: USGS.

Adamiec, G., and Aitken, M.J., 1998, Dose-rate conversion factors: update: Ancient Tl, v. 16, p. 37–50.

Adams, B.A., Whipple, K.X., Forte, A.M., Heimsath, A.M., and Hodges, K.V., 2020, Climate controls on erosion in tectonically active landscapes: Science Advances, v. 6, p. eaaz3166, doi:10.1126/sciadv.aaz3166.

Aitken, M.J., and Alldred, J.C., 1972, The assessment of error limits in thermoluminescent dating: Archaeometry, v. 14, p. 256–267.

Antonelli, A. et al., 2018, Geological and climatic influences on mountain biodiversity: Nature Geoscience, v. 11, p. 718–725, doi:10.1038/s41561-018-0236-z.

Auclair, M., Lamothe, M., and Huot, S., 2003, Measurement of anomalous fading for feldspar IRSL using SAR: Radiation Measurements, v. 37, p. 487–492, doi:10.1016/S1350-4487(03)00018-0.

Balco, G., Stone, J.O., Lifton, N.A., and Dunai, T.J., 2008, A complete and easily accessible means of calculating surface exposure ages or erosion rates from 10Be and 26Al measurements: Quaternary Geochronology, v. 3, p. 174–195, doi:10.1016/j.quageo.2007.12.001.

Beeson, H.W., McCoy, S.W., and Keen-Zebert, A., 2017, Geometric disequilibrium of river basins produces long-lived transient landscapes: Earth and Planetary Science Letters, v. 475, p. 34–43, doi:10.1016/j.epsl.2017.07.010.

Berlin, M.M., and Anderson, R.S., 2007, Modeling of knickpoint retreat on the Roan Plateau, western Colorado: Journal of Geophysical Research, v. 112, p. F03S06, doi:10.1029/2006JF000553.

Bierman, P., and Steig, E.J., 1996, Estimating Rates of Denudation Using Cosmogenic Isotope Abundances in Sediment: Earth Surface Processes and Landforms, v. 21, p. 125–139.

Bird, P., 1998, Kinematic history of the Laramide orogeny in latitudes 35°-49°N, western United States: Tectonics, v. 17, p. 780–801, doi:10.1029/98TC02698.

Birkeland, P.W., Miller, D.C., Patterson, P.E., Price, A.B., and Shroba, R.R., 1999, Soil-geomorphic Relationships Near Rocky Flats, Boulder and Golden, Colorado Area, with a Stop at the Pre-Fountain Formation Paleosol of Wahlstrom (1948): Geological Society of America Field Trip, v. 18, p. 13.

Blackburn, T., Ferrier, K.L., and Perron, J.T., 2018, Coupled feedbacks between mountain erosion rate, elevation, crustal temperature, and density: Earth and Planetary Science Letters, v. 498, p. 377–386, doi:10.1016/j.epsl.2018.07.003.

von Blanckenburg, F., 2005, The control mechanisms of erosion and weathering at basin scale from cosmogenic nuclides in river sediment: Earth and Planetary Science Letters, v. 237, p. 462–479, doi:10.1016/j.epsl.2005.06.030.

Bøtter-Jensen, L., Andersen, C.E., Duller, G.A.T., and Murray, A.S., 2003, Developments in radiation, stimulation and observation facilities in luminescence measurements: Radiation Measurements, v. 37, p. 535–541, doi:10.1016/S1350-4487(03)00020-9.

Braddock, W.A., 1988, Geologic map of the Poudre Park quadrangle, Larimer County, Colorado: USGS.

Brennan, B.J., 2003, Beta doses to spherical grains: Radiation Measurements, v. 37, p. 299–303, doi:10.1016/S1350-4487(03)00011-8.

Brown, R.W., 1943, Cretaceous-Tertiary boundary in the Denver Basin, Colorado: Geological Society of America Bulletin, v. 54, p. 65–86, doi:10.1130/GSAB-54-65.

Burbank, D.W., and Anderson, R.S., 2011, Tectonic geomorphology: John Wiley & Sons.

Buylaert, J.P., Murray, A.S., Thomsen, K.J., and Jain, M., 2009, Testing the potential of an elevated temperature IRSL signal from K-feldspar: Radiation Measurements, v. 44, p. 560–565, doi:10.1016/j.radmeas.2009.02.007.

Chapin, C.E., and Kelley, S.A., 1997, The Rocky Mountain Erosion Surface in the Front Range of Colorado: Colorado Front Range Guidebook, p. 101–114.

Chen, S.-A., Michaelides, K., Grieve, S.W.D., and Singer, M.B., 2019, Aridity is expressed in river topography globally: Nature, v. 573, p. 573–577, doi:10.1038/s41586-019-1558-8.

Clarey, T.L., Chase, R.B., and Schmidt, C.J., 2004, Precambrian Influences on the Development of the Royal Gorge Arch, Colorado: A Thick-Skinned Fault-Propagation Fold: The Mountain Geologist, v. 41, p. 17–32.

Codilean, A.T., Munack, H., Cohen, T.J., Saktura, W.M., Gray, A., and Mudd, S.M., 2018, OCTOPUS: an open cosmogenic isotope and luminescence database: Earth System Science Data, v. 10, p. 2123–2139, doi:10.5194/essd-10-2123-2018.

Crone, A.J., and Haller, K.M., 2015, Fault number 2330, Cheraw fault: USGS Quaternary fault and fold database of the United States: U.S. Geological Survey.

Crosby, B.T., and Whipple, K.X., 2004, Knickpoint initiation and distribution within fluvial networks: 236 waterfalls in the Waipaoa River, North Island, New Zealand: Geomorphology, v. 82, p. 16–38, doi:10.1016/j.geomorph.2005.08.023.

Damon, P.E., 1983, Continental uplift, compensation and shunting during trench-spreading center collision: Tectonophysics, v. 99, p. T1–T8, doi:10.1016/0040-1951(83)90165-8.

Davis, W.M., 1889, The rivers and valleys of Pennsylvania: National Geographic Society.

Deal, E., Braun, J., and Botter, G., 2018, Understanding the Role of Rainfall and Hydrology in Determining Fluvial Erosion Efficiency: Journal of Geophysical Research: Earth Surface, v. 123, p. 744–778, doi:10.1002/2017JF004393.

DeCelles, P.G., 2004, Late Jurassic to Eocene evolution of the Cordilleran thrust belt and foreland basin system, western U.S.A.: American Journal of Science, v. 304, p. 105–168, doi:10.2475/ajs.304.2.105.

Dethier, D.P., Ouimet, W., Bierman, P.R., Rood, D.H., and Balco, G., 2014, Basins and bedrock: Spatial variation in 10Be erosion rates and increasing relief in the southern Rocky Mountains, USA: Geology, v. 42, p. 167–170, doi:10.1130/G34922.1.

DiBiase, R.A., 2018, Short communication: Increasing vertical attenuation length of cosmogenic nuclide production on steep slopes negates topographic shielding corrections for catchment erosion rates: Earth Surface Dynamics, v. 6, p. 923–931, doi:10.5194/esurf-6-923-2018.

DiBiase, R.A., and Whipple, K.X., 2011, The influence of erosion thresholds and runoff variability on the relationships among topography, climate, and erosion rate: Journal of Geophysical Research, v. 116, p. F04036, doi:10.1029/2011JF002095.

DiBiase, R.A., Whipple, K.X., Heimsath, A.M., and Ouimet, W.B., 2010, Landscape form and millennial erosion rates in the San Gabriel Mountains, CA: Earth and Planetary Science Letters, v. 289, p. 134–144, doi:10.1016/j.epsl.2009.10.036.

Dickinson, W.R., Klute, M.A., Hayes, M.J., Janecke, S.U., and Lundin, E.R. Paleogeographic and paleotectonic setting of Laramide sedimentary basins in the central Rocky Mountain region: Geological Society of America Bulletin, v. 100, p. 1023–1039.

Dickinson, W.R., and Snyder, W.S., 1978, Plate tectonics of the Laramide orogeny, *in* Laramide Folding Associated with Basement Block Faulting in the Western United States, Geological Society of America, v. 3, p. 355–366.

Dühnforth, M., Anderson, R.S., Ward, D.J., and Blum, A., 2012, Unsteady late Pleistocene incision of streams bounding the Colorado Front Range from measurements of meteoric and in situ 10Be: Journal of Geophysical Research: Earth Surface, v. 117, p. n/a-n/a, doi:10.1029/2011JF002232.

Duller, R.A., Whittaker, A.C., Swinehart, J.B., Armitage, J.J., Sinclair, H.D., Bair, A., and Allen, P.A., 2012, Abrupt landscape change post–6 Ma on the central Great Plains, USA: Geology, v. 40, p. 871–874, doi:10.1130/G32919.1.

Eaton, G.P., 2008, Epeirogeny in the Southern Rocky Mountains region: Evidence and origin: Geoshpere, v. 4, p. 764–784, doi:10.1130/GES00149.1.

Epis, R.C., and Chapin, C.E., 1975, Geomorphic and tectonic implications of the post-Laramide, late Eocene erosion surface in the Southern Rocky Mountains, *in* Surface in the Southern Rocky Mountains, Geological Society of America, Geological Society of America Memoirs, v. 144, p. 45–74, doi:10.1130/MEM144-p45.

Epis, R.C., and Chapin, C.E., 1974, Stratigraphic nomenclature of the Thirtynine Mile volcanic field, central Colorado: USGS 1395.

Epis, R.C., Scott, G.R., Taylor, R.B., and Chapin, C.E., 1976, Cenozoic, volcanic, tectonic, and geomorphic features of central Colorado, *in* Studies in Colorado field geology, Professional Contributions of Colorado School of Mines 8, p. 323–338.

Epis, R.C., Wobus, R.A., and Scott, G.R., 1979, Preliminary geologic map of the Black Mountain Quadrangle, Fremont and Park counties, Colorado.:

Ferrier, K.L., Huppert, K.L., and Perron, J.T., 2013, Climatic control of bedrock river incision: Nature, v. 496, p. 206–209, doi:10.1038/nature11982.

Fick, S.E., and Hijmans, R.J., 2017, WorldClim 2: new 1-km spatial resolution climate surfaces for global land areas: International Journal of Climatology, v. 37, p. 4302–4315, doi:10.1002/joc.5086.

Fillon, C. et al., 2021, Post-orogenic exhumation in the western Pyrenees: evidence for extension driven by pre-orogenic inheritance: Journal of the Geological Society, v. 178, p. jgs2020- 079, doi:10.1144/jgs2020-079.

Finnegan, N.J., Schumer, R., and Finnegan, S., 2014, A signature of transience in bedrock river incision rates over timescales of 104–107 years: Nature, v. 505, p. 391–394, doi:10.1038/nature12913.

Fischer, K.M., 2002, Waning buoyancy in the crustal roots of old mountains: Nature, v. 417, p. 933–936, doi:10.1038/nature00855.

Fisher, G.B., Amos, C.B., Bookhagen, B., Burbank, D.W., and Godard, V., 2012, Channel widths, landslides, faults, and beyond: The new world order of high-spatial resolution Google Earth imagery in the study of earth surface processes, *in* Google Earth and Virtual Visualizations in Geoscience Education and Research, Geological Society of America, doi:10.1130/2012.2492(01).

Fisher, G.B., Bookhagen, B., and Amos, C.B., 2013, Channel planform geometry and slopes from freely available high-spatial resolution imagery and DEM fusion: Implications for channel width scalings, erosion proxies, and fluvial signatures in tectonically active landscapes: Geomorphology, v. 194, p. 46–56, doi:10.1016/j.geomorph.2013.04.011.

Flint, J.J., 1974, Stream gradient as a function of order, magnitude, and discharge: Water Resources Research, v. 10, p. 969–973, doi:10.1029/WR010i005p00969.

Forte, A.M., Yanites, B.J., and Whipple, K.X., 2016, Complexities of landscape evolution during incision through layered stratigraphy with contrasts in rock strength: Rock Strength and Landscape Evolution: Earth Surface Processes and Landforms, v. 41, p. 1736–1757, doi:10.1002/esp.3947.

Fülöp, R.-H. et al., 2020, Million-year lag times in a post-orogenic sediment conveyor: Science Advances, v. 6, p. eaaz8845, doi:10.1126/sciadv.aaz8845.

Galbraith, R.F., and Roberts, R.G., 2012, Statistical aspects of equivalent dose and error calculation and display in OSL dating: An overview and some recommendations: Quaternary Geochronology, v. 11, p. 1–27, doi:10.1016/j.quageo.2012.04.020.

Gallen, S.F., 2018, Lithologic controls on landscape dynamics and aquatic species evolution in post-orogenic mountains: Earth and Planetary Science Letters, v. 493, p. 150–160, doi:10.1016/j.epsl.2018.04.029.

Gallen, S.F., Pazzaglia, F.J., Wegmann, K.W., Pederson, J.L., and Gardner, T.W., 2015, The dynamic reference frame of rivers and apparent transience in incision rates: Geology, v. 43, p. 623–626, doi:10.1130/G36692.1.

Gallen, S.F., and Thigpen, J.R., 2018, Lithologic controls on focused erosion and intraplate earthquakes in the Eastern Tennessee Seismic Zone: Geophysical Research Letters, v. 45, p. 9569–9578, doi:10.1029/2018GL079157.

Gallen, S.F., and Wegmann, K.W., 2017, River profile response to normal fault growth and linkage: an example from the Hellenic forearc of south-central Crete, Greece: Earth Surface Dynamics, v. 5, p. 161–186, doi:10.5194/esurf-5-161-2017.

Gallen, S.F., Wegmann, K.W., and Bohnenstiehl, D.W.R., 2013, Miocene rejuvenation of topographic relief in the southern Appalachians: GSA Today, v. 23, p. 4–10, doi:10.1130/GSATG163A.1.

Galloway, W.E., Whiteaker, T.L., and Ganey-Curry, P., 2011, History of Cenozoic North American drainage basin evolution, sediment yield, and accumulation in the Gulf of Mexico basin: Geosphere, v. 7, p. 938–973, doi:10.1130/GES00647.1.

Gayer, E., Michon, L., Louvat, P., and Gaillardet, J., 2019, Storm-induced precipitation variability control of long-term erosion: Earth and Planetary Science Letters, v. 517, p. 61–70, doi:10.1016/j.epsl.2019.04.003.

Giachetta, E., Molin, P., Scotti, V.N., and Faccenna, C., 2015, Plio-Quaternary uplift of the Iberian Chain (central–eastern Spain) from landscape evolution experiments and river profile modeling: Geomorphology, v. 246, p. 48–67, doi:10.1016/j.geomorph.2015.06.005.

Giachetta, E., and Willett, S.D., 2018, Effects of river capture and sediment flux on the evolution of plateaus: insights from numerical modeling and river profile analysis in the Upper Blue Nile catchment: Journal of Geophysical Research: Earth Surface, v. 123, p. 1187–1217, doi:10.1029/2017JF004252.

Goren, L., Fox, M., and Willett, S.D., 2014a, Tectonics from fluvial topography using formal linear inversion: Theory and applications to the Inyo Mountains, California: Journal of Geophysical Research: Earth Surface, v. 119, p. 1651–1681, doi:10.1002/2014JF003079.

Goren, L., Willett, S.D., Herman, F., and Braun, J., 2014b, Coupled numerical-analytical approach to landscape evolution modeling: Earth Surface Processes and Landforms, v. 39, p. 522–545, doi:10.1002/esp.3514.

Grambling, J.A., and Tewksbury, B.J., 1989, Proterozoic geology of the southern Rocky Mountains: Geological Society of America, v. 235.

Granger, D.E., and Muzikar, P.F., 2001, Dating sediment burial with in situ-produced cosmogenic nuclides: theory, techniques, and limitations: Earth and Planetary Science Letters, v. 188, p. 269–281, doi:10.1016/S0012-821X(01)00309-0.

Granger, D.E., and Schaller, M., 2014, Cosmogenic Nuclides and Erosion at the Watershed Scale: Elements, v. 10, p. 369–373, doi:10.2113/gselements.10.5.369.

Green, G.N., 1992, The digital geologic map of Colorado in ARC/INFO format: USGS.

Guérin, G., Mercier, N., and Adamiec, G., 2011, Dose-rate conversion factors: update: Ancient Tl, v. 29, p. 5–8.

Hack, J.T., 1960, Interpretation of erosional topography in humid temperate regions: American Journal of Science, v. 258-A, p. 80–97.

Hansen, S.M., Dueker, K.G., Stachnik, J.C., Aster, R.C., and Karlstrom, K.E., 2013, A rootless Rockies-support and lithospheric structure of the Colorado Rocky Mountains inferred from CREST and TA seismic data: CREST: Geochemistry, Geophysics, Geosystems, v. 14, p. 2670–2695, doi:10.1002/ggge.20143.

Harel, M.-A., Mudd, S.M., and Attal, M., 2016, Global analysis of the stream power law parameters based on worldwide 10 Be denudation rates: Geomorphology, v. 268, p. 184–196, doi:10.1016/j.geomorph.2016.05.035.

Hartmann, J., and Moosdorf, N., 2012, The new global lithological map database GLiM: A representation of rock properties at the Earth surface: Geochemistry, Geophysics, Geosystems, v. 13, doi:10.1029/2012GC004370.

Haviv, I., Enzel, Y., Whipple, K.X., Zilberman, E., Matmon, A., Stone, J., and Fifield, K.L., 2010, Evolution of vertical knickpoints (waterfalls) with resistant caprock: Insights from numerical modeling: Journal of Geophysical Research, v. 115, p. F03028, doi:10.1029/2008JF001187.

Heede, B.H., 1970, Morphology of Gullies in the Colorado Rocky Mountains: International Association of Scientific Hydrology. Bulletin, v. 15, p. 79–89, doi:10.1080/02626667009493955.

Heller, P.L., Dueker, K., and McMillan, M.E., 2003, Post-Paleozoic alluvial gravel transport as evidence of continental tilting in the U.S. Cordillera: Bulletin of the Geological Society of America, v. 115, p. 1122–1132, doi:10.1130/B25219.1.

Heller, P.L., and Liu, L., 2016, Dynamic topography and vertical motion of the U.S. Rocky Mountain region prior to and during the Laramide orogeny: Geological Society of America Bulletin, v. 128, p. 973–988, doi:10.1130/B31431.1.

Hergarten, S., Robl, J., and Stüwe, K., 2016, Tectonic geomorphology at small catchment sizes – extensions of the stream-power approach and the chi method: Earth Surface Dynamics, v. 4, p. 1–9, doi:10.5194/esurf-4-1-2016.

Holbrook, J., and Schumm, S.A., 1999, Geomorphic and sedimentary response of rivers to tectonic deformation: a brief review and critique of a tool for recognizing subtle epeirogenic deformation in modern and ancient settings: Tectonophysics, v. 305, p. 287–306, doi:10.1016/S0040-1951(99)00011-6.

Howard, A.D., 1994, A detachment-limited model of drainage basin evolution: Water Resources Research, v. 30, p. 2261–2285, doi:10.1029/94WR00757.

Huntley, D.J., and Baril, M.R., 1997, The K content of the K-feldspars being measured in optical dating or in thermoluminescence dating: Ancient Tl, v. 15, p. 11–13.

Huntley, D.J., and Hancock, R.G.V., 2001, The Rb contents of the K-feldspar grains being measured in optical dating: Ancient Tl, v. 19, p. 43–46.

Huntley, D.J., and Lamothe, M., 2001, Ubiquity of anomalous fading in K-feldspars and the measurement and correction for it in optical dating: Canadian Journal of Earth Sciences, v. 38, p. 1093–1106.

Jones, C.H., Mahan, K.H., Butcher, L.A., Levandowski, W.B., and Farmer, G.L., 2015, Continental uplift through crustal hydration: Geology, v. 43, p. 355–358, doi:10.1130/G36509.1.

Karlstrom, K.E. et al., 2012, Mantle-driven dynamic uplift of the Rocky Mountains and Colorado Plateau and its surface response: Toward a unified hypothesis: Lithosphere, v. 4, p. 3–22, doi:10.1130/L150.1.

Keller, S.M., and Morgan, M.L., 2016, Overview of the Eocene Castle Rock Conglomerate, east-central Colorado: remapping the fluvial system, and implications for the history of the Colorado Piedmont and Front Range, *in* Unfolding the Geology of the West, Geological Society of America, Field Guides 44, p. 125–141.

Kelley, S.A., Chapin, C.E., and Corrigan, J., 1992, Late Mesozoic to Cenozoic Cooling Histories of the Flanks of the Northern and Central Rio Grande rift, Colorado and New Mexico: New Mexico Bureau of Mines & Mineral Resources, v. 145, p. 1–40.

Kirby, E., and Whipple, K.X., 2012, Expression of active tectonics in erosional landscapes: Journal of Structural Geology, v. 44, p. 54–75, doi:10.1016/j.jsg.2012.07.009.

Kluth, C.F., and Coney, P.J., 1981, Plate tectonics of the Ancestral Rocky Mountains: Geology, v. 9, p. 10–15.

Kluth, C.F., and Nelson, S.N., 1988, Age of the Dawson Arkose, Southwestern Air Force Academy, Colorado, and Implications for the Uplift History of the Front Range: The Mountain Geologist, v. 25, p. 29–35.

Kohl, C.P., and Nishiizumi, K., 1992, Chemical isolation of quartz for measurement of in-situ -produced cosmogenic nuclides: Geochimica et Cosmochimica Acta, v. 56, p. 3583–3587, doi:10.1016/0016-7037(92)90401-4.

Lague, D., 2014, The stream power river incision model: evidence, theory and beyond: Earth Surface Processes and Landforms, v. 39, p. 38–61, doi:10.1002/esp.3462.

Lague, D., Hovius, N., and Davy, P., 2005, Discharge, discharge variability, and the bedrock channel profile: Journal of Geophysical Research: Earth Surface, v. 110, p. n/a-n/a, doi:10.1029/2004JF000259.

Langston, A.L., Tucker, G.E., and Anderson, R.S., 2015, Interpreting climate-modulated processes of terrace development along the Colorado Front Range using a landscape evolution model: Journal of Geophysical Research: Earth Surface, v. 120, p. 2121–2138, doi:10.1002/2014JF003403.

Larsen, I.J., Montgomery, D.R., and Greenberg, H.M., 2014, The contribution of mountains to global denudation: Geology, v. 42, p. 527–530, doi:10.1130/G35136.1.

Lavé, J., and Avouac, J.P., 2000, Active folding of fluvial terraces across the Siwaliks Hills, Himalayas of central Nepal: Journal of Geophysical Research: Solid Earth, v. 105, p. 5735–5770, doi:10.1029/1999JB900292.

Lazear, G., Karlstrom, K., Aslan, A., and Kelley, S., 2013, Denudation and flexural isostatic response of the colorado plateau and southern rocky mountains region since 10 Ma: Geosphere, v. 9, p. 792–814, doi:10.1130/GES00836.1.

Leonard, E.M., 2002, Geomorphic and tectonic forcing of late Cenozoic warping of the Colorado piedmont: Geology, v. 30, p. 595–598.

Lindsey, D.A., Langer, W.H., and Knepper, D.H., 2005, Stratigraphy, lithology, and sedimentary features of Quaternary alluvial deposits of the South Platte River and some of its tributaries east of the Front Range, Colorado: USGS Professional Paper 1705.

Liu, L., Gurnis, M., Seton, M., Saleeby, J., Müller, R.D., and Jackson, J.M., 2010, The role of oceanic plateau subduction in the Laramide orogeny: Nature Geoscience, v. 3, p. 353–357, doi:10.1038/ngeo829.

Madole, R.F., 1991, Colorado Piedmont, *in* Morrison, R.B. ed., Quaternary geology of the northern Great Plains, Geological Society of America, K-2, p. 456–475, doi:10.1130/DNAG-GNA-K2.441.

Madole, R.F., Van Sistine, D.P., and Michael, J.A., 1998, Pleistocene glaciation in the upper Platte River drainage basin, Colorado: USGS 2644, 10.3133/i2644.

Marder, E., Bookman, R., and Filin, S., 2018, Geomorphological response of the Lower Jordan River basin to active tectonics of the Dead Sea Transform: Geomorphology, v. 317, p. 75–90, doi:10.1016/j.geomorph.2018.05.018.

Marder, E., Gallen, S.F., and Pazzaglia, F.J. Late Cenozoic deformation in the Southern Colorado Front Range revealed by river profile analysis and fluvial terraces (In review): Geological Society of America Bulletin,.

McMillan, M.E., Angevine, C.L., and Heller, P.L., 2002, Postdepositional tilt of the Miocene-Pliocene Ogallala Group on the western Great Plains: Evidence of late Cenozoic uplift of the Rocky Mountains: Geology, v. 30, p. 64–66.

McMillan, M.E., and Heller, P.L., 2006, History and causes of post-Laramide relief in the Rocky Mountain orogenic plateau: Geological Society of America Bulletin, v. 118, p. 393–405, doi:10.1130/B25712.1.

Merrick & Co, 2019, Classified LAS 1.4 QL2: Merrick & Co LAS data.

Miller, S.R., Sak, P.B., Kirby, E., and Bierman, P.R., 2013, Neogene rejuvenation of central Appalachian topography: Evidence for differential rock uplift from stream profiles and erosion rates: Earth and Planetary Science Letters, v. 369–370, p. 1–12, doi:10.1016/j.epsl.2013.04.007.

Mitchell, N.A., and Yanites, B.J., 2019, Spatially variable increase in rock uplift in the Northern U.S. Cordillera recorded in the distribution of river knickpoints and incision depths: Journal of Geophysical Research: Earth Surface, v. 124, p. 1238–1260, doi:10.1029/2018JF004880.

Mitrovica, J.X., Beaumont, C., and Jarvis, G.T., 1989, Tilting of continental interiors by the dynamical effects of subduction: Tectonics, v. 8, p. 1079–1094, doi:10.1029/TC008i005p01079.

Molnar, P., Anderson, R.S., Kier, G., and Rose, J., 2006, Relationships among probability distributions of stream discharges in floods, climate, bed load transport, and river incision: Journal of Geophysical Research, v. 111, p. F02001, doi:10.1029/2005JF000310.

Molnar, P., and England, P., 1990, Late Cenozoic uplift of mountain ranges and global climate change: Chicken or egg? Nature, v. 346, p. 29–34, doi:10.1038/346029a0.

Molnar, P., England, P.C., and Jones, C.H., 2015, Mantle dynamics, isostasy, and the support of high terrain: Journal of Geophysical Research: Solid Earth, v. 120, p. 1932–1957, doi:10.1002/2014JB011724.

Moodie, A.J., Pazzaglia, F.J., and Berti, C., 2018, Exogenic forcing and autogenic processes on continental divide location and mobility: Basin Research, v. 30, p. 344–369, doi:10.1111/bre.12256.

Moon, S., Page Chamberlain, C., Blisniuk, K., Levine, N., Rood, D.H., and Hilley, G.E., 2011, Climatic control of denudation in the deglaciated landscape of the Washington Cascades: Nature Geoscience, v. 4, p. 469–473, doi:10.1038/ngeo1159.

Morgan, P., Seager, W.R., and Golombek, M.P., 1986, Cenozoic thermal, mechanical and tectonic evolution of the Rio Grande Rift: Journal of Geophysical Research, v. 91, p. 6263, doi:10.1029/JB091iB06p06263.

Moucha, R., Forte, A.M., Rowley, D.B., Mitrovica, J.X., Simmons, N.A., and Grand, S.P., 2009, Deep mantle forces and the uplift of the Colorado Plateau: Geophysical Research Letters, v. 36, p. L19310, doi:10.1029/2009GL039778.

Moucha, R., Forte, A.M., Rowley, D.B., Mitrovica, J.X., Simmons, N.A., and Grand, S.P., 2008, Mantle convection and the recent evolution of the Colorado Plateau and the Rio Grande Rift valley: Geology, v. 36, p. 439, doi:10.1130/G24577A.1.

Murray, A.S., and Wintle, A.G., 2000, Luminescence dating of quartz using an improved single-aliquot regenerative-dose protocol: Radiation Measurements, v. 32, p. 57–73, doi:10.1016/S1350-4487(99)00253-X.

Nelson, M.S., Gray, H.J., Johnson, J.A., Rittenour, T.M., Feathers, J.K., and Mahan, S.A., 2015, User Guide for Luminescence Sampling in Archaeological and Geological Contexts: Advances in Archaeological Practice, v. 3, p. 166–177, doi:10.7183/2326-3768.3.2.166.

Niemann, J.D., Gasparini, N.M., Tucker, G.E., and Bras, R.L., 2001, A quantitative evaluation of Playfair's law and its use in testing long-term stream erosion models: Earth Surface Processes and Landforms, v. 26, p. 1317–1332, doi:10.1002/esp.272.

Nishiizumi, K., Imamura, M., Caffee, M.W., Southon, J.R., Finkel, R.C., and McAninch, J., 2007, Absolute calibration of 10Be AMS standards: Nuclear Instruments and Methods in Physics Research Section B: Beam Interactions with Materials and Atoms, v. 258, p. 403–413, doi:10.1016/j.nimb.2007.01.297.

Ouchi, S., 1985, Response of alluvial rivers to slow active tectonic movement: Geological Society of America Bulletin, v. 96, p. 504–515.

Ouimet, W.B., Whipple, K.X., and Granger, D.E., 2009, Beyond threshold hillslopes: Channel adjustment to base-level fall in tectonically active mountain ranges: Geology, v. 37, p. 579–582, doi:10.1130/G30013A.1.

Pavano, F., and Gallen, S.F., 2021, A geomorphic examination of the Calabrian forearc translation: Tectonics, v. 40, doi:10.1029/2020TC006692.

Pazzaglia, F.J., 2013, 9.22 Fluvial Terraces, *in* Treatise on Geomorphology, Elsevier, p. 379–412, doi:10.1016/B978-0-12-374739-6.00248-7.

Pazzaglia, F.J., and Brandon, M.T., 1996, Macrogeomorphic evolution of the post-Triassic Appalachian mountains determined by deconvolution of the offshore basin sedimentary record: Basin Research, v. 8, p. 255–278, doi:10.1046/j.1365-2117.1996.00274.x.

Pazzaglia, F.J., and Gardner, T.W., 1994, Late Cenozoic flexural deformation of the middle U.S. Atlantic passive margin: Journal of Geophysical Research: Solid Earth, v. 99, p. 12143–12157, doi:10.1029/93JB03130.

Pecl, G.T. et al., 2017, Biodiversity redistribution under climate change: Impacts on ecosystems and human well-being: Science, v. 355, p. eaai9214, doi:10.1126/science.aai9214.

Peifer, D., Persano, C., Hurst, M.D., Bishop, P., and Fabel, D., 2020, Growing topography due to contrasting rock types in a tectonically dead landscape: Physical: Geomorphology (including all aspects of fluvial, coastal, aeolian, hillslope and glacial geomorphology) preprint, doi:10.5194/esurf-2020-68.

Pelletier, J., 2009, The impact of snowmelt on the late Cenozoic landscape of the southern Rocky Mountains, USA: GSA Today, v. 19, doi:10.1130/GSATG44A.1.

Perron, J.T., Royden, L., Niemi, N.A., Schildgen, T.F., Van Der Beek, P.A., Sinclair, H.D., and Thiede, R.C., 2013, An integral approach to bedrock river profile analysis: Earth Surface Processes and Landforms, v. 38, p. 570–576, doi:10.1002/esp.3302.

Portenga, E.W., and Bierman, P.R., 2011, Understanding Earth's eroding surface with 10Be: GSA Today, v. 21, p. 4–10, doi:10.1130/G111A.1.

Powers, W.E., 1935, Physiographic History of the Upper Arkansas River Valley and the Royal Gorge, Colorado: The Journal of Geology, v. 43, p. 184–199, doi:10.1086/624287.

Prescott, J.R., and Hutton, J.T., 1994, Cosmic ray contributions to dose rates for luminescence and ESR dating: Large depths and long-term time variations: Radiation Measurements, v. 23, p. 497–500, doi:10.1016/1350-4487(94)90086-8.

Prince, P.S., Spotila, J.A., and Henika, W.S., 2011, Stream capture as driver of transient landscape evolution in a tectonically quiescent setting: Geology, v. 39, p. 823–826, doi:10.1130/G32008.1.

Raymo, M.E., Ruddiman, W.F., and Froelich, P.N., 1988, Influence of late Cenozoic mountain building on ocean geochemical cycles: Geology, v. 16, p. 649–653.

Raynolds, R.G., 2002, Upper Cretaceous and Tertiary stratigraphy of the Denver Basin, Colorado: Rocky Mountain Geology, v. 37, p. 111–134, doi:10.2113/gsrocky.37.2.111.

Rees-Jones, J., 1995, Optical dating of young sediments using fine-grain quartz: Ancient Tl, v. 13, p. 9–14.

Riebe, C.S., and Granger, D.E., 2013, Quantifying effects of deep and near-surface chemical erosion on cosmogenic nuclides in soils, saprolite, and sediment: Earth Surface Processes and Landforms, v. 38, p. 523–533, doi:10.1002/esp.3339.

Riebe, C.S., Kirchner, J.W., Granger, D.E., and Finkel, R.C., 2001, Strong tectonic and weak climatic control of long-term chemical weathering rates: Geology, v. 29, p. 511, doi:10.1130/0091-7613(2001)029<0511:STAWCC>2.0.CO;2.

Riihimaki, C.A., Anderson, R.S., and Safran, E.B., 2007, Impact of rock uplift on rates of late Cenozoic Rocky Mountain river incision: Journal of Geophysical Research, v. 112, p. F03S02, doi:10.1029/2006JF000557.

Riihimaki, C.A., Anderson, R.S., Safran, E.B., Dethier, D.P., Finkel, R.C., and Bierman, P.R., 2006, Longevity and progressive abandonment of the Rocky Flats surface, Front Range, Colorado: Geomorphology, v. 78, p. 265–278, doi:10.1016/j.geomorph.2006.01.035.

Rosenberg, R., Kirby, E., Aslan, A., Karlstrom, K., Heizler, M., and Ouimet, W., 2014, Late Miocene erosion and evolution of topography along the western slope of the Colorado Rockies: Geoshpere, v. 10, p. 641–663, doi:10.1130/GES00989.1.

Rossi, M.W., Whipple, K.X., and Vivoni, E.R., 2016, Precipitation and evapotranspiration controls on daily runoff variability in the contiguous United States and Puerto Rico: Journal of Geophysical Research: Earth Surface, v. 121, p. 128–145, doi:10.1002/2015JF003446.

Royden, L., and Taylor Perron, J., 2013, Solutions of the stream power equation and application to the evolution of river longitudinal profiles: Journal of Geophysical Research: Earth Surface, v. 118, p. 497–518, doi:10.1002/jgrf.20031.

Schildgen, T., Dethier, D.P., Bierman, P., and Caffee, M., 2002, 26Al and 10Be dating of Late Pleistocene and Holocene fill terraces: A record of fluvial deposition and incision, Colorado Front Range: Earth Surface Processes and Landforms, v. 27, p. 773–787, doi:10.1002/esp.352.

Schoenbohm, L.M., Whipple, K.X., Burchfiel, B.C., and Chen, L., 2004, Geomorphic constraints on surface uplift, exhumation, and plateau growth in the Red River region, Yunnan Province, China: Geological Society of America Bulletin, v. 116, p. 895, doi:10.1130/B25364.1.

Schumm, S.A., Dumont, J.F., and Holbrook, J.M., 2002, Active tectonics and alluvial rivers: Cambridge University Press.

Schwanghart, W., and Scherler, D., 2014, Short Communication: TopoToolbox 2 – MATLAB-based software for topographic analysis and modeling in Earth surface sciences: Earth Surface Dynamics, v. 2, p. 1–7, doi:10.5194/esurf-2-1-2014.

Schweinsberg, A.D., Briner, J.P., Licciardi, J.M., Shroba, R.R., and Leonard, E.M., 2020, Cosmogenic 10Be exposure dating of Bull Lake and Pinedale moraine sequences in the upper Arkansas River valley, Colorado Rocky Mountains, USA: Quaternary Research, v. 97, p. 125–139, doi:10.1017/qua.2020.21.

Schweinsberg, A.D., Briner, J.P., Shroba, R.R., Licciardi, J.M., and Leonard, E.M., 2016, Pinedale Glacial History of the Upper Arkansas River Valley: New Moraine Chronologies, Modeling Results and Geologic Mapping: , p. 50.

Scott, G.R., 1977, Reconnaissance geologic map of the Cañon City Quadrangle, Fremont County, Colorado: USGS Miscellaneous Field Studies Map Geological maps.

Scott, G.R., 1972, Reconnaissance geologic map of the Hobson quadrangle, Pueblo and Fremont County, Colorado: USGS.

Scott, G.R., 1960, Subdivision of the Quaternary alluvium east of the Front Range near Denver, Colorado: Geological Society of America Bulletin, v. 71, p. 1541, doi:10.1130/0016-7606(1960)10[1541:SOTQAE]2.0.CO;2.

Scott, G.R., and Lindvall, R.M., 1970, Geology of new occurrences of Pleistocene bisons and peccaries in Colorado: USGS 700, 141–149 p.

Scott, G.R., and Taylor, R.B., 1975, Post-Paleocene Tertiary rocks and Quaternary volcanic ash of the Wet Mountain Valley, Colorado: USGS Professional Paper Professional Paper 868, 1–15 p.

Sharps, J.A., 1976, Geologic map of the Lamar quadrangle, Colorado and Kansas: USGS.

Small, E.E., and Anderson, R.S., 1998, Pleistocene relief production in Laramide mountain ranges, western United States: Geology, v. 26, p. 123–126.

Smith, R.B., 1979, The influence of mountains on the atmosphere, *in* Advances in Geophysics, Elsevier, v. 21, p. 87–230, doi:10.1016/S0065-2687(08)60262-9.

Snyder, N.P., Whipple, K.X., Tucker, G.E., and Merritts, D.J., 2000, Landscape response to tectonic forcing: Digital elevation model analysis of stream profiles in the Mendocino triple junction region, northern California: Geological Society of America Bulletin, v. 112, p. 1250–1263.

Steven, T.A., 1975, Middle Tertiary volcanic field in the Southern Rocky Mountains: Geological Society of America Memoir, v. 144, p. 75–94.

Szabo, B.J., 1980, Results and assessment of uranium-series dating of vertebrate fossils from Quaternary alluviums in Colorado: Arctic and Alpine Research, v. 12, p. 95, doi:10.2307/1550593.

Tao, Z., Li, A., and Fischer, K.M., 2020, Hotspot signatures at the North American passive margin: Geology, v. 49, p. 525–530, doi:10.1130/G47994.1.

Taylor, R.B., 1975, Reconnaissance geologic map of the Cotopaxi 15-minute quadrangle, Fremont and Custer Counties, Colorado: No. 900.

Taylor, R.B., Scott, G.R., Wobus, R.A., and Epis, R.C., 1975a, Reconnaissance geologic map of the Cotopaxi 15-minute quadrangle, Fremont and Custer Counties, Colorado.:

Taylor, R., Scott, G., Wobus, R., and Epis, R., 1975b, Reconnaissance geologic map of the Royal Gorge quadrangle, Fremont and Custer Counties, Colorado: US Geological Survey: Geologic Quadrangle Map I, v. 869.

Thomsen, K.J., Murray, A.S., Jain, M., and Bøtter-Jensen, L., 2008, Laboratory fading rates of various luminescence signals from feldspar-rich sediment extracts: Radiation Measurements, v. 43, p. 1474–1486, doi:10.1016/j.radmeas.2008.06.002.

Trabucco, A., and Zomer, R.J., 2009, Global aridity index (global-aridity) and global potential evapo-transpiration (global-PET) geospatial database.: CGIAR Consortium for Spatial Information, v. 89, p. 1–2.

Tucker, G.E., and van der Beek, P., 2013, A model for post-orogenic development of a mountain range and its foreland: Basin Research, v. 25, p. 241–259, doi:10.1111/j.1365-2117.2012.00559.x.

Tucker, G.E., and Whipple, K.X., 2002, Topographic outcomes predicted by stream erosion models: Sensitivity analysis and intermodel comparison: Journal of Geophysical Research: Solid Earth, v. 107, p. ETG 1-1-ETG 1-16, doi:10.1029/2001JB000162.

Turowski, J.M., Lague, D., Crave, A., and Hovius, N., 2006, Experimental channel response to tectonic uplift: EXPERIMENTAL CHANNEL RESPONSE: Journal of Geophysical Research: Earth Surface, v. 111, p. n/a-n/a, doi:10.1029/2005JF000306.

Tuyl, F.M.V., and Lovering, T.S., 1935, Physiographic development of the Front Range: Bulletin of the Geological Society of America, v. 46, p. 1291–1439.

Wallinga, J., Murray, A., and Wintle, A., 2000, The single-aliquot regenerative-dose (SAR) protocol applied to coarse-grain feldspar: Radiation Measurements, v. 32, p. 529–533, doi:10.1016/S1350-4487(00)00091-3.

Watts, A.B., 2001, Isostasy and flexure of the lithosphere: Cambridge ; New York, Cambridge University Press, 458 p.

Wegmann, K.W., and Pazzaglia, F.J., 2009, Late Quaternary fluvial terraces of the Romagna and Marche Apennines, Italy: Climatic, lithologic, and tectonic controls on terrace genesis in an active orogen: Quaternary Science Reviews, v. 28, p. 137–165, doi:10.1016/j.quascirev.2008.10.006.

Whipple, K.X., 2004, Bedrock rivers and the geomorphology of active orogens: Annual Review of Earth and Planetary Sciences, v. 32, p. 151–185, doi:10.1146/annurev.earth.32.101802.120356.

Whipple, K.X., Forte, A.M., DiBiase, R.A., Gasparini, N.M., and Ouimet, W.B., 2017, Timescales of landscape response to divide migration and drainage capture: Implications for the role of divide mobility in landscape evolution: Landscape Response to Divide Mobility: Journal of Geophysical Research: Earth Surface, v. 122, p. 248–273, doi:10.1002/2016JF003973.

Whipple, K.X., Hancock, G.S., and Anderson, R.S., 2000, River incision into bedrock: Mechanics and relative efficacy of plucking, abrasion and cavitation: Geological Society of America Bulletin, p. 18.

Whipple, K.X., Kirby, E., and Brocklehurst, S.H., 1999, Geomorphic limits to climate-induced increases in topographic relief: Nature, v. 401, p. 39–43, doi:10.1038/43375.

Whipple, K.X., and Tucker, G.E., 1999, Dynamics of the stream-power river incision model: Implications for height limits of mountain ranges, landscape response timescales, and research needs: Journal of Geophysical Research: Solid Earth, v. 104, p. 17661–17674, doi:10.1029/1999JB900120.

Widmann, B.L., 1997a, Fault number 2327, Ute Pass fault zone: USGS Quaternary fault and fold database of the United States: U.S. Geological Survey.

Widmann, B.L., 1997b, Fault number 2329, Goodpasture fault: USGS Quaternary fault and fold database of the United States: U.S. Geological Survey.

Willett, S.D., 1999, Orogeny and orography: The effects of erosion on the structure of mountain belts: Journal of Geophysical Research: Solid Earth, v. 104, p. 28957–28981, doi:10.1029/1999JB900248.

Willett, S.D., McCoy, S.W., and Beeson, H.W., 2018, Transience of the North American High Plains landscape and its impact on surface water: Nature, v. 561, p. 528–532, doi:10.1038/s41586-018-0532-1.

Willett, S.D., McCoy, S.W., Perron, J.T., Goren, L., and Chen, C.-Y., 2014, Dynamic Reorganization of River Basins: Science, v. 343, p. 1248765–1248765, doi:10.1126/science.1248765.

Wintle, A.G., 1997, Luminescence dating: laboratory procedures and protocols: Radiation Measurements, v. 27, p. 769–817, doi:10.1016/S1350-4487(97)00220-5.

Wobus, R.A., Epis, R.C., and Scott, G.R., 1979, Geologic map of the Cover Mountain quadrangle, Fremont, Park, and Teller counties, Colorado.:

Wobus, C.W., Tucker, G.E., and Anderson, R.S., 2010, Does climate change create distinctive patterns of landscape incision? Journal of Geophysical Research, v. 115, p. F04008, doi:10.1029/2009JF001562.

Wobus, C., Whipple, K.X., Kirby, E., Snyder, N., Johnson, J., Spyropolou, K., Crosby, B., and Sheehan, D., 2006, Tectonics from topography: Procedures, promise, and pitfalls, *in* Tectonics, Climate, and Landscape Evolution, Geological Society of America, doi:10.1130/2006.2398(04).

Yanites, B.J., Tucker, G.E., and Anderson, R.S., 2009, Numerical and analytical models of cosmogenic radionuclide dynamics in landslide-dominated drainage basins: Journal of Geophysical Research, v. 114, p. F01007, doi:10.1029/2008JF001088.

Young, N.E., Briner, J.P., Leonard, E.M., Licciardi, J.M., and Lee, K., 2011, Assessing climatic and nonclimatic forcing of Pinedale glaciation and deglaciation in the western United States: Geology, v. 39, p. 171–174, doi:10.1130/G31527.1.

Zaprowski, B.J., Evenson, E.B., Pazzaglia, F.J., and Epstein, J.B., 2001, Knickzone propagation in the Black Hills and northern High Plains: A different perspective on the late Cenozoic exhumation of the Laramide Rocky Mountains: Geology, v. 29, p. 4.

Zaprowski, B.J., Pazzaglia, F.J., and Evenson, E.B., 2005, Climatic influences on profile concavity and river incision: Journal of Geophysical Research, v. 110, p. F03004, doi:10.1029/2004JF000138.

Zhu, Y., Dortch, J.M., Massey, M.A., Haneberg, W.C., and Curl, D., 2021, An intelligent swath tool to characterize complex topographic features: Theory and application in the Teton Range, Licking River, and Olympus Mons: Geomorphology, v. 387, p. 107778, doi:10.1016/j.geomorph.2021.107778.

Appendices

Appendix A

Digital topographic analysis

We delineated the eastern Rockies fluvial network based on linear relationships between the log of drainage slope, S, and the log of upstream drainage area, A (Figure C1; Snyder, 2000; Wobus et al., 2006; Kirby and Whipple, 2012). This analysis suggests that the transition between fluvially- and colluvially-dominate channels occur at a drainage area of ~3e^4 m^2 (Figure C1). To ensure that we only work in the fluvially-dominated portion of the channels and follow the detachment-limited stream power incision model assumptions (i.e., bedrock channels are not affected by hillslope and sediment processes; e.g., Snyder, 2000; Kirby and Whipple, 2012), we conservatively used a drainage area threshold ≥ 10^6 m^2 to define drainage networks in the eastern Rockies. We calculated the regional-scale concavity, θ_{ref}, in the eastern Rockies by taking the average of two independent TopoToolbox functions - a Bayesian optimization function 'mnoptim' and a variance minimization function 'mnoptimvar' (Figure A2). We used this empirically-derived θ_{ref} to calculate χ across the eastern Rockies drainage network, evaluate k_{sn} for binned segments along it, and interpolate k_{sn} for the entire eastern Rockies region (Figure 1.3C, main text).

Basin-wide linear inversion

We evaluated the relative base level fall history of each basin using a linear inversion approach. We discretized equation 7 (see main text) to solve for the average basin k_{sn} for a discrete $\Delta\chi$ interval, such that:

$$z_j = 1k_{sn_1}\Delta\chi_1 + 2k_{sn_2}\Delta\chi_2 + \cdots + qk_{sn_{j-2}}\Delta\chi_{j-2} + qk_{sn_{j-1}}\Delta\chi_{j-1} \quad \text{(A1).}$$

Equation A1 can be written as a matrix forward problem:

$$Ak_{sn} = z \quad \text{(A2),}$$

where A is an n by q sized matrix, where n is the number of stream nodes, and q is the number of discrete domains:

$$A = \begin{bmatrix} \Delta\chi_1 & \cdots & q\Delta\chi_1 \\ \vdots & \ddots & \vdots \\ \Delta\chi_n & \cdots & q\Delta\chi_n \end{bmatrix} \quad \text{(A3).}$$

The Tikhonov regularization for Equation A2 is:

$$k_{sn} = k_{sn}{}^{pri} + (A^T A + \Gamma^2 I)^{-1} A^T (z - Ak_{sn}{}^{pri}) \quad \text{(A4),}$$

where ${k_{sn}}^{pri}$ is a prior guess for k_{sn}, Γ is a dampening coefficient that determines the smoothness imposed on the solution, and I is the $q\ X\ q$ identity matrix. We used these equations to conduct a linear inversion of χ-z data for each of the basins in the eastern Rockies and compared them with the tributary trunk channel χ-plots and knickpoints (Figure A3). Under the assumption that K is spatially and temporally uniform and rock uplift is spatially uniform, changes in base level fall rate will translate upstream at the same rate in χ-transformed distance space. In this case, the results of linear inversion of χ-z data can be interpreted as a test for genetically-related knickpoints, analogous to applications of the knickpoint celerity model (e.g., Crosby and Whipple, 2006; Berlin and Anderson, 2007; Gallen et al., 2013; Miller et al., 2013). However, in the case of the linear inversion, all data in the fluvial network is analyzed rather than just hand-selected knickpoint data, and related knickpoints can be identified as spikes or steps in χ-binned k_{sn} plots. If it is assumed that the slope exponent in the stream power model, n, is equal to 1, this analysis reflects the relative history of base level fall assuming block uplift (cf. Goren et al., 2014). If the erodibility constant can be calibrated, the χ-binned k_{sn} plots can be converted to base level fall or rock uplift rate histories (e.g., Goren et al., 2014; Gallen, 2018).

Terrace analysis

To get a first identification of the presented surfaces in the western High Plains, we conducted 28 cross-sections across the Arkansas River Valley at 1 km intervals from Canon City, CO downstream to Pueblo, CO using Google Earth imagery. We measured forty-five terraces strath elevations and alluvial fills above these straths using a TruPulse 360 Rangefinder in the field (Table A1). We verified the downstream terrace correlations by subdividing the LiDAR elevation data to equal increments of 10m of elevation difference from the modern Arkansas River. We refined our terrace correlations by conducting a LiDAR hypsometry (Figure 1.7, main text). For the hypsometry, we first removed “non-flat” areas in the LiDAR data using slope and curvature thresholds of 5° and ± 0.005, respectively, as well as mapped Holocene terraces along the Arkansas valley. We projected the mapped treads polygon edges to the Arkansas River Valley and performed power law (Figure 1.7, main text) and linear (Figure A5) regressions to evaluate the estimated total incisions for each terrace level from the modern Arkansas River.

Flexural Analysis

We conducted a 2D flexural response model to differential erosion beneath the estimated Rocky Flats (~1.3-2 Ma) paleo-surface along the western High Plains (Figure 1.10, main text; Figure A6). For the flexural model, we used a continuous two-dimensional elastic layer over an inviscid half-space (Watts, 2001):

$$D\frac{d^4w}{dx^4} + (\rho_m - \rho_c)gw = q \tag{A5}$$

$$D = \frac{ET_e{}^3}{(1 - v)^2} \tag{A6}$$

where D is the lithospheric rigidity, w is the vertical deflection of the plate, ρ_m is the mantle density, ρ_c, is the crust/infill density, g, is the acceleration due to gravity (9.81 m s^{-2}), q, is the applied surface load based on the inferred eroded volume from the paleo-surface of the Rocky Flats, T_e, is the effective elastic thickness of the lithosphere, E, is the Young's modulus, and v, is the Poisson's ratio. To calculate the flexural deflection, w, we applied elastic thicknesses, $T_e = 5 - 15\ km$; mantle density, $\rho_m = 3300\ kg/m^3$; crust/infill density, $\rho_c = 2500\ kg/m^3$; Young's modulus, $E = 10^{11}\ Pa$; and Poisson's ratio, $v = 0.25$, following previous geophysical studies in the region (Lazear et al., 2013; Hansen et al., 2013). All calculations assumed spatially uniform lithospheric rigidity and were solved in the spectral domain. Forward and inverse fast Fourier transforms were used to move between the spatial and spectral domains and generate maps of two-dimensional surface deflections (Figure A6).

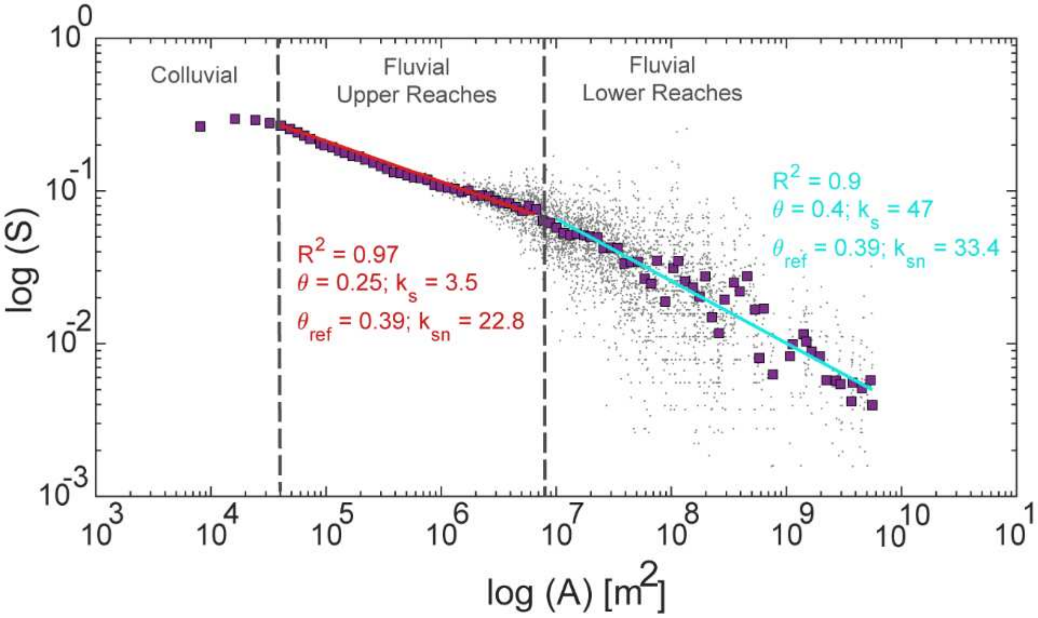

Figure A1 Slope-Drainage Area plot for 100 m streamwise distance increments along the eastern Rockies drainage network (grey points) overlain by log-binned averages of the raw data (purple squares). A transition from colluvial to a fluvial regime is noticed at drainage areas of ~3e^4 m^2. In this study, only basins that drain > 1e6 m^2 were analyzed. Also marked is the transition between upper reaches that drain 1e^5 - 1e^7 m^2 (red line) and lower reaches that drain 1e^7 - 1e^{10} m^2 (cyan line), with relative k_s, θ, k_{sn} (for $\theta_{ref} = 0.39$) and R^2.

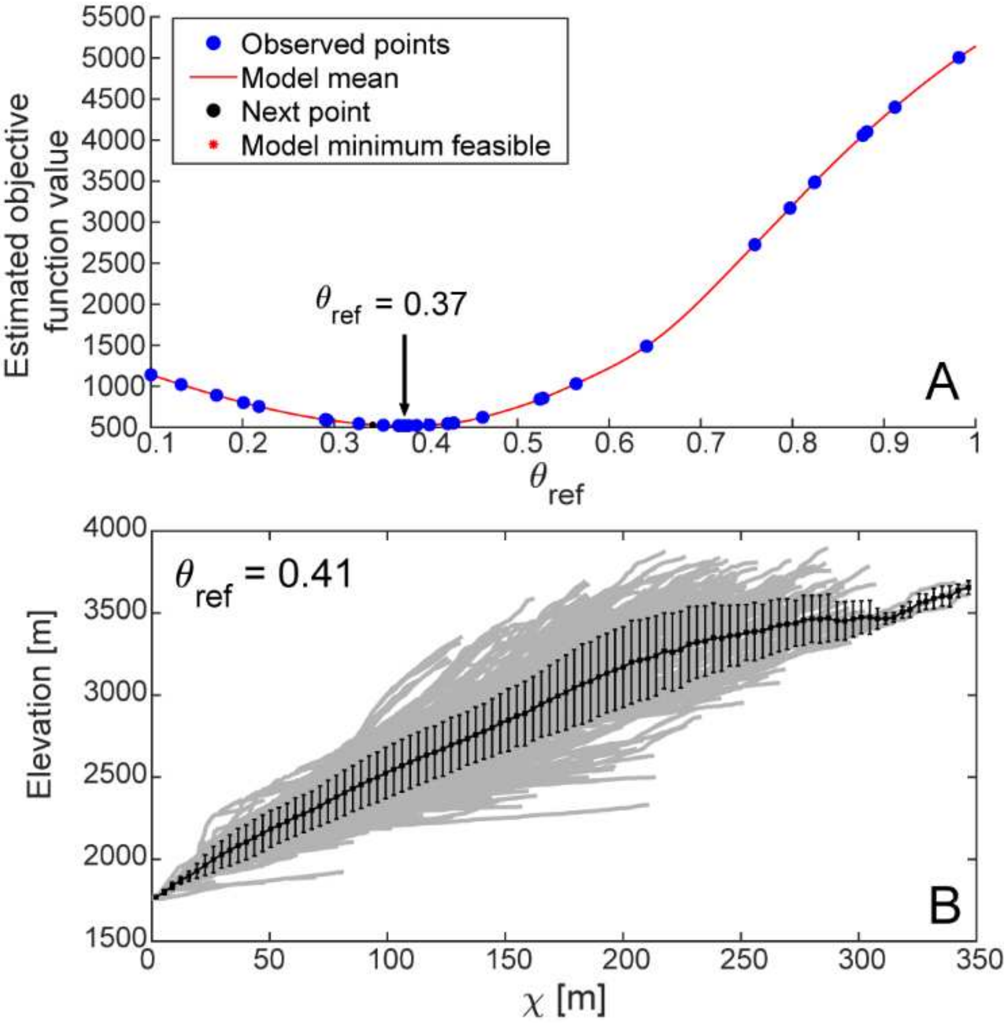

Figure A2 The two independent methods used to calculate θ_{ref} for the eastern Rockies drainage network (TopoToolbox v2; Schwanghart and Scherler, 2014): ***(A)*** *Bayesian optimization;* ***(B)*** *variance minimization. The average value from these two methods is ~0.39.*

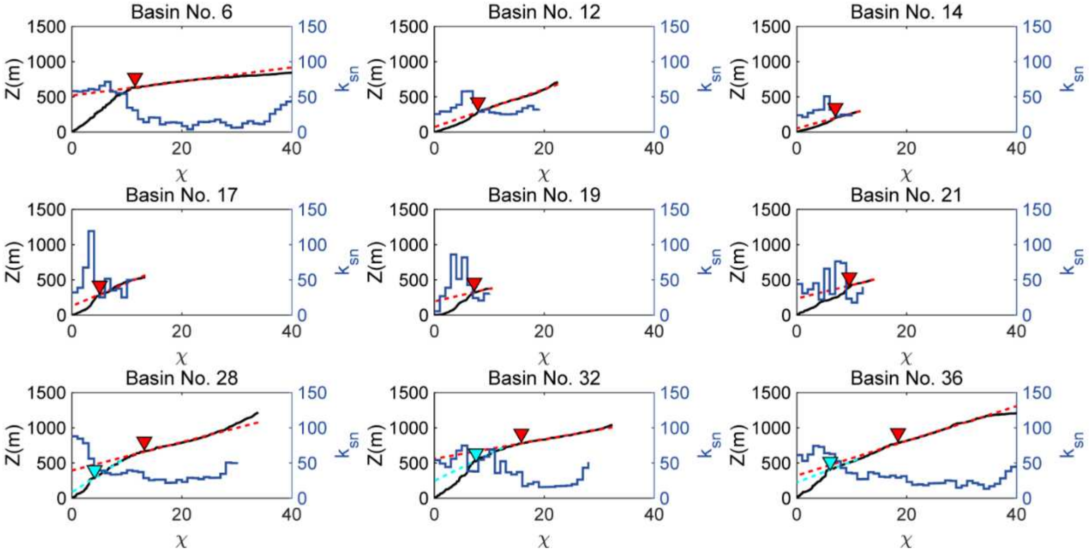

Figure A3 Full river profile analysis for the analyzed basins in the eastern Rockies drainage network (Figure 1.1, Figure 1.3B, Figure 1.5 in main text). Tributary trunks (black lines) and knickpoints (reversed triangles, see legend in Figure 1.4, main text) are plotted against k_{sn} *calculated from the basin-wide linear inversion (blue lines), which is equivalent to the relative uplift/base level fall history. Also marked are calculated relict topographies regressions from reaches above the knickpoints (dashed lines).*

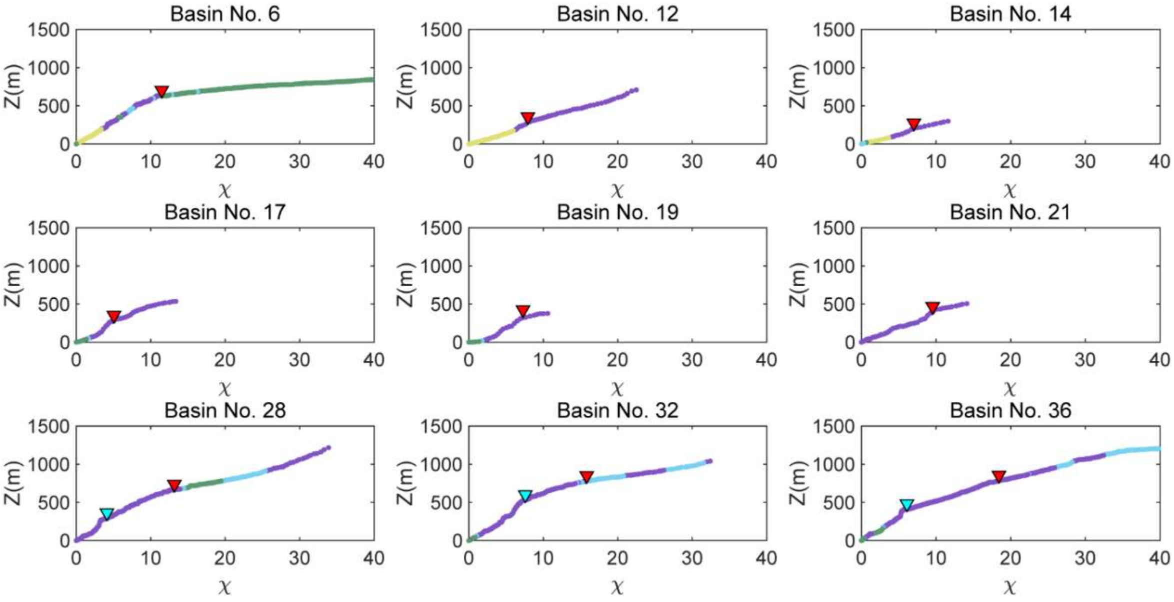

Figure A4 Same river profiles as in Figure A3, colored by main lithologies beneath the river flow path (e.g., Figure 1.33A main text). Generally, the knickpoints do not show correlations with lithological changes.

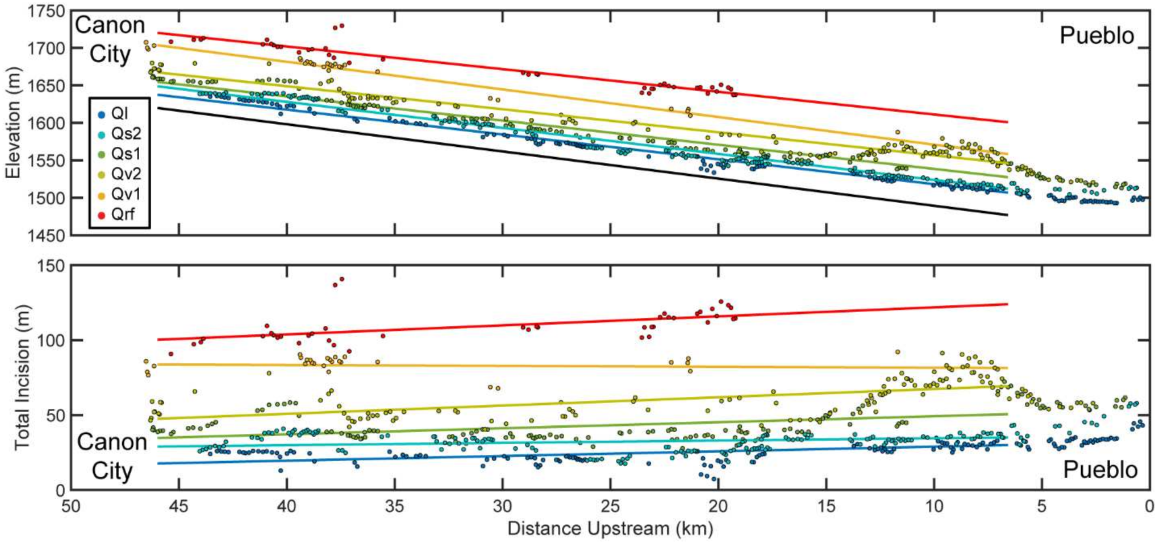

Figure A5 ***(Top)*** *Linear regressions through projected tread river-facing edges points to the Arkansas River valley line (cf. Figure 1.7, main text).* ***(Bottom)*** *Total incision calculated from the linear regressions to the modern Arkansas River (cf. Figure 1.7, main text). Like the power law regressions (Figure 1.7), total incision increases downstream along the Arkansas River in a reversed fanning pattern.*

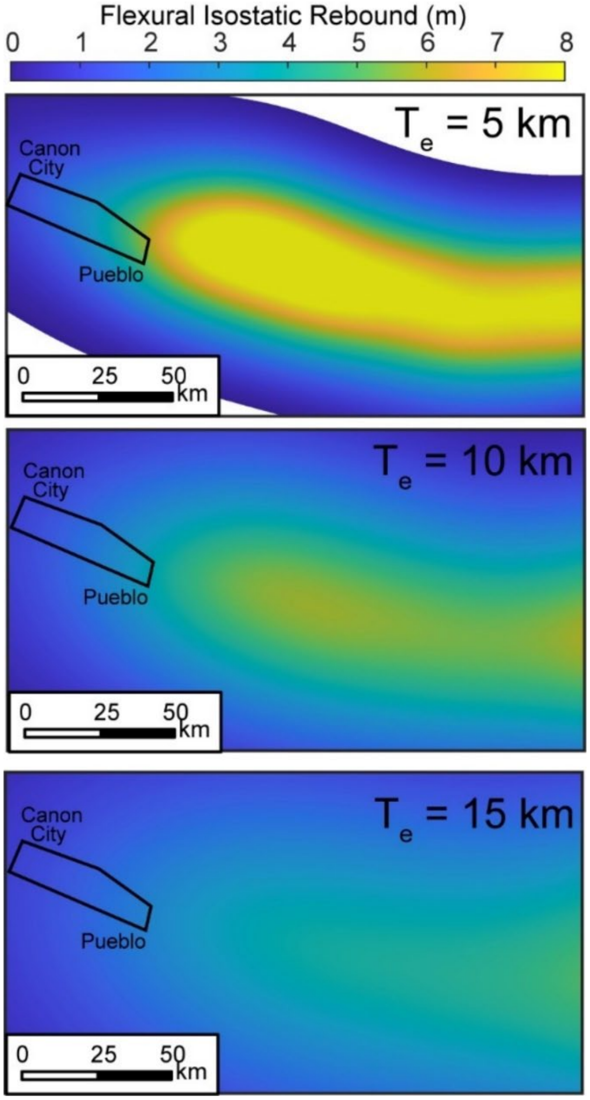

Figure A6 Flexural response of the Arkansas River valley across the western High Plains under T_e *= 5, 10, and 15 km. The flexural load is calculated from an inferred eroded volume based on remnants of the oldest terrace in the western High Plains, the Rocky Flats (~1.3-2 Ma) (Figure 1.1, Figure 1.8A main text).*

Table A1 Summary of terrace strath elevations and alluvial fill thicknesses as measured in the field (Figure 7, main text). Terrace names are after Scott et al. (1972, 1977).

Terrace Name	Latitude (°)	Longtitude (°)	Elevation (m)	Height from AR/Other (m)	Alluvial Fill (m)
Qs2	38.39693333	-105.14045	1609	16 from tributary	6.2
Ql	38.4374	-105.20675	1575	16.4 from trail	3.5
Ql	38.39166667	-105.0675667	1515	23	0.1
Qs2	38.38551667	-105.0698667	1528	25	1.7
Ql	38.38601667	-105.00505	1542	22	3
Qs1	38.38101667	-104.9689667	1557	20 from creek	2.8
Qv2	38.37165	-104.9535	1578	25 from Qs strath	
Qs2	38.40051667	-105.1157833	1590	30	4
Qs2	38.3842	-105.1157167	1584	16 from HW 115	3
Qv2	38.40416667	-105.1642833	1586		5
Qv2	38.40276667	-105.1649	1565		2.5
Qv1	38.42846667	-105.2534333	1636		
Qs2	38.43146667	-105.2521	1619	50m below Qrf above	3
Ql	38.4281	-105.19165	1596	21	
Qs2	38.38683333	-104.9929667	1555	26	
Qv2	38.38683333	-104.9929667	1555	54	
Qv1	38.36888889	-104.9425	1595		3
Qs1	38.37138889	-104.9491667	1569		2.8
Qs1	38.37055556	-104.9533333	1571		3
Qs2	38.375	-104.9622222	1547		4
Qs2	38.37083333	-104.9633333	1548		4
Qs2	38.3725	-104.9594444	1552		4
Qs1	38.38194444	-104.9766667	1564		3
Qs1	38.38611111	-105.0297222	1578		6
Qs1	38.38444444	-105.0294444	1581		6
Qv2	38.3825	-105.0511111	1600		1
Qs1	38.38444444	-105.0519444	1583		1
Qs1	38.40416667	-105.1461111	1609		10

Appendix B

Basin average erosion rates

Fluvial sand samples for basin average erosion rate analysis were collected in twelve basin outlets that confluence with the Arkansas and Poudre rivers (Table B1). These samples were physically separated and chemical washed following the techniques described by Kohl and Nishiizumi (1992) at the Critical Zone and Tectonic Geomorphology (CaT) lab at Colorado State University to obtain purified quartz grains for further analysis. ~20.3-43.3 g purified quartz were processed and analyzed at PRIME lab at Purdue University. These analyses included quartz purity testing, ^{9}Be and ^{10}Be extraction, and accelerator mass spectrometry (AMS) analysis on beryllium nuclides. The purified quartz mass used for each sample was determined by Al concentration. One process blank was prepared with each batch of eight samples. Each quartz sample was dissolved in 1:5 HNO_3/HF after adding ~0.25 mg of ^{9}Be carrier. Fluorides were removed by adding 1 ml concentrated H_2SO_4. The remaining solution was added to NaOH to remove iron, titanium, and other elements at ~pH 14. Beryllium was extracted by cation/anion exchange columns and precipitated as beryllium hydroxide ($Be(OH)_2$). The precipitate was converted to beryllium oxide (BeO) by heating the covered quartz crucibles over a propane flame for 60 seconds. The BeO powder of each sample was mixed with niobium and packed in stainless steel holder. Isotope ratios of $^{10}Be/^{9}Be$ were measured by AMS against standard 07KNSTD (Table B2; Nishiizumi et al., 2007). ^{10}Be concentrations for each sample were converted to erosion rates using the CRONUS algorithm (Balco et al., 2008) assuming no shielding (DiBiase, 2018) and an average density of 2.65 g/cm^3, following previous basin average erosion rate calculations near Boulder, CO by Dethier et al. (2014) (Table B1, Table B2).

OSL/IRSL on fluvial terraces

Seven samples were processed and analyzed at Utah State University Luminescence Laboratory in North Logan, Utah for luminescence dating (Table B3, B4). Two of the samples were dated using optically stimulated luminescence (OSL) dating of quartz sand and six samples were dated using infrared stimulated luminescence (IRSL) dating of feldspathic sand (Wintle, 1997). The choice between OSL and IRSL was related to the assumed age of the samples (Table B4), high dose rate and low saturation levels of the quartz, which lead to more favorable application of IRSL in the lower terrace samples. Samples were opened under dim amber light (~590 nm) and potentially light-exposed material from the outer ends of tubes was removed and discarded prior to further processing. The remaining sediment was wet sieved to a target grain size range between 125 and 212 µm. Target sediment was treated with 10% hydrochloric acid and hydrogen peroxide to dissolve carbonates and remove organic material, respectively. Feldspar and quartz mineral grains were separated from heavy minerals using sequential 2.7 g/cm3 and 2.58 g/cm3 density sodium polytungstate solutions and dried at room temperature (Wintle, 1997). Quartz grains for OSL dating were purified and etched with 48% HF over three 30-minute treatments, followed by 38% HCl rinse.

Samples for dose-rate determination were collected from a 30 cm diameter area surrounding the sample tube. Sediments were homogenized and representative samples were analyzed for radioisotope concentration using ICP-MS and ICP-AES techniques. Pebble and small cobble fractions were crushed analyzed separately and their contribution to the total dose rate tallied. Elemental concentrations of U, Th, Rb and K were converted to dose rate following the conversion factors of Guérin et al. (2011) and beta attenuation values of Brennan (2003). For the IRSL ages, the beta dose included contribution from 12.5% internal potassium (Huntley and Baril, 1997) and 400 ppm Rb (Huntley and Hancock, 2001) and an a-value of 0.086 (Rees-Jones, 1995). Contribution of cosmic radiation to the dose rate was calculated using sample depth, elevation and latitude/longitude following (Prescott and Hutton, 1994). Total dose rates were calculated based on water content, radioisotope concentrations, and cosmic contribution (Adamiec and Aitken, 1998).

Luminescence measurements on potassium feldspar followed the latest single-aliquot regenerative-dose (SAR) procedures for potassium feldspar (Wallinga et al., 2000) and include post-IR IRSL (pIR IRSL) at 250°C (Thomsen et al., 2008; Buylaert et al., 2009). OSL ages followed the SAR procedure for quartz (Murray and Wintle, 2000). Both mineral fractions were analyzed from 1-mm aliquots (~20-50 grains per disk). Measurements were performed on Risø TL/OSL Model DA-20 readers with infrared light-emitting diodes (LEDs) (870±40 nm) and blue-green diodes (470±30 nm). The IRSL signal was measured through a blue filter pack of 2-mm and 4-mm thick filters (BG-39 and Corning 7-39, respectively) over 100 seconds (250 channels) at 50°C with LED diodes at 85% power (~120 mW/cm2). OSL signals were detected through 7.5-mm UV filters (U-340) over 40 seconds (250 channels) at 125ºC with LED diodes at 90% power (36-45 mW/cm2). Instrumental dose rates were 0.10-0.11 Gy/sec from decaying 90Sr beta sources (Bøtter-Jensen et al., 2003). Dose response curves were fit to saturating-exponential and saturating-exponential plus linear fits to calculate equivalent dose (DE) values.

The IRSL ages were calculated by correcting individual DE measurements for fading (loss of signal with time, g2days %/decade) using the method of Auclair et al. (2003) and the age correction model of Huntley and Lamothe (2001). OSL DE and IRSL age values were calculated using the Central Age Model (CAM) of Galbraith and Roberts (2012). Aliquots were rejected if recycled (repeated) doses were >10% of unity, produced >10% of signal in the zero-dose step (recuperation) or if they had a natural DE value greater than the highest regenerative dose given. Errors on DE are reported at 2-sigma standard error and include errors related to instrument calibration, dose rate and equivalent dose calculations, and were calculated in quadrature using the methods of Aitken and Alldred (1972) and Guérin et al. (2011).

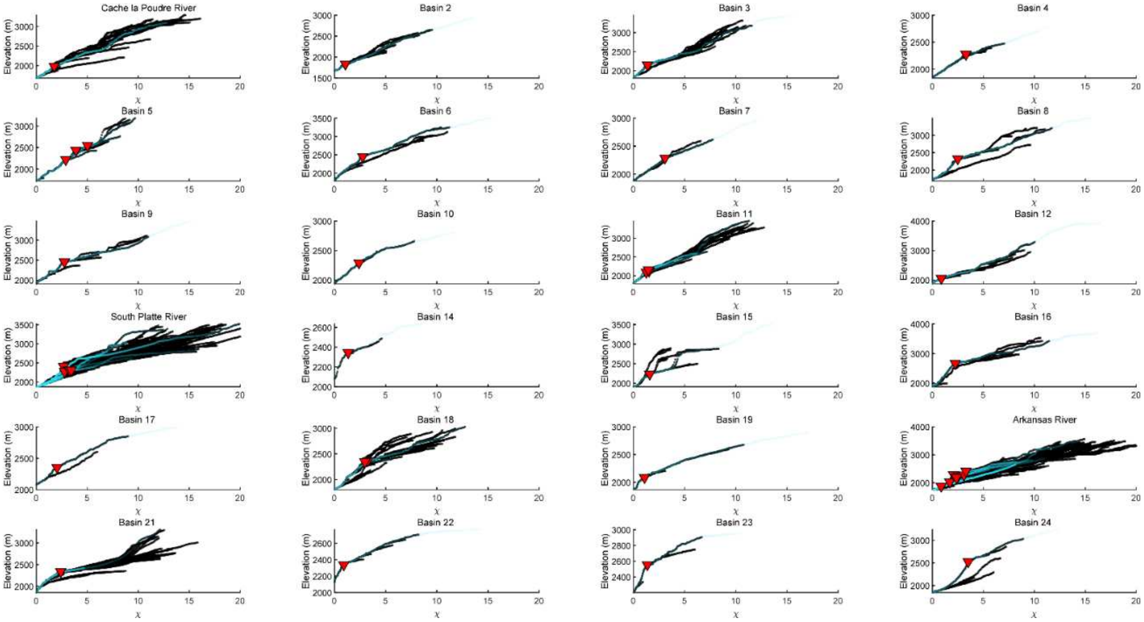

Figure B1 Full river profile analysis of the 24 delineated basins (Figure 1A in main text) in χ-z space. The analyzed rivers (cyan) are plotted on top of the full drainage network (black). Slope-break normal knickpoints (red inverted triangles) are marked. Basin numbers are based on their outlets at the Colorado Rockies-High Plains boundary from north to south.

Table B1 Calculated basin average erosion rates from the new and existing (Dethier et al., 2014) data across the Colorado Rocky Mountains as shown in Figure 1 in the main text.

Sample	Basin outlet coordinates		Drainage area (km^2)	Basin elevation (m)		P muons (at g^-1 yr^-1)	P spallation	Erosion rate (mm/yr)	Erosion rate uncertainty (mm/yr)
	Latitude	Longitude		Outlet	Headwaters				
DC-01-03	39.86	-105.35	11.28	2317	3198	0.18	29.22	1.38E-02	1.22E-03
DC-01-04	39.76	-105.43	9.81	2218	3053	0.17	27.06	1.72E-02	1.53E-03
DC-01-05	39.74	-105.33	16.60	2072	3039	0.17	24.87	1.63E-02	1.45E-03
DC-01-06	39.96	-105.40	10.13	2364	2708	0.17	25.50	2.55E-02	2.18E-03
DC-01-09	40.16	-105.47	13.61	2440	3222	0.18	30.68	1.50E-02	1.30E-03
DC-01-16	40.69	-105.35	39.52	1820	2789	0.16	22.72	1.68E-02	1.45E-03
ESL1-UP	38.60	-105.94	21.49	2694	3338	0.19	32.23	2.06E-02	1.74E-03
ESL1-Down	38.56	-105.99	29.76	2293	3338	0.18	30.51	2.75E-02	2.32E-03
EWS	38.47	-105.86	544.13	2065	3478	0.18	30.63	4.06E-02	3.41E-03
ECR	38.41	-105.64	183.29	1980	3563	0.18	28.59	3.31E-02	2.78E-03
EFP	38.45	-105.49	23.82	1847	2589	0.16	21.26	1.57E-02	1.32E-03
ERGN	38.53	-105.39	369.19	1881	3546	0.18	28.23	2.26E-02	1.90E-03
CC-0319-02	38.51	-105.11	110.88	1814	3286	0.17	25.84	2.21E-02	1.86E-03
CC-0319-03	38.58	-105.01	290.80	1875	4299	0.19	34.56	3.09E-02	2.61E-03
PO-2	40.70	-105.44	89.04	1999	3310	0.17	25.99	1.65E-02	1.42E-03
PO-7	40.69	-105.35	39.58	1803	2789	0.16	22.71	1.71E-02	1.46E-03
PO-9	40.69	-105.31	56.20	1755	2473	0.15	20.27	1.57E-02	1.33E-03
PO-15	40.70	-105.58	22.19	2222	3300	0.18	29.59	2.25E-02	1.90E-03

Table B2 Beryllium mass spectrometer data of the new basin average erosion rate samples along the Poudre and Arkansas rivers (Figure 1 in main text)

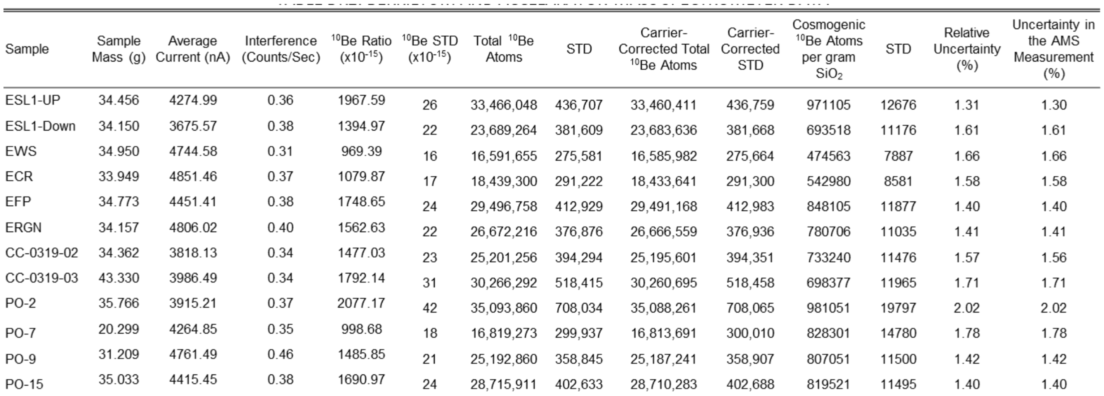

Sample	Sample Mass (g)	Average Current (nA)	Interference (Counts/Sec)	^{10}Be Ratio ($x10^{-15}$)	^{10}Be STD ($x10^{-15}$)	Total ^{10}Be Atoms	STD	Carrier-Corrected Total ^{10}Be Atoms	Carrier-Corrected STD	Cosmogenic ^{10}Be Atoms per gram SiO_2	STD	Relative Uncertainty (%)	Uncertainty in the AMS Measurement (%)
ESL1-UP	34.456	4274.99	0.36	1967.59	26	33,466,048	436,707	33,460,411	436,759	971105	12676	1.31	1.30
ESL1-Down	34.150	3675.57	0.38	1394.97	22	23,689,264	381,609	23,683,636	381,668	693518	11176	1.61	1.61
EWS	34.950	4744.58	0.31	969.39	16	16,591,655	275,581	16,585,982	275,664	474563	7887	1.66	1.66
ECR	33.949	4851.46	0.37	1079.87	17	18,439,300	291,222	18,433,641	291,300	542980	8581	1.58	1.58
EFP	34.773	4451.41	0.38	1748.65	24	29,496,758	412,929	29,491,168	412,983	848105	11877	1.40	1.40
ERGN	34.157	4806.02	0.40	1562.63	22	26,672,216	376,876	26,666,559	376,936	780706	11035	1.41	1.41
CC-0319-02	34.362	3818.13	0.34	1477.03	23	25,201,256	394,294	25,195,601	394,351	733240	11476	1.57	1.56
CC-0319-03	43.330	3986.49	0.34	1792.14	31	30,266,292	518,415	30,260,695	518,458	698377	11965	1.71	1.71
PO-2	35.766	3915.21	0.37	2077.17	42	35,093,860	708,034	35,088,261	708,065	981051	19797	2.02	2.02
PO-7	20.299	4264.85	0.35	998.68	18	16,819,273	299,937	16,813,691	300,010	828301	14780	1.78	1.78
PO-9	31.209	4761.49	0.46	1485.85	21	25,192,860	358,845	25,187,241	358,907	807051	11500	1.42	1.42
PO-15	35.033	4415.45	0.38	1690.97	24	28,715,911	402,633	28,710,283	402,688	819521	11495	1.40	1.40

Table B3 Terrace data and calculated local incision rates from new and existing (Schildgen et al., 2002; Dethier et al., 2014) terrace geochronology across the Colorado Rocky Mountains as shown in Figure 1 in the main text.

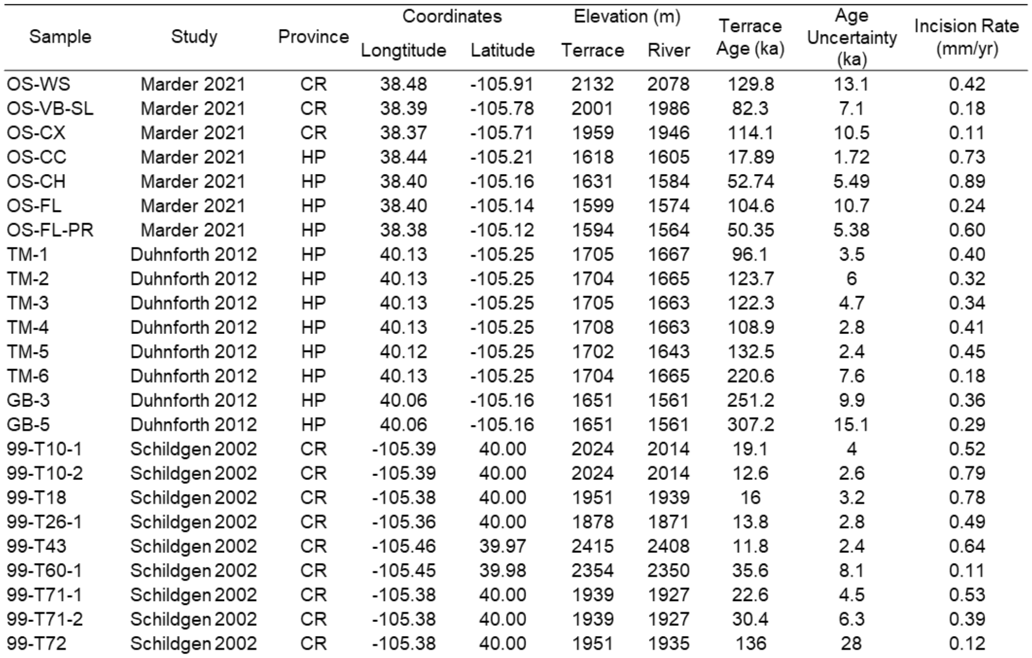

Sample	Study	Province	Coordinates		Elevation (m)		Terrace Age (ka)	Age Uncertainty (ka)	Incision Rate (mm/yr)
			Longtitude	Latitude	Terrace	River			
OS-WS	Marder 2021	CR	38.48	-105.91	2132	2078	129.8	13.1	0.42
OS-VB-SL	Marder 2021	CR	38.39	-105.78	2001	1986	82.3	7.1	0.18
OS-CX	Marder 2021	CR	38.37	-105.71	1959	1946	114.1	10.5	0.11
OS-CC	Marder 2021	HP	38.44	-105.21	1618	1605	17.89	1.72	0.73
OS-CH	Marder 2021	HP	38.40	-105.16	1631	1584	52.74	5.49	0.89
OS-FL	Marder 2021	HP	38.40	-105.14	1599	1574	104.6	10.7	0.24
OS-FL-PR	Marder 2021	HP	38.38	-105.12	1594	1564	50.35	5.38	0.60
TM-1	Duhnforth 2012	HP	40.13	-105.25	1705	1667	96.1	3.5	0.40
TM-2	Duhnforth 2012	HP	40.13	-105.25	1704	1665	123.7	6	0.32
TM-3	Duhnforth 2012	HP	40.13	-105.25	1705	1663	122.3	4.7	0.34
TM-4	Duhnforth 2012	HP	40.13	-105.25	1708	1663	108.9	2.8	0.41
TM-5	Duhnforth 2012	HP	40.12	-105.25	1702	1643	132.5	2.4	0.45
TM-6	Duhnforth 2012	HP	40.13	-105.25	1704	1665	220.6	7.6	0.18
GB-3	Duhnforth 2012	HP	40.06	-105.16	1651	1561	251.2	9.9	0.36
GB-5	Duhnforth 2012	HP	40.06	-105.16	1651	1561	307.2	15.1	0.29
99-T10-1	Schildgen 2002	CR	-105.39	40.00	2024	2014	19.1	4	0.52
99-T10-2	Schildgen 2002	CR	-105.39	40.00	2024	2014	12.6	2.6	0.79
99-T18	Schildgen 2002	CR	-105.38	40.00	1951	1939	16	3.2	0.78
99-T26-1	Schildgen 2002	CR	-105.36	40.00	1878	1871	13.8	2.8	0.49
99-T43	Schildgen 2002	CR	-105.46	39.97	2415	2408	11.8	2.4	0.64
99-T60-1	Schildgen 2002	CR	-105.45	39.98	2354	2350	35.6	8.1	0.11
99-T71-1	Schildgen 2002	CR	-105.38	40.00	1939	1927	22.6	4.5	0.53
99-T71-2	Schildgen 2002	CR	-105.38	40.00	1939	1927	30.4	6.3	0.39
99-T72	Schildgen 2002	CR	-105.38	40.00	1951	1935	136	28	0.12

Table B4 Optically stimulated luminescence (OSL) and infrared stimulated luminescence (IRSL) data for the samples collected in different fluvial terraces along the Arkansas River (Figure 1 in main text).

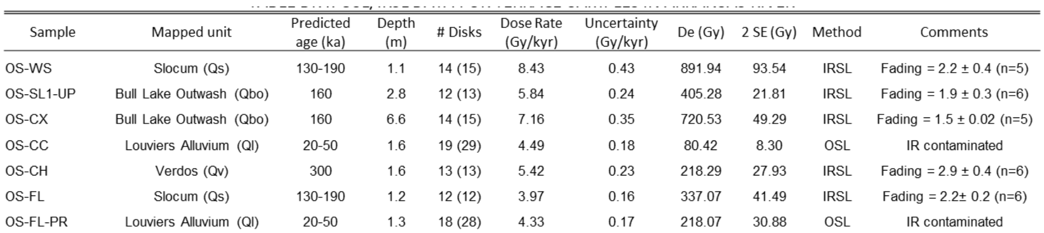

Sample	Mapped unit	Predicted age (ka)	Depth (m)	# Disks	Dose Rate (Gy/kyr)	Uncertainty (Gy/kyr)	De (Gy)	2 SE (Gy)	Method	Comments
OS-WS	Slocum (Qs)	130-190	1.1	14 (15)	8.43	0.43	891.94	93.54	IRSL	Fading = 2.2 ± 0.4 (n=5)
OS-SL1-UP	Bull Lake Outwash (Qbo)	160	2.8	12 (13)	5.84	0.24	405.28	21.81	IRSL	Fading = 1.9 ± 0.3 (n=6)
OS-CX	Bull Lake Outwash (Qbo)	160	6.6	14 (15)	7.16	0.35	720.53	49.29	IRSL	Fading = 1.5 ± 0.02 (n=5)
OS-CC	Louviers Alluvium (Ql)	20-50	1.6	19 (29)	4.49	0.18	80.42	8.30	OSL	IR contaminated
OS-CH	Verdos (Qv)	300	1.6	13 (13)	5.42	0.23	218.29	27.93	IRSL	Fading = 2.9 ± 0.4 (n=6)
OS-FL	Slocum (Qs)	130-190	1.2	12 (12)	3.97	0.16	337.07	41.49	IRSL	Fading = 2.2± 0.2 (n=6)
OS-FL-PR	Louviers Alluvium (Ql)	20-50	1.3	18 (28)	4.33	0.17	218.07	30.88	OSL	IR contaminated

Appendix C

River profile analysis

For graded, steady-state river profiles, where the rock uplift rate, U, is balanced by the long term erosion rate, E, the relationship between local channel slope, S, and the upstream drainage area, A, can be described by a power function (Flint, 1974):

$$S = k_s A^{-\theta} \tag{C1}$$

where k_s is the channel steepness index and θ is the channel concavity index (Kirby and Whipple, 2012). The covariation of k_s and θ requires normalization which is typically done by fixing θ to a reference value (i.e., reference concavity index, θ_{ref}) of ~0.3-0.7 to calculate the normalized channel steepness index k_{sn} (Kirby and Whipple, 2012; Lague, 2014; Harel et al., 2016). Equation C1 can be used to derive k_s or k_{sn} empirically from regression through S and A data. However, such calculation introduces noise and requires a large amount of smoothing (Snyder et al., 2000; Wobus et al., 2006). Thus, it is preferable to use χ, a path-dependent integral parameter of the inverse of A raised to θ_{ref} (Royden and Perron, 2013):

$$\chi = \int_{x_b}^{x} \left(\frac{A_0}{A(x')}\right)^{\theta_{ref}} dx' \tag{C2}$$

where x_b is the referenced distance at the drainage network outlet, x is the upstream distance along the channel, and A_0 is the referenced upstream drainage area, usually chosen as unity ($A_0 = 1$). Equation C1, where $S = dz/dx$, can be integrated with respect to distance to generate a χ-elevation plot (typically referred to as a χ-plot):

$$z(x) = z(x_b) + k_{sn}\chi \tag{C3}$$

where the slope of a linear regression of $\chi - z$ is k_{sn}. We calculate χ by implementing A and drainage area weighted by the spatial distribution of mean annual precipitation, $MAP \times A$, in equation C2, using ChiProfiler (Gallen and Wegmann, 2017). We use χ and the precipitation-weighted χ to calculate k_{sn} and $k_{sn}Q$ (cf. Adams et al., 2020), respectively, by calculating linear regressions through the basin-wide χ-z data (Equation C3; 56, inset in the main text). We calculate the R^2 for each of these linear regressions to determine the basin morphological steady state, where higher R^2 values reflect basins that appear to be morphologically in steady state (i.e., roughly linear χ-z plots), and low R^2 values reflect basins that are in transient state (56, inset in the main text). We conduct this analysis for all basins with published 10Be cosmogenic nuclide basin average erosion rates from fluvial sands from the Octopus archive (Codilean et al., 2018).

Binning, regressions, and sensitivity analyses

We use existing global climate data of mean annual precipitation (MAP), mean annual temperature (MAT) (Fick and Hijmans, 2017), aridity index (AI) (Trabucco and Zomer, 2009), and SRTM 3-arc second digital elevation model (DEM) tiles (ME) (OpenTopography) to calculate mean climate proxy values for each basin (56 in the main text, Figure C1; Table C1). We convert all global data to rasters, project them to the WGS 84 geographic coordinate system, and crop them to the basin geometries, using Arc Pro 2.0.8. We project the basin rasters to a UTM coordinate system, resample them to 90 m cell size, calculate their mean MAP, MAT, AI, and ME values using Matlab and TopoToolbox (Schwanghart and Scherler, 2014), and compile this data with E, k_{sn}, and $k_{sn}Q$ data for each basin (Table C1). To control for bedrock variability, we restrict our analysis to bedrock rivers that drain ≥ 90% crystalline rocks (plutonic and metamorphic units) based on a global composite geological map (Figure C2A; 'GLiM'; Hartmann and Moosdorf, 2012). We calculate the distribution and dominance of plutonic and metamorphic units and compare them to MAP, MAT, AI, and ME in each basin to ensure that there is no global relationship between rock type and climate variability (Figure C2B; Table C1).

We bin the $E - k_{sn}$ and $E - k_{sn}Q$ datasets based on increments of MAP, MAT, AI, and ME (Figure C3). We select the bins to have an equal number of data points, with at least 15 data points in each bin. For each climate bin, we conduct a linear regression through log-transformed $E - k_{sn}$ and $E - k_{sn}Q$ data using total least squares to determine the power-law exponent, p, and its constant, C, in equation 1 (main text) (Figure C4). We assess the relationships between these parameters and the climate proxy data to evaluate if systematic patterns exist (Figure C4). We attempt to account for the general nonlinearity (i.e., p) in the global dataset by conducting normalized regressions through the data under a fixed p~2.2 (i.e., the global value of our dataset; cf. Harel et al., 2016; Adams et al., 2020) to determine the normalized y-intercept, C_{ne}, for the $E - k_{sn}$ and $E - k_{sn}Q$ data sets (Figure C5; Table C2). For all modeled regressions, we calculate the statistical goodness-of-fit metrics of R^2, χ^2, and Kolmogorov-Smirnov two-sided p-value at the 90% significance level to evaluate the significance of p and C_{ne} in our analysis (Table C2).

We conduct several sensitivity analyses to evaluate the robustness of p in our modeled regressions, namely testing the impact of the number of bins with equal number of data points per bin (e.g., for the dataset in Table C1, 4 bins with 66 points per bin, 6 bins with 44 points per bin, 8 bins with

33 points per bin, etc.; Figure C6A) and testing for the impact of transience in our basin analysis by changing the minimum R^2 morphological threshold value from $R^2 = 0.75$ to $R^2 = 0.95$ (56, inset in main text, Figure C6B; Table C2). Generally, the increase of R^2 improve the overall fit for all modeled regressions but do not change the overall systematic patterns (Figure C6B; Table C2).

Threshold stochastic stream power incision models (STIMs) and discharge variability

Bedrock channel incision rate, I, is often modeled as a function of the magnitude of the shear stress (or stream power) exerted on a river bed (Howard, 1994). Approximations of this general concept simulate incision as a function of the channel slope, S, raised to an exponent n, upstream drainage area, A, raised to an exponent m, and an erodibility coefficient, K, which captures rock type, climate and downstream changes in the channel hydraulic geometry (Howard, 1994; Whipple and Tucker, 1999):

$$I = KA^m S^n - \psi \qquad \text{(C4),}$$

where ψ is a threshold term for channel incision. Assuming that the incision threshold is negligible and that $I \cong E$ in steady-state basins, equation C4 is reduced to the constant effective discharge stream power incision model (SPIM) solution (Howard, 1994; Kirby and Whipple, 2012; Lague, 2014):

$$E = KA^m S^n \qquad \text{(C5).}$$

However, when ψ is significant, the critical discharge needed to overcome the threshold shear stress, Q_c (which is typically defined by the effective bedload grain size), and the distribution of floods are important. Stochastic threshold stream power incision models (or STIMs) account for this via the calculation of E as the integral of the product of I (equation DR4) and the probability of threshold-breaching floods (i.e., floods large enough to generate shear stress capable of exceeding ψ) for specific normalized discharges, $pdf(Q^*)$:

$$Q^* = Q/\overline{Q} \qquad \text{(C6)}$$

$$E = \int_{Q_c}^{Q_{max}} I(Q^*) pdf(Q^*) dQ \qquad \text{(C7),}$$

where Q, $\bar{Q}$, Q^*, and Q_{max} are the actual, mean, normalized, and maximum discharges, respectively (Lague et al., 2005; DiBiase and Whipple, 2011). Lague et al. (2005) present a model where $pdf(Q^*)$ is represented by an inverse gamma distribution:

$$pdf(Q^*) = \frac{k^{k+1}}{\Gamma(k+1)} exp\left(-\frac{k}{Q^*}\right) Q^{*^{-(2+k)}} \quad \text{(C8),}$$

where Γ is the inverse gamma function, and k is a shape parameter that describes discharge variability. In this model, low to high k reflect heavier-tailed, higher-variability flood distributions to lighter-tailed, lower-variability flood distributions (Lague et al., 2005; Lague, 2014).

This model predicts that in threshold-dominated bedrock river systems, the nonlinearity between E and k_{sn} (equation 1 in main text) systematically increases with decreasing discharge variability (i.e., higher k in equation C8; 59 in main text). This behavior arises because for steeper channels, smaller magnitude floods are capable of overcoming incision thresholds, while for shallow to moderate channels, small floods are less effective, allowing only larger floods to overcome bedrock incision thresholds (Lague et al., 2005; DiBiase and Whipple, 2011; Deal et al., 2018). The integral of discharge events that breach this incision threshold is related to the erosional efficiency in a STIM framework, where more threshold breaching events increase erosional efficiency. Thus, as channel steepness increases, the flood size needed to breach thresholds declines, and more erosive floods are included in a lighter-tailed, lower discharge flood distribution relative to a heavier-tailed, higher discharge flood distribution system. It is these general concepts that explain why the nonlinearity between E and k_{sn} increases with decreasing discharge variability.

To empirically determine k from discharge records, it is easier to use the complementary cumulative distribution function, $ccdf(Q^*)$, to avoid binning complexities when comparing actual discharge data (DiBiase and Whipple, 2011):

$$ccdf(Q^*) = \Gamma(k/Q^*, k+1) \quad \text{(C9).}$$

Empirical studies and theory suggest k to systematically increase with increasing MAP and AI (Lague, 2014; Rossi et al., 2016; Deal et al., 2018). To demonstrate this general pattern at the global scale, we use equation C9 along with several discharge records near some of our studied basins to empirically determine the shape parameter k for each of these stations and compare it with MAP and AI patterns. We gather mean daily discharge records of ~20-50 years from several gauges near some of our analyzed basins that span a large range of climate conditions (see locations in 56 in main text, Figure C1), to calculate their exceedance probability plots (Figure C7A). We calculate similar exceedance probability plots using Lague et al.'s STIM and equation C9 to verify that STIM predictions generally fit the recorded data (Figure C7B). From the STIM exceedance probability plots, we calculate k and compare it with MAP and AI at each gauge station (59 in main text; Figure C7C; DiBiase and Whipple, 2011; Lague, 2014; Deal et al., 2018).

We find that for the calculated k range using STIMs, p values as a function of the normalized incision threshold, ψ/E, and discharge variability under locally-calibrated parameters (59 in main text; DiBiase and Whipple, 2011; Lague, 2014) are consistent with empirically derived p from our global analysis (Figure C4), where for both cases, p increases from ~1 to 5 with an increase in k from ~0.1 to 3 (Figure 3.3, 59 in main text, Figure C7; Molnar et al., 2006; Lague, 2014; Deal et al., 2018). Thus, assuming STIMs are representative for the analyzed basins in this study, our results imply that incision thresholds are important, and that discharge variability decreases with increasing MAP and AI globally.

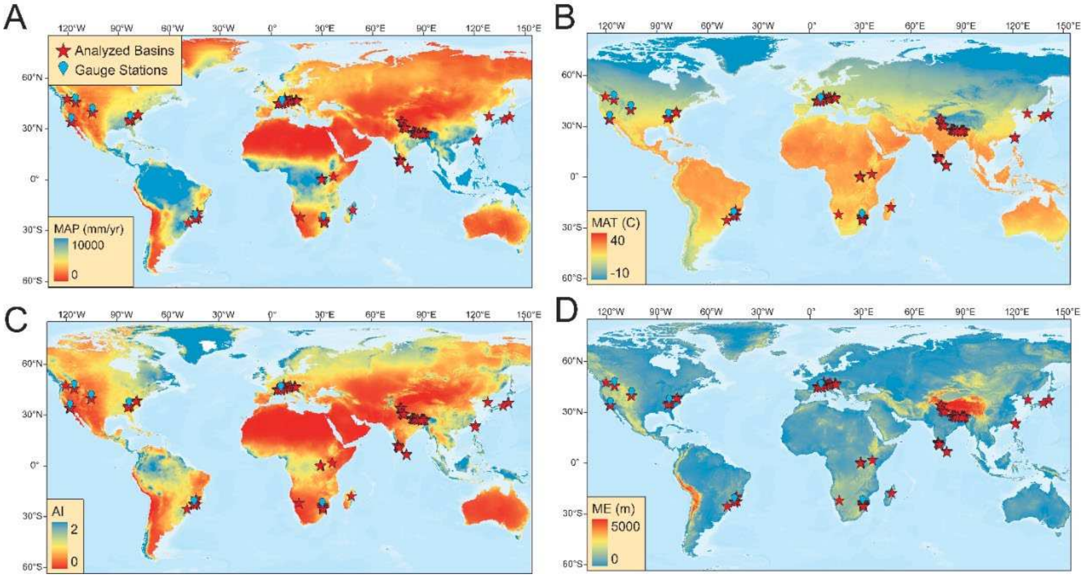

Figure C1 Global climate rasters used for our analysis. ***(A)*** *Mean annual precipitation (MAP; 'WorldClim 2'; Fick and Hijmans, 2017)* ***(B)*** *Mean annual temperature (MAT; 'WorldClim 2'; Fick and Hijmans, 2017);* ***(C)*** *Aridity index (AI; 'CGIAR-CSI'; Trabucco and Zomer, 2009);* ***(D)*** *Elevation (ME; 'ETOPO1'; Amanter and Eakins, 2009). Marked are the locations of the analyzed basin regions (red stars) and stream gauge stations in Figure C7 (cyan marks).*

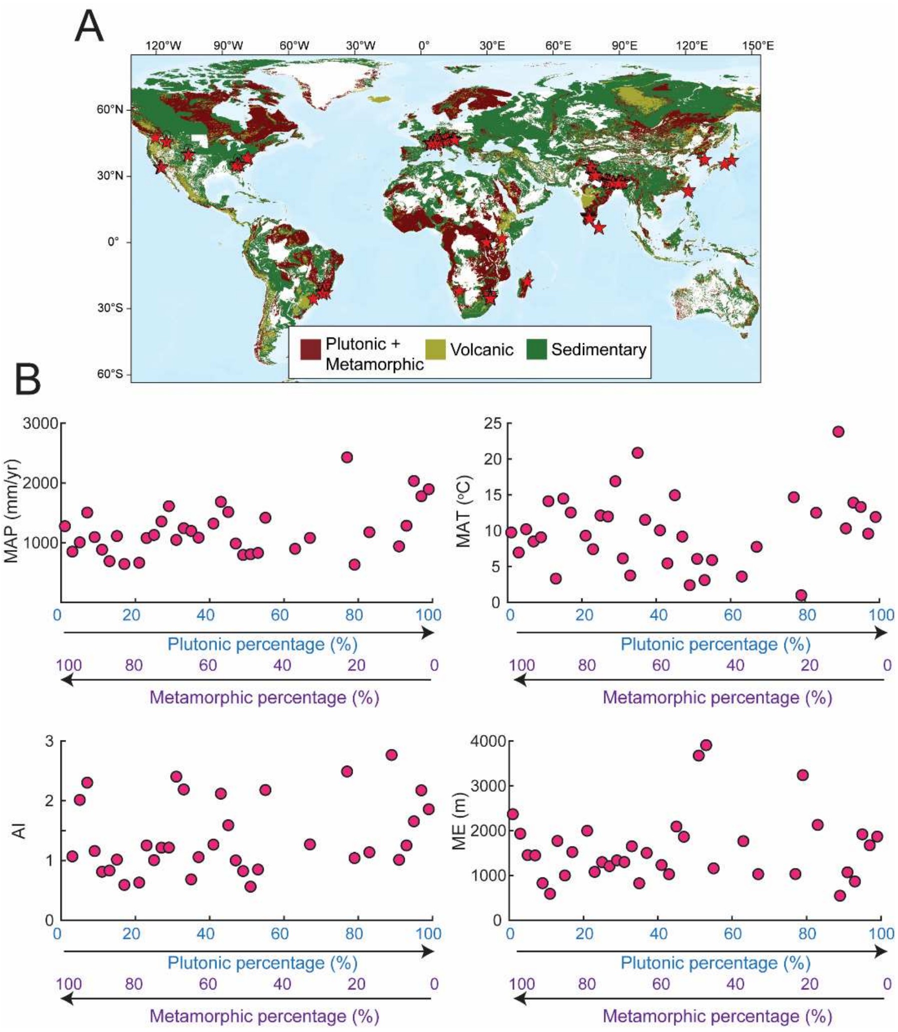

Figure C2 ***(A)*** *Global rock type data (after 'GLiM'; Hartmann and Moosdorf, 2012) classified by crystalline, volcanic, and sedimentary rocks, where crystalline rocks consist of plutonic and metamorphic units. All analyzed basins in this study consist of at least 90% crystalline units.* ***(B)*** *Binned data of the percentages of plutonic and metamorphic units for 265 basins under a steady state threshold of* $R^2 > 0.9$*, versus MAP, MAT, AI, and ME (Table C1). At the global scale, no relationship is observed between changes in the percentage of plutonic or metamorphic units and climate variability.*

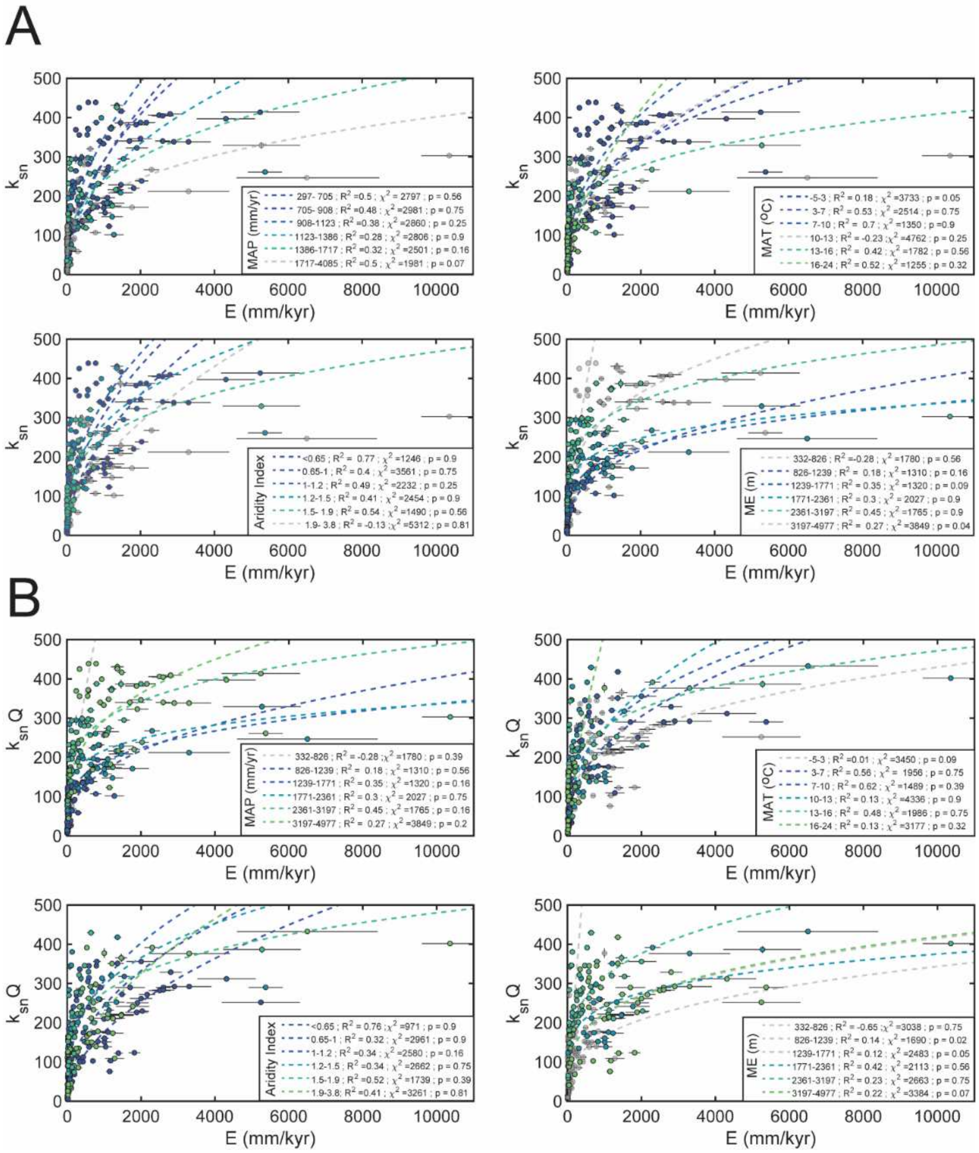

Figure C3 ***(A)*** *Modeled regressions for* k_{sn} *versus* E *(equation 1 in main text) for 265 basins under a steady state threshold of* $R^2 > 0.9$*, where each data point represents one basin. Data is classified and binned by (from top left clockwise) MAP, MAT, AI, and ME (see Table C1). Legend shows statistical goodness-of-fit parameters (*R^2*,* χ^2*,KS test p-value) for each climate bin modeled regression (see Table C2).* ***(B)*** *Same as (A) but for* $k_{sn}Q$*, where MAP across the basin is weighted in drainage area prior to calculation of* χ *(see text). The regressions and associated data points with low or negative* R^2 *or KS test p-value < 0.1 are colored in transparent grey (see also Table C2).*

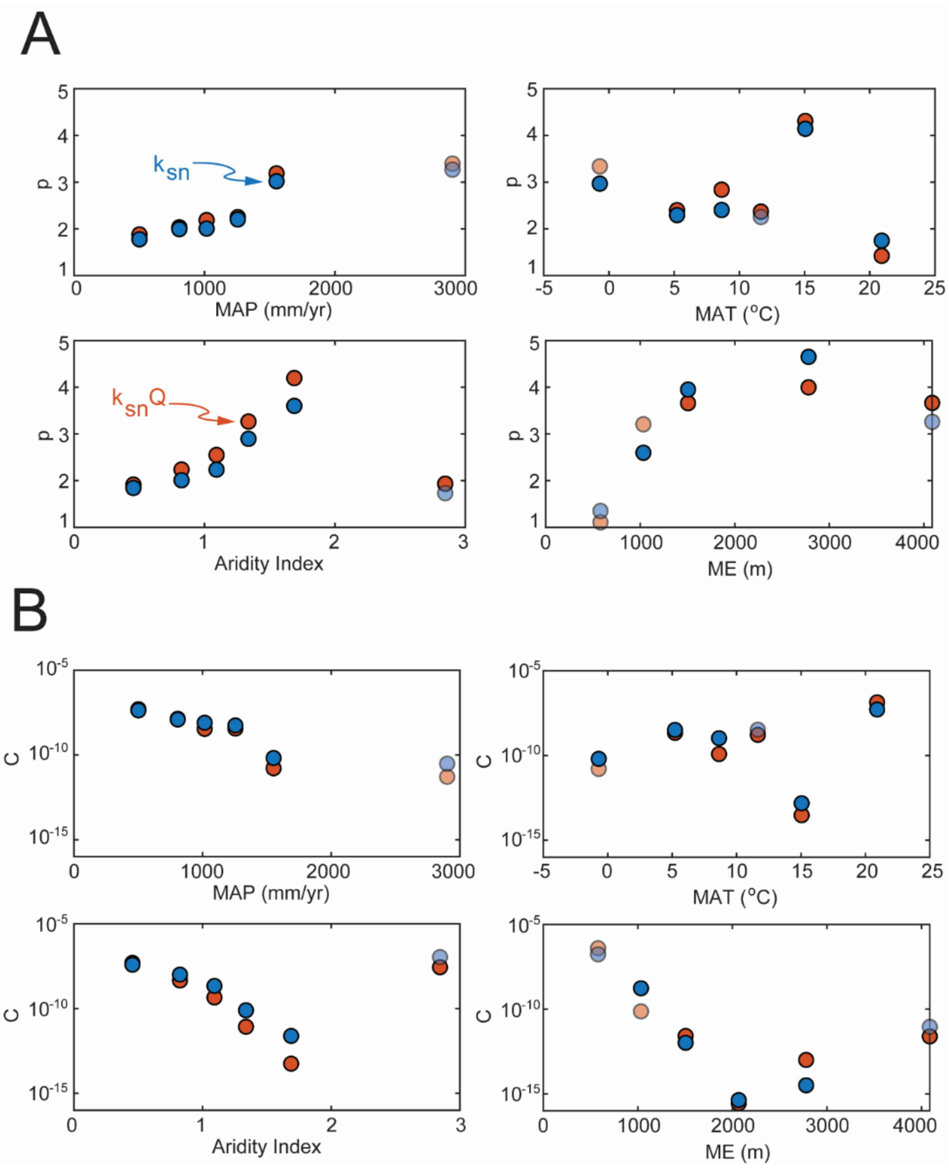

Figure C4 ***(A)*** *Values of p in equation 1 for each modeled regression for k_{sn} and $k_{sn}Q$ under changes in MAP, MAT, AI, and ME. Note a systematic increase in p with increasing MAP (i.e., wetter) and AI (i.e., higher humidity).* ***(B)*** *Same as (A) but for C in equation 1. Note a systematic decrease in C with increasing MAP and AI. For all regressions, $k_{sn}Q$ does not significantly change systematic patterns. For both (A) and (B), associated p and C with low or negative R^2 or p-value < 0.1 are transparent (see also Table C2).*

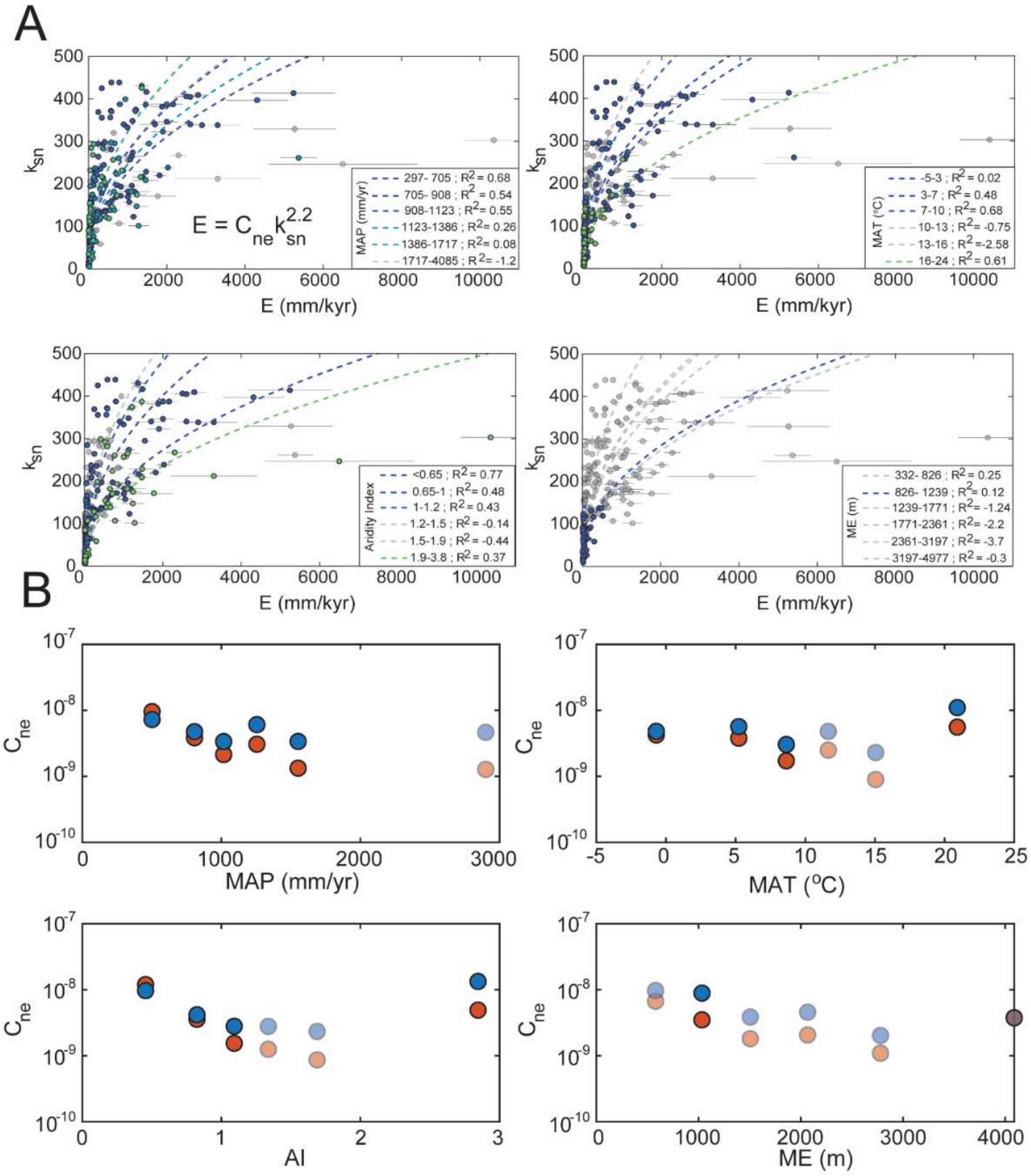

Figure C5 ***(A)*** *Modeled normalized regressions for k_{sn} versus E (equation 1 in main text) under a fixed p = 2.2, which is the global value from best fit regression through the entire E - k_{sn} dataset. Regressions and associated data points with low or negative R^2 or p-value < 0.1 are colored in transparent grey (see also Table C2).* ***(B)*** *Changes in C_{ne} under a fixed p = 2.2. Note that C_{ne} generally decreases from ~$10^{-8}m^{-7}yr^{-1}$ to $10^{-9}m^{-8}yr^{-1}$ with all climate proxies. $k_{sn}Q$ does not significantly change systematic patterns. Associated C_{ne} with low or negative R^2 or p-value < 0.1 are transparent (see Table C2).*

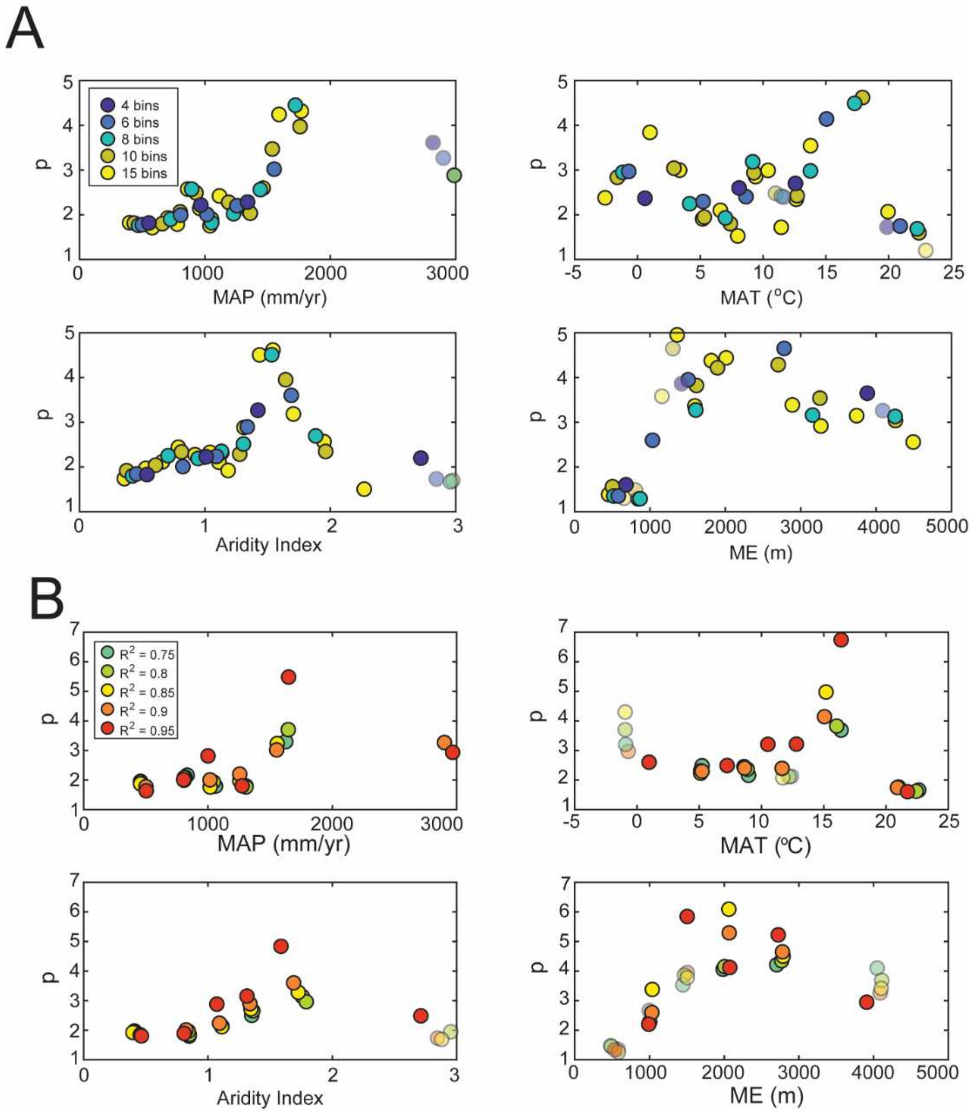

Figure C6 Sensitivity analyses for modeled regressions under ***(A)*** *changes of the number of bins and* ***(B)*** *changes of the R^2 threshold used to define morphological steady state (e.g., Figure 1, inset in main text). p (and hence C that covary with it; Figure C4) is statistically robust to changes in MAP and AI under different number of bins and R^2 threshold values and to changes in ME and MAT under different R^2 threshold values. For both (A) and (B), associated p with low or negative R^2 or p-value < 0.1 are transparent (see also Table C2).*

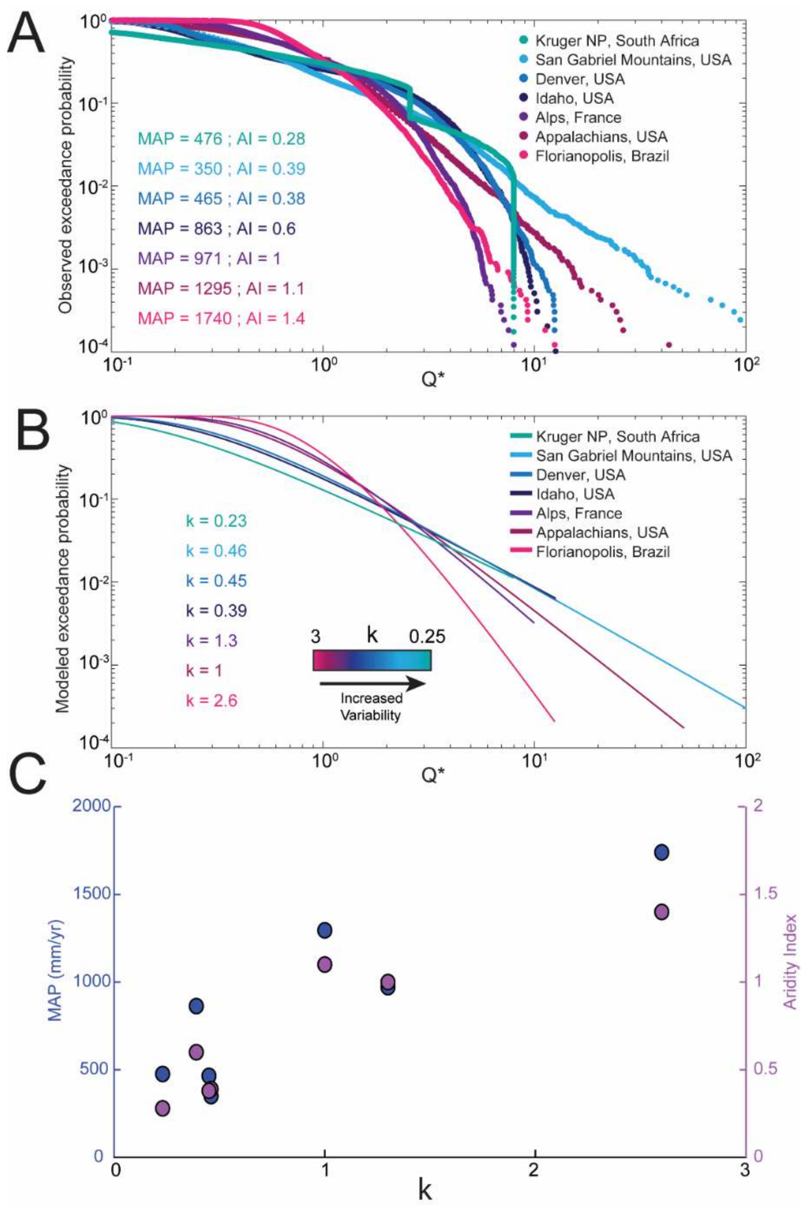

Figure C7 ***(A)*** *Exceedance probability plots of normalized recorded mean daily discharge (m^3/s), Q^* (equation C6), from seven stream gauge stations with records spanning ~20-50 yrs near some of our analyzed basins (for locations, see 56 in main text, C1).* ***(B)*** *Exceedance probability plots based on modeled cumulative distribution function of the normalized discharge, $ccdf(Q^*)$ (equation C9), where low to high k represents high to low discharge variability (Lague et al., 2005; DiBiase and Whipple, 2011; Deal et al., 2018). Note a general systematic decrease in discharge variability (higher k) with increasing MAP and AI.* ***(C)*** *MAP and AI as a function of k based on (A) and (B).*

Table C1 Locations, climate proxy values, erosion rates, k_{sn}, $k_{sn}Q$, and percentage of crystalline units for 265 analyzed basins under a morphological steady-state threshold of $R^2 > 0.9$.

Global Zone	Basin ID	Publication	Latitude (WGS84)	Longtitude (WGS84)	MAP (mm/yr)		MAT (°C)		AI		ME (m)		E (m/My)		Ksn ($m^{0.9}$)		KsnQ ($m^{0.9}$)		Crystalline Area (%)	
					Mean	STD	Mean	STD	Mean	STD	Mean	STD	Mean	STD	Mean	STD	Mean	STD	Plut.	Meta.
App	2	Duxburry, 2008	-78.24	38.65	1102	43	11	1	1.04	0.1	551	175	17	2	58.37	1.03	61.49	1.13	10	83
App	4	Duxburry, 2008	-78.26	38.61	1147	39	10	1	1.12	0.09	688	147	16	2	82.79	2.02	88.69	2.14	10	90
App	5	Duxburry, 2008	-78.29	38.57	1152	54	10	1	1.13	0.12	697	200	17	2	94.56	1.42	101.9	1.56	21	75
App	7	Duxburry, 2008	-78.79	38.2	1152	54	10	1	1.13	0.12	697	200	15	2	94.56	1.42	101.9	1.56	0	100
App	13	Matmon, 2003	-83.13	35.74	1127	26	11	0	1.04	0.05	639	108	14	2	25.45	0.66	27.01	0.72	0	97
App	16	Matmon, 2003	-83.25	35.61	1163	16	12	1	0.97	0.05	543	150	11	1	27.59	1.07	29.54	1.16	0	90
App	20	Sullivan, 2007	-82.22	35.57	1275	35	13	1	1.13	0.15	633	240	25	2	34.07	0.5	38.1	0.57	0	100
App	21	Linari, 2016	-82.22	35.57	1625	150	9	1	1.6	0.26	1306	258	34	4	125.69	1.8	160.1	2.17	0	100
App	22	Matmon, 2003	-83.25	35.56	1654	130	9	1	1.65	0.24	1349	232	33	4	108.39	1.39	138.7	1.68	0	100
App	23	Linari, 2016	-82.38	35.54	1319	40	13	1	1.1	0.08	673	160	29	2	48.44	1.9	55.29	2.2	0	100
App	24	Sullivan, 2007	-82.38	35.54	1319	39	13	1	1.1	0.08	674	155	23	3	51.38	1.98	58.69	2.29	0	100
App	25	Matmon, 2003	-83.31	35.52	1791	49	9	1	1.86	0.13	1517	139	19	3	53.72	0.82	70.25	1.06	0	100
App	26	Matmon, 2003	-83.29	35.52	1314	28	13	0	1.07	0.05	587	118	18	2	22.84	1.3	25.88	1.49	0	93
App	27	Matmon, 2003	-83.3	35.51	1314	28	13	0	1.07	0.05	588	120	23	2	21.11	1.35	23.91	1.54	0	90
App	28	Matmon, 2003	-83.57	35.47	1770	71	9	1	1.81	0.16	1464	175	19	2	103.24	2.97	134.8	3.84	0	97
App	30	Matmon, 2003	-83.43	35.46	1340	29	13	0	1.12	0.05	706	114	32	2	44.74	1.41	51.15	1.64	0	94
App	31	Matmon, 2003	-83.53	35.46	1687	120	10	1	1.61	0.22	1249	225	23	3	93.55	1.29	120.5	1.74	0	100
App	32	Linari, 2016	-82.18	35.34	1412	58	12	1	1.24	0.11	915	136	16	1	30.79	1.29	36.34	1.56	0	100
App	33	Sullivan, 2007	-82.18	35.34	1395	43	12	0	1.2	0.08	874	98	13	2	21.12	0.55	24.62	0.65	0	100
App	34	Linari, 2016	-82.32	35.32	1595	92	11	1	1.42	0.15	1021	181	23	3	78.22	0.78	98.01	0.97	7	93
App	37	Reusser, 2015	-83.77	34.74	1661	129	10	1	1.58	0.25	1226	270	28	4	81.29	0.52	103.9	0.69	0	100
CUS	3	Kirchner, 2001	-115.34	45.99	684	7	5	0	0.81	0.03	1566	105	32	4	51.86	0.9	43.77	0.76	0	100
CUS	4	Kirchner, 2001	-115.33	45.99	684	5	4	0	0.82	0.04	1594	118	28	4	60.4	2.04	50.92	1.72	0	100
CUS	8	Kirchner, 2001	-115.34	45.71	692	19	3	1	0.83	0.06	1771	170	21	3	69.4	0.53	58.68	0.47	12	88
CUS	9	Kirchner, 2001	-115.33	45.67	666	13	3	0	0.81	0.02	1769	104	21	3	44.27	0.74	36.67	0.61	3	97
CUS	12	Foster, 2016	-105.47	40.16	502	31	3	1	0.65	0.1	2787	169	16	1	80.65	3.74	59.5	2.91	99	0
CUS	13	Dethier, 2014	-105.53	39.96	502	31	3	1	0.65	0.1	2787	169	19	2	80.65	3.74	59.5	2.91	46	51
CUS	14	Dethier, 2014	-105.35	39.86	633	88	1	1	1.04	0.26	3239	300	38	3	104.71	0.94	87.89	0.8	79	21
CUS	15	Dethier, 2014	-105.33	39.74	486	23	4	1	0.62	0.09	2718	179	18	2	89.3	3.13	65.37	2.24	0	100
Pac	4	Moon, 2011	-120.37	47.74	937	235	4	2	1.23	0.43	1332	350	127	9	125.95	0.87	130.3	0.78	47	53
Pac	10	DiBiase, 2010	-118.12	34.33	532	65	14	1	0.47	0.08	1355	180	135	33	64.59	0.44	49.92	0.44	90	10
Pac	13	DiBiase, 2010	-117.73	34.31	766	58	10	2	0.73	0.11	2022	420	1106	204	195.82	2.06	175.9	1.88	2	98
Pac	14	DiBiase, 2010	-117.73	34.31	744	47	10	1	0.69	0.08	1950	345	1039	175	157.41	1.42	138.6	1.24	4	96
Pac	16	DiBiase, 2010	-117.98	34.31	705	59	12	1	0.67	0.1	1728	297	239	28	135.26	3.77	117.4	3.39	100	0
Pac	17	DiBiase, 2010	-117.76	34.3	768	31	10	1	0.73	0.07	1951	317	1006	191	170.07	2.29	150.9	2.01	24	76
Pac	18	DiBiase, 2010	-118.26	34.3	474	55	14	1	0.41	0.06	1149	242	424	37	137.44	1.63	100.8	1.11	83	17
Pac	19	DiBiase, 2010	-117.74	34.3	750	60	10	2	0.71	0.1	1964	389	436	50	197.1	2.3	174.6	2.02	14	86
Pac	20	DiBiase, 2010	-117.74	34.3	750	60	10	2	0.71	0.1	1964	389	717	106	197.1	2.3	174.6	2.02	3	97
Pac	21	DiBiase, 2010	-117.89	34.27	746	61	10	1	0.69	0.1	1954	382	826	79	172.13	1.85	152.2	1.73	100	0
Pac	22	DiBiase, 2010	-117.89	34.27	656	134	12	1	0.59	0.13	1532	364	591	84	160.57	1.23	138.3	1.09	100	0
Pac	23	DiBiase, 2010	-117.97	34.25	613	143	13	1	0.55	0.14	1404	361	428	85	134.9	2.01	112.4	2.05	93	7
Pac	24	DiBiase, 2010	-117.76	34.24	644	110	13	1	0.59	0.13	1523	339	292	37	131.66	1.44	111.9	1.28	16	84
Pac	25	DiBiase, 2010	-117.64	34.16	706	121	11	2	0.66	0.13	1809	477	1010	108	182.72	1.22	160.4	1.11	47	52
Alps	1	Meyer, 2010	8.21	48.24	1347	116	7	1	1.56	0.23	788	169	91	7	85.97	0.84	100.1	1.02	87	8
Alps	6	Morel, 2003	8.2	47.94	1487	81	6	0	1.96	0.1	989	69	43	5	19.95	0.68	24.16	0.82	0	100
Alps	8	Morel, 2003	8.16	47.88	1685	73	5	0	2.12	0.17	1028	78	73	10	28.87	0.82	36.85	1.05	43	57
Alps	9	Morel, 2003	8.26	47.87	1524	158	6	0	2	0.24	983	105	47	6	24.65	0.29	30.6	0.38	14	82
Alps	10	Morel, 2003	8.22	47.86	1587	119	6	0	2.02	0.17	987	87	110	15	26.52	0.59	33.38	0.75	52	43
Alps	17	Dixon, 2016	14.66	47.27	1494	186	3	1	2.37	0.39	1588	299	77	5	107.04	1.68	131.9	2.08	0	99
Alps	18	Norton, 2011	12.42	47.27	1333	150	2	2	2.41	0.75	1956	467	1090	470	181.96	3.32	211.7	3.86	3	97
Alps	19	Norton, 2011	11.26	47.25	1333	150	2	2	2.41	0.75	1956	467	650	110	181.96	3.32	211.7	3.86	0	99
Alps	22	Dixon, 2016	14.78	47.15	1246	141	0	3	2.95	1.17	2238	513	710	130	224.01	2.32	251.3	2.6	0	98
Alps	25	Norton, 2011	12.13	47.05	1458	113	-1	2	3.25	1.1	2363	414	1240	240	174.93	3.18	210.5	3.82	32	68
Alps	26	Dixon, 2016	14.82	46.94	1384	100	-1	2	3.04	0.78	2351	335	1230	290	147.51	2.86	173.4	3.4	0	94
Alps	28	Dixon, 2016	15.17	46.84	1080	154	1	3	2.45	1.07	2085	469	530	100	154.41	2.02	165.5	2.17	0	100
Alps	29	Dixon, 2016	15.18	46.82	1229	123	5	1	1.73	0.26	1144	271	57	3	93.69	1.05	104.7	1.25	0	100
Alps	32	Savi, 2014	11.02	46.72	861	44	2	2	1.84	0.43	1907	321	376	70	294.49	12.22	277.6	11.23	0	100
Alps	33	Savi, 2014	11.02	46.72	861	44	2	2	1.84	0.43	1907	321	246	42	294.49	12.22	277.6	11.23	0	100
Alps	34	Savi, 2014	11.03	46.71	895	54	2	2	2.07	0.56	2012	387	1470	340	228.82	8.08	220.8	7.63	0	100
Alps	42	Savi, 2014	11.07	46.67	832	156	-2	2	3.56	1.19	2559	366	412	26	298.59	9.93	287.1	8.87	0	99
Alps	44	Dixon, 2016	15.14	46.61	790	161	0	3	3.11	1.39	2368	537	1460	160	386.75	11.3	365.3	10.02	0	100
Alps	46	Dixon, 2016	15.43	46.53	790	160	0	3	3.09	1.4	2353	559	1210	120	374.92	8.07	350.8	7.07	5	95
Alps	47	Wittmann, 2007	8.64	46.41	770	213	0	3	3.21	1.6	2362	534	580	110	281.45	3.05	262.4	2.67	0	92
Alps	49	Norton, 2011	10.25	46.33	1284	126	5	2	1.79	0.29	1184	307	69	6	118.47	0.95	136	1.05	0	91
Alps	50	Wittmann, 2007	8.71	46.25	593	176	-1	3	3.22	1.57	2424	535	1100	300	265.4	2.77	221.8	2	0	100
Alps	54	Wittmann, 2007	8.7	46.17	1369	90	2	2	3.71	1.01	1964	441	770	130	260.66	7.39	297.9	8.29	7	92
Alps	57	Wittmann, 2007	8.26	46.02	1431	63	4	2	2.89	0.74	1646	454	590	120	146.64	3.09	171.8	3.61	7	93
Alps	58	Wittmann, 2016	8.53	45.96	1431	63	4	2	2.89	0.74	1646	454	600	110	146.64	3.09	171.8	3.61	0	100
Alps	59	Wittmann, 2007	8.26	45.81	1251	70	6	2	2.35	0.58	1333	441	560	100	138.39	1.53	150.5	1.74	5	92
Alps	60	Glotzbach, 2013	6.14	45.41	1251	70	6	2	2.35	0.58	1333	441	660	160	138.39	1.53	150.5	1.74	54	43
Alps	62	Glotzbach, 2013	6.26	45.39	1131	83	2	3	3.8	1.44	1930	605	1460	330	208.61	1.38	218.6	1.47	30	69
Alps	64	Glotzbach, 2013	7.06	45.37	1188	51	6	2	2.29	0.5	1341	385	1280	260	101.73	1.73	109.2	1.85	0	100
Alps	65	Olivetti, 2016	4.68	45.35	1239	55	8	2	1.98	0.33	1087	354	286	24	116.55	2.04	126.5	2.29	91	3
Alps	66	Olivetti, 2016	4.56	45.3	899	146	4	4	3.07	1.75	1766	695	830	260	193.54	1.32	178.1	1.3	61	37
Alps	67	Olivetti, 2016	4.55	45.29	1134	52	7	2	2.11	0.46	1240	421	244	27	128.53	0.88	134.6	0.94	76	24
Alps	69	Olivetti, 2016	4.41	45.24	1471	125	4	2	2.23	0.58	1716	377	330	90	198.41	3.01	240.7	3.74	100	0
Alps	72	Olivetti, 2016	4.38	45.21	890	50	11	1	0.95	0.09	472	174	39	2	61.44	1.79	58.87	1.81	2	98
Alps	75	Olivetti, 2016	4.29	45.14	1081	79	8	1	1.27	0.14	1030	175	44	3	90.52	1.42	95.43	1.43	68	32

Alps	76	Olivetti, 2016	4.6	45.14	1042	74	8	1	1.19	0.13	970	186	46	4	75.92	1.27	78.17	1.32	9	91
Alps	77	Olivetti, 2016	4.3	45.11	871	8	11	0	0.91	0.02	382	42	67	5	52.85	3.53	49.79	3.32	37	63
Alps	78	Olivetti, 2016	4.66	45.07	1079	49	7	0	1.25	0.08	1081	93	34	2	38.78	0.72	40.64	0.73	23	77
Alps	79	Olivetti, 2016	4.78	45.06	996	80	9	1	1.1	0.13	820	230	49	3	69.39	1.1	70.28	1.16	24	76
Alps	80	Olivetti, 2016	4.72	45.06	995	88	8	1	1.12	0.13	957	137	53	4	50.49	0.34	51.54	0.34	28	72
Alps	81	Olivetti, 2016	4.5	45.04	1071	56	8	0	1.22	0.09	1066	103	46	3	44.04	0.41	45.94	0.46	1	99
Alps	82	Olivetti, 2016	4.39	45.02	1052	53	8	1	1.18	0.09	992	141	79	6	62.07	2.98	63.52	3.1	42	58
Alps	85	Olivetti, 2016	4.53	44.99	1005	48	9	1	1.09	0.08	820	143	47	4	57.53	0.82	58.39	0.86	11	89
Alps	86	Delunel, 2010	6.48	44.99	1031	44	8	0	1.14	0.06	1022	75	39	3	33.52	0.82	34.43	0.85	38	54
Alps	88	Olivetti, 2016	4.81	44.9	964	59	10	1	1.01	0.1	671	221	60	6	59.64	0.21	59.53	0.21	32	68
Alps	89	Delunel, 2010	6.45	44.89	977	65	10	1	1.03	0.11	743	224	64	6	55.76	0.27	55.97	0.28	36	62
Alps	90	Delunel, 2010	6.44	44.88	1028	63	8	1	1.13	0.1	940	162	66	6	65.56	0.54	67.28	0.56	33	64
Him	6	Munack, 2014	76.63	34.5	104	16	-3	4	0.15	0.02	4454	592	63	5	259.83	2.97	93.08	1.04	100	0
Him	10	Dortch, 2011	77.35	34.34	121	4	-10	1	0.16	0.02	5251	217	31	4	107.39	3.75	41.85	1.43	100	0
Him	14	Dortch, 2011	77.76	34.28	115	4	-9	2	0.17	0.02	5154	264	51	9	130.36	1.94	49.66	0.72	100	0
Him	15	Dortch, 2011	77.29	34.25	113	7	-6	4	0.14	0.02	4704	532	39	8	246.32	3.03	93.96	1.16	100	0
Him	16	Munack, 2014	77.45	34.22	118	4	-5	3	0.14	0.01	4808	372	22	2	201.48	1.63	77.58	0.62	100	0
Him	17	Munack, 2014	77.39	34.22	112	5	-3	3	0.13	0.01	4500	376	19	2	162.65	1.68	61.42	0.67	100	0
Him	18	Munack, 2014	77.34	34.21	114	7	-4	5	0.14	0.02	4594	574	33	3	236.83	2.12	90.47	0.78	100	0
Him	19	Munack, 2014	77.34	34.2	113	7	-4	5	0.14	0.02	4546	601	31	3	236.19	2.4	90.17	0.91	100	0
Him	21	Dortch, 2011	77.66	34.16	116	5	-7	3	0.16	0.02	4944	424	20	3	219.68	4.76	84.51	1.79	100	0
Him	23	Scherler, 2014	77.96	31.25	1003	142	3	5	1.33	0.09	3722	641	1060	90	257.21	1.46	246.6	1.56	1	99
Him	24	Scherler, 2014	77.85	31.23	1089	143	7	5	1.34	0.09	3301	735	390	30	244.64	0.78	243.3	0.74	2	96
Him	25	Scherler, 2014	77.83	31.22	1180	52	11	3	1.39	0.07	2685	489	290	20	189.06	1.42	201.5	1.36	0	100
Him	26	Scherler, 2014	77.74	31.15	1268	25	14	2	1.48	0.12	2281	304	310	20	121.81	0.8	134.9	0.92	0	100
Him	27	Scherler, 2014	78.4	30.93	1330	171	4	4	1.38	0.1	3535	621	5370	460	261.41	1.75	290.3	1.75	0	100
Him	28	Morell, 2017	79	30.62	1843	102	11	2	1.55	0.14	2720	432	320	40	242.13	2.72	321.7	3.66	0	100
Him	29	Morell, 2015	79.51	30.53	1879	133	11	3	1.63	0.23	2756	485	640	100	320.17	5.65	429.3	7.49	0	100
Him	30	Morell, 2015	79.32	30.38	1551	228	16	2	1.23	0.14	1863	370	340	50	217.01	4.53	272.9	5.1	0	100
Him	43	Kim, 2017	83.88	28.38	797	313	2	8	0.82	0.44	4007	1146	787	7	438.73	3.59	345.1	3.28	0	100
Him	44	Puchol, 2014	84.29	28.38	797	313	2	8	0.82	0.44	4007	1146	585	5	438.73	3.59	345.1	3.28	49	51
Him	47	Puchol, 2014	84.3	28.37	808	166	6	3	0.56	0.08	3676	558	1700	400	340.32	7.45	289.9	6.22	50	50
Him	49	Kim, 2017	83.88	28.36	808	166	6	3	0.56	0.08	3676	558	2600	200	340.32	7.45	289.9	6.22	0	100
Him	50	Kim, 2017	83.96	28.34	808	166	6	3	0.56	0.08	3676	558	900	100	340.32	7.45	289.9	6.22	0	100
Him	51	Kim, 2017	83.89	28.34	808	166	6	3	0.56	0.08	3676	558	900	100	340.32	7.45	289.9	6.22	0	100
Him	52	Puchol, 2014	84.33	28.33	830	331	3	8	0.85	0.49	3909	1165	340	2	425.18	3.2	336.2	3.06	53	47
Him	56	Godard, 2012	84.41	28.32	858	187	7	4	0.6	0.13	3526	608	3300	600	338.45	6.39	292.3	5.22	1	99
Him	58	Godard, 2014	83.77	28.31	858	187	7	4	0.6	0.13	3526	608	2900	300	338.45	6.39	292.3	5.22	0	100
Him	65	Godard, 2012	84.36	28.28	1000	214	10	4	0.91	0.5	2979	774	2000	400	387.52	3.03	356	3.34	37	63
Him	68	Godard, 2014	83.74	28.28	1000	214	10	4	0.91	0.5	2979	774	800	100	387.52	3.03	356	3.34	0	100
Him	73	Andermann, 2011	85.37	28.23	543	216	-2	8	0.75	0.32	4677	1074	2500	300	406.09	1.28	282.2	0.95	0	100
Him	74	Andermann, 2011	85.3	28.18	834	294	6	8	0.86	0.48	3453	1205	2800	300	409.37	2.15	328.9	1.98	0	100
Him	76	Wobus, 2005	84.85	28.14	1483	239	13	2	1.49	0.82	2389	549	630	90	256.86	3.18	291.9	3.77	0	100
Him	78	Andermann, 2011	85.31	28.11	1013	468	6	9	1.11	0.73	3454	1335	585	3	370.32	3.22	314.7	2.2	0	100
Him	80	Andermann, 2011	84.83	28.1	1553	448	14	4	1.77	0.88	2205	846	410	2	204.79	5.8	230.5	5.01	0	100
Him	81	Wobus, 2005	84.83	28.1	1042	495	6	9	1.14	0.75	3394	1357	559	4	356.33	3.22	305.1	2.22	0	100
Him	83	Portenga, 2015	89.71	28.06	574	258	-1	8	0.77	0.35	4558	1162	2600	300	404.72	1.17	283.5	0.88	0	97
Him	90	Godard, 2014	85.18	27.98	1291	603	9	9	1.41	0.85	2885	1385	669	2	295.6	3.68	279.1	2.26	0	100
Him	92	Andermann, 2011	85.19	27.98	1935	194	17	1	2.38	0.62	1525	328	780	150	106.9	3.9	139.7	4.93	0	90
Him	93	Godard, 2014	85.19	27.98	808	252	7	4	0.78	0.21	3518	736	1360	170	430.89	8.72	351.1	8.17	0	90
Him	95	Wobus, 2005	84.73	27.95	1045	222	10	3	0.92	0.24	2973	538	2030	180	238.65	1.7	229.7	1.54	0	100
Him	96	Andermann, 2011	85.13	27.93	1105	531	9	9	1.24	0.61	2894	1539	1200	100	371.51	3.88	319.7	1.94	0	100
Him	97	Wobus, 2005	84.73	27.93	1261	107	15	2	1.4	0.25	2019	525	370	40	283.8	9.07	313	9.92	0	100
Him	98	Godard, 2014	85.14	27.92	2367	249	20	1	1.96	0.06	946	240	300	100	58.64	1.7	85.5	2.28	0	100
Him	101	Roux-Mallouf, 2015	89.74	27.89	1486	227	17	2	1.59	0.07	1429	423	730	50	173.14	2.35	200.2	2.52	0	100
Him	104	Wobus, 2005	84.74	27.88	298	37	-1	3	0.42	0.03	4572	472	335	28	177.57	1.93	100.2	1.08	0	100
Him	105	Godard, 2014	84.63	27.87	297	33	-1	3	0.43	0.04	4652	477	1174	99	182.6	2.57	103.2	1.48	0	100
Him	107	Portenga, 2015	89.87	27.86	299	39	-5	4	0.44	0.06	4978	509	1816	159	220.19	2.67	123.5	1.58	0	100
Him	110	Godard, 2014	84.97	27.81	868	620	3	11	0.99	0.54	3799	1690	2000	300	346.53	0.91	261.6	0.57	0	100
Him	111	Godard, 2014	84.89	27.81	1491	166	15	3	1.38	0.21	1908	647	1330	220	216.41	2.93	252.5	2.93	36	64
Him	113	Olen, 2015	87.37	27.77	1448	286	14	4	1.3	0.26	2140	855	880	50	231.3	2.67	259.6	2.26	0	100
Him	114	Godard, 2014	85.86	27.75	1452	283	14	4	1.3	0.25	2131	850	850	160	231.95	2.72	260.5	2.3	0	100
Him	115	Godard, 2014	85.07	27.75	307	46	-4	4	0.44	0.06	4933	544	1383	119	216.74	2.25	122.4	1.34	21	79
Him	116	Olen, 2015	87.35	27.74	2105	86	21	1	1.55	0.07	792	164	190	30	64.9	0.79	90.11	1.1	0	100
Him	117	Adams, 2016	91.15	27.72	1698	109	18	2	1.4	0.14	1242	359	460	30	121.58	2.18	152.3	2.61	0	100
Him	119	Adams, 2016	91.15	27.72	1703	115	18	2	1.4	0.14	1234	363	520	100	118.98	2.04	149.2	2.45	0	100
Him	121	Adams, 2016	91.17	27.69	942	684	4	11	1.02	0.55	3640	1783	1900	300	322.91	0.9	250.9	0.52	0	100
Him	126	Godard, 2014	85.73	27.68	2027	92	20	1	1.48	0.08	896	241	180	20	89.36	1.6	121.5	2.23	0	100
Him	127	Adams, 2016	89.77	27.67	2037	95	20	1	1.48	0.07	917	249	490	70	137.31	1.33	187.6	1.85	0	98
Him	128	Portenga, 2015	89.77	27.67	344	21	-2	1	0.45	0.01	4707	183	198	17	112.88	3.28	68.76	2.02	0	98
Him	129	Adams, 2016	91.44	27.66	357	25	-1	1	0.46	0.01	4613	215	1148	95	123.1	3.31	75.93	2.11	0	100
Him	130	Olen, 2015	87.36	27.66	349	31	-2	2	0.46	0.01	4707	266	693	58	168.46	2.46	102.6	1.49	0	100
Him	131	Roux-Mallouf, 2015	89.87	27.66	1983	72	18	3	1.52	0.25	1241	469	200	20	119.85	2.41	163.5	3.34	0	100
Him	133	Roux-Mallouf, 2015	89.8	27.63	1983	74	20	2	1.4	0.15	947	327	210	30	92.4	3.04	125.4	4.16	0	100
Him	135	Adams, 2016	91.49	27.62	1849	416	9	2	1.76	0.39	3067	422	470	40	280.14	3.53	345.7	3.15	0	100
Him	136	Andermann, 2011	86.09	27.62	2031	63	16	2	1.9	0.11	1710	405	710	120	170.2	1.01	233.1	1.41	0	100
Him	137	Adams, 2016	90.67	27.61	1941	119	17	2	1.54	0.32	1479	401	190	20	136.52	1.51	186.1	2.09	0	95
Him	140	Olen, 2015	87.28	27.59	620	167	7	4	0.81	0.35	3421	736	250	30	369.17	5.33	269.7	4.48	0	100
Him	142	Roux-Mallouf, 2015	89.85	27.59	777	611	-3	9	0.96	0.5	4748	1176	1480	110	416.46	3.28	272.3	2.73	0	100
Him	143	Adams, 2016	91.49	27.58	1049	131	14	2	1.35	0.22	2193	401	131	11	208.25	3.37	215.5	3.54	0	100
Him	144	Roux-Mallouf, 2015	89.63	27.58	704	185	8	4	0.91	0.41	3225	733	340	40	355.78	4.89	282.2	3.8	0	100
Him	146	Adams, 2016	90.44	27.56	481	189	2	5	0.6	0.28	4154	772	575	47	371.94	3.83	239.6	2.82	0	100

Him	147	Olen, 2015	87.31	27.56	443	188	-1	6	0.56	0.24	4442	873	1124	93	348.22	1.23	214.5	0.87	0	100
Him	148	Adams, 2016	91.52	27.55	1889	139	17	1	1.65	0.22	1513	317	120	10	168.67	1.97	227.5	2.58	0	99
Him	149	Roux-Mallouf, 2015	89.66	27.54	766	156	10	4	1.09	0.39	2903	650	1130	137	273.95	1.72	231.8	1.06	0	100
Him	151	Adams, 2016	90.44	27.54	917	153	10	3	0.87	0.2	3031	498	306	25	235.58	1.33	218.1	1.24	0	100
Him	152	Roux-Mallouf, 2015	89.8	27.53	2402	130	14	2	2.27	0.1	2183	468	2300	210	267.49	4.06	391.6	6.42	0	100
Him	153	Adams, 2016	89.87	27.53	920	149	14	2	1.44	0.32	2337	416	210	30	230.92	2.96	216.4	2.89	0	100
Him	154	Portenga, 2015	89.87	27.52	1610	165	19	1	1.2	0.23	1229	241	120	10	66.66	1.85	83.54	2.53	0	100
Him	156	Adams, 2016	91.17	27.52	854	670	1	9	0.96	0.53	4248	1344	2160	220	387.35	1.17	271.8	0.89	0	92
Him	158	Olen, 2015	87.19	27.51	1965	68	16	2	1.72	0.17	1776	381	270	10	163.96	1.98	223	2.66	0	100
Him	159	Adams, 2016	90.66	27.51	808	110	6	2	0.75	0.13	3572	376	80	10	154.77	1.6	134.9	1.27	0	100
Him	160	Portenga, 2015	89.79	27.51	419	220	-1	6	0.62	0.22	4551	842	1880	310	381.94	1.96	226.6	1.39	0	100
Him	162	Adams, 2016	90.66	27.5	2158	429	12	4	2.06	0.4	2559	680	####	760	303.05	3.51	401.9	4.36	0	100
Him	163	Roux-Mallouf, 2015	89.44	27.5	500	257	1	7	0.66	0.4	4224	1064	996	85	333.15	0.98	209.7	0.71	0	100
Him	164	Adams, 2016	90.67	27.5	1085	202	16	1	1.79	0.26	2008	325	90	9	173.1	1.49	171.6	1.36	0	100
Him	165	Adams, 2016	90.67	27.5	999	154	10	3	0.95	0.22	2919	503	179	15	208.2	0.69	199.7	0.67	0	100
Him	166	Adams, 2016	90.52	27.49	698	122	6	3	0.77	0.14	3549	455	170	20	225.91	1.62	182.8	1.2	0	100
Him	167	Olen, 2015	87.16	27.48	1150	752	2	9	1.23	0.63	4011	1250	940	70	399.39	4.2	313.4	4.79	0	100
Him	169	Adams, 2016	90.35	27.47	2106	362	13	4	2.03	0.33	2429	726	530	40	292.21	2.91	391.5	3.04	0	100
Him	170	Adams, 2016	89.9	27.46	1081	129	12	2	1.02	0.19	2702	411	166	13	237.18	4.22	240.3	4.64	0	94
Him	171	Portenga, 2015	89.9	27.46	876	68	8	1	0.93	0.13	3165	285	50	5	159.67	2.36	148.8	2.09	0	94
Him	172	Roux-Mallouf, 2015	89.44	27.45	1428	698	6	6	1.41	0.61	3467	1022	1360	100	425.78	3.27	418	4.57	0	100
Him	173	Adams, 2016	90.96	27.44	1133	39	11	2	1.21	0.19	2724	319	98	8	175.4	2.18	184.6	2.4	0	100
Him	174	Adams, 2016	89.68	27.43	962	60	12	3	1.36	0.29	2562	391	120	13	169.86	1.59	166.9	1.56	0	100
Him	175	Adams, 2016	89.68	27.43	1036	142	14	3	1.52	0.37	2380	462	134	13	197.03	1.27	196.6	1.34	0	100
Him	177	Adams, 2016	91.55	27.4	979	627	5	8	1.08	0.52	3648	1185	4310	790	397.18	1.82	311.7	1.72	0	100
Him	178	Olen, 2015	87.15	27.39	985	138	12	4	1.17	0.34	2663	633	252	21	264.24	1.15	257	1.32	0	100
Him	179	Adams, 2016	90.54	27.37	568	477	0	8	0.75	0.41	4426	1114	5240	1060	413.69	1.17	252.1	0.87	0	100
Him	181	Adams, 2016	91.67	27.36	918	73	7	2	0.83	0.1	3400	268	48	4	102.99	1.99	97.73	1.76	0	98
Him	182	Adams, 2016	91.62	27.34	1041	54	12	2	1.24	0.23	2754	332	146	11	166.25	4.61	170.2	4.72	0	92
Him	184	Adams, 2016	89.48	27.33	909	100	7	2	0.81	0.11	3475	288	79	7	105.82	0.94	98.03	0.76	0	100
Him	186	Adams, 2016	89.97	27.3	963	75	7	2	0.86	0.11	3441	302	117	14	110.92	1.59	107.1	1.47	0	100
Him	188	Adams, 2016	90.01	27.29	1037	85	9	2	1.03	0.2	3059	379	208	19	221.64	3.18	220.2	3.3	98	2
Him	189	Portenga, 2015	90.04	27.27	2310	162	17	2	2.01	0.42	1518	440	1000	60	256.79	8.33	377.3	12.3	1	90
Him	190	Adams, 2016	90.02	27.27	1870	564	14	3	1.83	0.42	2143	628	5270	1050	329.26	7.79	386.6	9.11	0	91
Him	191	Adams, 2016	90.05	27.26	1131	87	9	1	1.02	0.12	3060	226	102	10	139.86	2.4	145.6	2.6	83	17
Him	192	Portenga, 2015	90.05	27.26	1124	110	13	3	1.52	0.41	2460	527	132	12	215.71	1.24	225.1	1.28	83	17
Him	193	Roux-Mallouf, 2015	89.53	27.23	1124	109	13	3	1.52	0.41	2462	530	368	32	214.63	1.24	224	1.28	0	95
Him	194	Roux-Mallouf, 2015	89.48	27.23	925	79	10	2	0.99	0.15	3092	290	50	5	156.4	4.14	148.5	3.95	0	91
Him	195	Olen, 2015	87.24	27.21	843	38	5	1	0.71	0.03	3770	119	42	4	44.82	0.56	41.03	0.52	0	100
Him	197	Olen, 2015	87.26	27.18	1066	109	8	2	0.99	0.15	3198	314	65	6	166.5	2.02	167.7	2.05	0	100
Him	200	Olen, 2015	87.25	27.12	1856	201	21	1	1.15	0.32	871	276	220	10	131.34	2.09	177.1	3.2	0	100
Him	203	Roux-Mallouf, 2015	89.59	26.95	1272	173	12	3	1.18	0.28	2592	629	1541	156	294.96	3.09	317.9	3.43	0	100
Him	204	Roux-Mallouf, 2015	89.59	26.94	1294	176	13	3	1.24	0.31	2504	670	574	55	297.74	1.55	329.9	2.02	0	100
Him	206	Roux-Mallouf, 2015	89.6	26.88	1160	175	8	2	1.09	0.22	3118	388	45	4	194.76	1.65	200.5	2.11	0	100
Jap	1	Byun, 2015	128.71	37.74	1386	12	7	0	2.11	0.05	1083	86	72	13	31.15	1.09	36.15	1.28	100	0
Jap	2	Byun, 2015	128.72	37.72	1381	11	7	0	2.09	0.05	1033	90	102	23	38.73	0.65	44.87	0.75	100	0
Jap	8	Regalla, 2013	140.92	37.41	1316	15	11	0	1.67	0.06	486	105	130	4	76.28	1.71	86.56	1.93	100	0
Jap	10	Regalla, 2013	140.95	37.31	1327	20	11	0	1.68	0.07	451	126	186	6	64.87	0.82	73.92	0.93	85	7
Jap	12	Korup, 2014	137.76	35.72	2094	125	2	2	3.7	0.69	2114	337	1770	450	171.4	1.76	241.6	2.4	98	2
Ken	1	Acosta, 2015	36.84	1.91	459	8	21	0	0.29	0.01	1411	41	5	0	14.93	0.25	10.55	0.18	0	100
Ken	5	Roller, 2012	30.05	0.66	1522	32	16	2	1.12	0.13	2290	460	70	3	284.7	8.12	343.6	9.8	0	100
Ken	6	Roller, 2012	30.17	0.66	1473	9	16	1	1.07	0.07	2216	236	56	2	106.43	3.26	126.6	3.86	0	100
Ken	7	Roller, 2012	29.98	0.64	1532	76	15	4	1.21	0.27	2441	700	47	2	232.29	1.95	283.7	2.42	0	96
Ken	9	Roller, 2012	30.15	0.59	1496	39	15	2	1.13	0.12	2385	319	46	2	149.98	1.29	180.7	1.62	0	100
Ken	13	Roller, 2012	30.01	0.21	1667	187	11	4	1.48	0.47	2970	737	131	15	293.7	3.63	380.4	4.89	0	100
Ken	14	Roller, 2012	29.95	0.12	1653	181	12	5	1.47	0.53	2924	797	113	3	268.42	2.81	346.3	3.91	0	98
Ken	16	Roller, 2012	29.75	0.08	1420	98	16	3	1	0.19	2105	485	37	1	155.08	2.85	184.6	3.69	0	95
Saf	1	Chadwick, 2013	31.28	-23.04	564	56	23	0	0.32	0.04	413	52	7	1	12.09	0.04	9.59	0.03	1	98
Saf	2	Chadwick, 2013	31.24	-23.04	492	7	23	0	0.27	0.01	344	14	5	1	6.16	0.1	4.49	0.07	15	85
Saf	3	Chadwick, 2013	31.29	-23.12	548	39	23	0	0.31	0.03	404	44	5	1	10.97	0.06	8.55	0.04	11	89
Saf	4	Glotzbach, 2016	31.49	-23.93	536	6	22	0	0.32	0	365	17	7	1	8.19	0.09	6.2	0.06	21	79
Saf	5	Glotzbach, 2016	31.24	-23.94	542	5	22	0	0.32	0	404	11	3	0	7.02	0.11	5.34	0.08	0	100
Saf	6	Glotzbach, 2016	31.67	-24.73	635	8	22	0	0.41	0.01	377	17	4	0	7.73	0.09	6.31	0.08	100	0
Saf	7	Chadwick, 2013	31.5	-25.03	656	23	21	0	0.43	0.01	431	58	6	1	14.63	0.11	12.24	0.09	100	0
Saf	8	Glotzbach, 2016	31.26	-25.1	715	16	21	0	0.46	0.02	568	44	5	1	16.74	0.12	14.46	0.11	100	0
Saf	9	Glotzbach, 2016	31.22	-25.12	715	16	21	0	0.46	0.02	568	44	5	1	16.74	0.12	14.46	0.11	100	0
Saf	10	Glotzbach, 2016	31.71	-25.19	730	13	21	0	0.48	0.01	595	34	3	0	15.95	0.11	13.88	0.1	100	0
Saf	11	Chadwick, 2013	31.27	-25.22	629	4	22	0	0.43	0	332	17	4	0	8.76	0.12	7.11	0.11	100	0
Saf	12	Chadwick, 2013	31.27	-25.24	709	17	21	0	0.47	0.01	579	35	4	0	15.11	0.13	13.03	0.11	100	0
Saf	13	Glotzbach, 2016	31.43	-25.31	708	16	21	0	0.48	0.02	576	35	5	1	14.97	0.11	12.89	0.09	100	0
Saf	14	Glotzbach, 2016	31.39	-25.33	683	16	21	0	0.47	0.01	501	50	10	1	19.49	0.19	16.51	0.16	100	0
Mad	1	Cox, 2009	48.2	-17.63	1198	9	21	0	0.68	0	825	29	20	3	5.94	0.15	6.44	0.16	34	66
Nam	1	Bierman, 2007	17.26	-21.84	418	13	19	0	0.25	0.01	1616	68	6	1	13.99	0.11	9.53	0.07	0	100
Bra	2	Barreto, 2013	-43.45	-19.23	1563	37	19	1	1.08	0.03	1073	166	4	0	90.47	2.2	111.3	2.75	0	98
Bra	7	Salgado, 2007	-43.66	-20.37	1506	19	18	0	1.12	0.03	1213	81	4	2	35.43	0.95	42.75	1.15	29	68
Bra	16	Salgado, 2016	-44.63	-22.25	1890	98	14	1	1.51	0.11	1747	165	16	1	86.82	2.46	117.2	3.46	97	3
Bra	17	Rezende, 2013	-44.63	-22.25	1893	97	14	1	1.52	0.11	1750	163	15	0	87.86	2.82	118.7	3.97	97	3
Bra	18	Salgado, 2016	-44.64	-22.25	1979	124	14	1	1.6	0.13	1848	180	11	0	89.49	1.99	123.4	2.68	83	17
Bra	19	Salgado, 2016	-44.5	-22.25	1719	96	16	1	1.32	0.11	1462	195	15	1	81.35	2.12	105	2.71	29	71
Bra	20	Rezende, 2013	-44.5	-22.25	1717	94	16	1	1.31	0.11	1458	193	12	1	80.53	2.24	103.8	2.85	28	72
Bra	22	Salgado, 2016	-44.64	-22.27	2033	92	13	1	1.65	0.1	1916	135	12	0	64.53	1.34	89.62	1.85	95	5
Bra	23	Rezende, 2013	-44.64	-22.27	2035	92	13	1	1.66	0.1	1921	136	14	1	64.65	1.45	89.85	2.01	94	6

Bra	24	Salgado, 2016	-44.54	-22.28	1853	129	15	1	1.45	0.15	1642	232	19	1	123.05	1.69	165.1	2.24	0	100
Bra	25	Rezende, 2013	-44.54	-22.28	1845	128	15	1	1.44	0.15	1632	230	18	1	117.93	1.58	157.8	2.17	0	100
Bra	29	Salgado, 2016	-44.59	-22.32	1879	152	15	1	1.48	0.17	1686	252	20	1	112.82	2.74	152.2	3.75	41	59
Bra	30	Gonzalez, 2016	-43	-22.49	1784	64	15	2	1.5	0.17	1383	512	46	3	207.04	4.44	269.9	5.91	100	0
Bra	31	Salgado, 2016	-44.59	-22.67	1626	114	17	2	1.19	0.15	1121	315	22	1	120.63	4.11	152	5.45	25	75
Bra	32	Salgado, 2016	-44.53	-22.67	1626	100	17	1	1.2	0.13	1163	257	23	1	121.71	1.23	153.7	1.52	7	93
Bra	33	Salgado, 2016	-44.68	-22.69	1619	104	17	2	1.19	0.15	1131	319	27	2	112.22	3.52	140.6	4.57	1	99
Bra	39	Salgado, 2016	-44.55	-22.96	1683	101	19	2	1.08	0.08	710	370	49	9	140.2	3.13	174.9	3.84	15	85
Bra	43	Salgado, 2014	-48.75	-25.32	1916	50	18	2	1.53	0.07	745	445	20	1	123.84	2.83	166.2	3.77	92	6
SInd	23	Mandal, 2015	75.58	12.48	3316	270	21	0	2.24	0.24	1090	104	30	3	21.16	0.83	37.16	1.42	0	100
SInd	25	Mandal, 2015	75.71	12.45	3424	247	21	0	2.32	0.21	1073	78	30	3	24.08	1.07	42.77	1.83	0	100
SInd	27	Mandal, 2015	75.42	12.45	3224	926	22	1	2.15	0.87	955	106	24	2	10.31	0.11	18.45	0.2	100	0
SInd	35	Mandal, 2015	75.75	12.09	795	31	25	1	0.5	0.03	739	208	41	4	46.54	0.18	41.61	0.16	100	0
SInd	44	Mandal, 2015	75.75	11.77	3178	506	22	1	2.31	0.41	831	146	21	2	9.51	0.14	16.37	0.24	100	0
SInd	45	Mandal, 2015	75.81	11.7	3725	86	23	0	2.87	0.1	826	73	15	2	14.34	0.53	26.07	0.96	78	22
SInd	46	Mandal, 2015	75.8	11.69	4085	126	24	1	2.77	0.19	548	231	40	3	87.39	1.22	163.5	2.34	88	12
SInd	52	Mandal, 2015	76.01	11.41	1802	339	18	3	1.47	0.3	1530	581	22	2	94.95	2.28	123.2	2.6	46	54
SInd	62	Mandal, 2015	76.36	11.15	1515	147	15	1	1.59	0.13	2092	149	10	1	76.01	1.19	90.11	1.42	46	54
SInd	68	Mandal, 2015	76.57	10.92	980	659	25	3	0.61	0.48	678	356	23	2	39.85	0.05	38.98	0.05	4	96
SInd	79	Blanckenburg, 2004	80.66	7.15	2651	455	20	3	1.92	0.19	1221	448	17	2	84.53	0.56	126.1	0.75	0	94
SInd	80	Blanckenburg, 2004	80.75	7.13	2490	399	22	3	1.79	0.24	1014	460	45	5	67.05	0.42	100.6	0.59	0	96
SInd	84	Vanacker, 2007	80.78	6.72	2531	81	22	1	1.82	0.04	929	187	22	2	60.13	1.71	90.68	2.55	0	100
Taw	3	Derrieux, 2014	121.46	23.97	3147	790	13	4	3.27	1.26	1871	710	6500	1900	246.79	1.88	432.7	3.57	0	100
Taw	4	Derrieux, 2014	121.12	23.14	3124	815	13	4	3.18	1.27	1832	650	3300	1100	212.15	1.94	376.5	3.52	0	100

Table C2 p, C, C_{ne} and statistical goodness-of-fit metrics of R^2, χ^2, and Kolmogorov-Smirnov two-sided p-value at the 90% significance level for six climate bins of MAP, MAT, AI, and ME under different R^2 morphological steady-state thresholds from 0.75 to 0.95. Bolded values are low or negative R^2 or Kolmogorov-Smirnov p-value < 0.1 of poorly fit regressions.

	Morphological steady-state threshold $R^2 = 0.75$					Morphological steady-state threshold $R^2 = 0.8$				
MAP (mm/y	p	C	*R^2	†χ^2	KS p-value§	p	C	*R^2	†χ^2	KS p-value§
297-705	1.96	1.67E-08	0.5	4580	0.33	1.94	1.82E-08	0.49	4343	0.38
705-908	2.16	4.01E-09	0.26	6578	0.72	2.1	6.20E-09	0.23	6358	0.52
908-1123	1.80	2.45E-08	0.4	4986	0.33	1.93	1.17E-08	0.35	4585	0.19
1123-1386	1.80	4.38E-08	0.24	5522	0.44	1.77	5.64E-08	0.27	4721	0.82
1386-1717	3.30	1.56E-11	0.31	3750	0.33	3.71	2.01E-12	0.29	3503	0.52
1717-4085	3.18	5.88E-11	0.54	2680	**0.01**	3.16	6.42E-11	0.55	2383	**0.05**
MAT (°C)										
-5-3	3.21	1.67E-11	0.21	5861	**0.04**	3.7	1.03E-12	0.2	5361	**0.01**
3-7	2.48	1.12E-09	0.5	4320	0.23	2.32	2.69E-09	0.49	4012	0.27
7-10	2.16	4.42E-09	0.57	3344	0.43	2.37	1.69E-09	0.49	3809	0.53
10-13	2.13	6.08E-09	**-0.36**	9984	0.11	2.11	6.74E-09	**-0.47**	9310	0.12
13-16	3.69	1.50E-12	0.26	3513	**0.02**	3.83	8.20E-13	0.39	2766	**0.05**
16-25	1.66	6.73E-08	**0.09**	2602	**0.08**	1.62	7.10E-08	**-0.08**	3099	**0.08**
AI										
0.25-0.65	1.97	1.92E-08	0.72	2405	0.44	1.95	2.17E-08	0.71	2342	0.52
0.65-1	1.80	2.89E-08	0.19	8750	0.16	1.85	2.24E-08	0.18	7863	0.08
1-1.2	2.17	2.74E-09	0.43	4152	0.23	2.13	3.58E-09	0.42	3956	0.27
1.2-15.	2.50	7.32E-10	0.44	4110	0.44	2.65	3.01E-10	0.43	3624	0.52
1.5-1.9	3.14	4.08E-11	0.42	3173	0.33	2.96	1.07E-10	0.45	2946	0.38
1.9-3.8	1.86	4.45E-08	**-0.3**	9014	0.75	1.95	2.91E-08	**-0.22**	7471	0.82
ME (m)										
332-826	1.47	1.19E-07	**-0.06**	2575	0.95	1.45	1.21E-07	**-0.12**	2809	0.99
826-1239	2.67	1.27E-09	**0.03**	2885	**0.04**	2.28	6.43E-09	**0.01**	2462	0.11
1239-1771	3.53	9.36E-12	0.31	2343	**0.01**	3.86	1.94E-12	0.38	1962	**0.02**
1771-2361	4.06	2.83E-13	0.38	3077	0.72	4.15	1.73E-13	0.30	3203	0.82
2361-3197	4.21	3.57E-14	0.38	3535	0.44	4.35	1.62E-14	0.34	3411	0.52
3197-4977	4.10	7.37E-14	0.24	5921	**0.01**	3.69	8.21E-13	0.17	5641	**0.02**

*R^2 statistical goodness of fit

†χ^2 statistical goodness of fit

§Two sample Kolmogorov-Smirnov two sided p-value test at 90% significance level. H_0 = Calculated and modeled k_{sn} are from same continuous distribution.

	Morphological steady-state threshold $R^2 = 0.85$					Morphological steady-state threshold $R^2 = 0.9$				
MAP (mm/y	p	C	*R^2	†χ^2	KS p-value§	p	C	*R^2	†χ^2	KS p-value§
297-705	1.87	2.68E-08	0.53	3191	0.38	1.78	4.28E-08	0.50	2797	0.56
705-908	2.08	7.45E-09	0.28	4891	0.7	1.99	1.24E-08	0.48	2981	0.75
908-1123	1.76	2.73E-08	**0.01**	5407	0.16	2.01	7.98E-09	0.38	2860	0.26
1123-1386	1.98	1.53E-08	0.15	4437	0.55	2.20	5.54E-09	0.28	2806	0.91
1386-1717	3.24	2.36E-11	0.33	3123	0.26	3.02	6.64E-11	0.32	2502	0.16
1717-4085	3.08	8.44E-11	0.48	2473	**0.03**	3.27	3.06E-11	0.51	1982	**0.08**
MAT (°C)										
-5-3	4.3	3.60E-14	0.14	4516	**0.01**	2.97	6.37E-11	0.18	3734	**0.05**
3-7	2.23	4.34E-09	0.51	3260	0.38	2.30	3.24E-09	0.53	2514	0.75
7-10	2.45	1.02E-09	0.61	2326	0.38	2.40	1.05E-09	0.70	1350	0.91
10-13	2.08	7.65E-09	**-0.61**	8323	0.26	2.40	1.70E-09	**-0.24**	4762	0.26
13-16	4.98	2.07E-15	0.41	2131	0.11	4.14	1.52E-13	0.43	1783	0.56
16-25	1.76	4.91E-08	0.3	2117	0.14	1.75	5.20E-08	0.52	1256	0.32
AI										
0.25-0.65	1.92	2.62E-08	0.71	1990	0.7	1.84	3.90E-08	0.77	1246	0.91
0.65-1	1.97	1.22E-08	0.35	4794	0.38	2.01	1.01E-08	0.40	3561	0.75
1-1.2	2.12	3.74E-09	0.33	3524	0.26	2.24	2.17E-09	0.49	2233	0.26
1.2-15.	2.72	2.32E-10	0.4	3128	0.7	2.90	7.94E-11	0.41	2455	0.91
1.5-1.9	3.28	1.38E-11	0.51	2103	0.38	3.60	2.43E-12	0.54	1491	0.56
1.9-3.8	1.69	1.21E-07	**-0.35**	7788	0.76	1.73	1.09E-07	**-0.13**	5313	0.81
ME (m)										
332-826	1.26	2.52E-07	**-0.3**	2387	0.53	1.35	1.71E-07	**-0.28**	1781	0.56
826-1239	3.38	6.85E-11	0.06	1862	**0.04**	2.60	1.70E-09	0.19	1310	0.16
1239-1771	3.78	2.41E-12	0.37	1898	**0.04**	3.95	1.04E-12	0.35	1321	**0.09**
1771-2361	6.09	5.33E-18	0.2	2506	0.53	5.29	4.28E-16	0.30	2028	0.91
2361-3197	4.5	6.51E-15	0.44	2228	0.7	4.65	3.22E-15	0.45	1766	0.91
3197-4977	3.41	4.02E-12	0.19	4921	**0.03**	3.26	9.00E-12	0.27	3850	**0.04**

*R^2 statistical goodness of fit

†χ^2 statistical goodness of fit

§Two sample Kolmogorov-Smirnov two sided p-value test at 90% significance level. H_0 = Calculated and modeled k_{sn} are from same continuous distribution.

	Morphological steady-state threshold $R^2 = 0.9$ (fixed p)					Morphological steady-state threshold $R^2 = 0.95$				
MAP (mm/y	p	C_{ne}	*R^2	†χ^2	KS p-value§	p	C	*R^2	†χ^2	KS p-value§
297-705	2.18	7.28E-09	0.68	1807	0.16	1.64	9.66E-08	0.55	1233	0.88
705-908	2.18	4.75E-09	0.54	2646	0.26	2.01	1.12E-08	0.52	1704	0.88
908-1123	2.18	3.37E-09	0.55	2093	0.26	2.82	9.46E-11	0.54	1107	0.24
1123-1386	2.18	6.09E-09	0.26	2865	0.91	1.8	2.89E-08	0.66	928	0.99
1386-1717	2.18	3.38E-09	**0.09**	3377	0.16	5.48	1.79E-16	0.39	857	0.41
1717-4085	2.18	4.65E-09	**-1.20**	8855	**0.01**	2.94	1.81E-10	0.56	1128	0.3
MAT (°C)										
-5-3	2.18	4.81E-09	**0.02**	4480	0.39	2.6	4.50E-10	0.29	2158	0.41
3-7	2.18	5.67E-09	0.48	2753	0.75	2.49	6.40E-10	0.64	1031	0.88
7-10	2.18	3.04E-09	0.68	1448	0.91	3.21	2.41E-11	0.58	1020	0.88
10-13	2.18	4.79E-09	**-0.76**	6764	0.26	3.22	2.51E-11	0.28	1545	0.12
13-16	2.18	2.30E-09	**-2.59**	11139	0.16	6.74	2.22E-19	0.35	916	0.41
16-25	2.18	1.10E-08	0.62	1006	0.13	1.61	9.13E-08	0.4	724	0.49
AI										
0.25-0.65	2.18	9.69E-09	0.77	1209	0.16	1.81	5.61E-08	0.7	727	0.65
0.65-1	2.18	4.18E-09	0.49	3017	0.75	1.89	1.90E-08	0.33	2206	0.88
1-1.2	2.18	2.80E-09	0.43	2470	0.26	2.88	7.48E-11	0.81	560	0.88
1.2-15.	2.18	2.79E-09	**-0.14**	4743	0.75	3.15	1.91E-11	0.51	1134	0.88
1.5-1.9	2.18	2.34E-09	**-0.44**	4716	0.39	4.84	7.12E-15	0.29	1128	0.41
1.9-3.8	2.18	1.33E-08	0.37	2951	0.21	2.48	1.64E-09	0.16	2239	0.92
ME (m)										
332-826	2.18	9.70E-09	0.26	1031	**0.09**	1.34	1.62E-07	**-0.26**	1088	0.65
826-1239	2.18	8.89E-09	0.12	1411	0.16	2.2	7.54E-09	0.25	717	0.24
1239-1771	2.18	3.86E-09	**-1.24**	4576	**0.05**	5.85	6.57E-17	0.44	681	0.88
1771-2361	2.18	4.56E-09	**-2.20**	9284	**0.05**	4.12	2.04E-13	0.29	1267	0.65
2361-3197	2.18	2.03E-09	**-3.76**	15250	**0.09**	5.22	1.65E-16	0.46	939	0.65
3197-4977	2.18	3.72E-09	**-0.33**	7035	0.21	2.94	4.96E-11	0.39	2044	0.3

*R^2 statistical goodness of fit

†χ^2 statistical goodness of fit

§Two sample Kolmogorov-Smirnov two sided p-value test at 90% significance level. H_0 = Calculated and modeled k_{sn} are from same continuous distribution.